

Dissertation

zum Thema

Electron Energy-Loss Spectroscopy on Underdoped Cuprates and Transition-Metal Dichalcogenides

der Fakultät Mathematik und Naturwissenschaften
der Technischen Universität Dresden
vorgelegt von

Dipl. Phys. Roman Schuster

geboren am 17.01.1981 in Schlema

und

zur Erlangung des akademischen Grades

Doctor rerum naturalium

(Dr. rer. nat.)

begutachtet durch

Prof. Dr. rer. nat. habil. Bernd Büchner
Prof. Dr. rer. nat. habil. Markus Grüninger

Contents

1. Motivation	7
2. Electron Energy-Loss Spectroscopy	11
2.1. Introduction	11
2.2. Working Principle	12
2.3. Theoretical Remarks	12
2.3.1. Kinematics	13
2.3.2. Scattering Theory	14
2.4. The Dielectric Function	17
2.4.1. The Electron Gas In RPA	18
2.4.2. Effects Beyond RPA	24
2.4.3. The DRUDE-LORENTZ-Model	27
2.5. Experimental Details	29
2.5.1. The Spectrometer	29
2.5.2. Sample Preparation	30
3. EELS On Underdoped Cuprates	33
3.1. Introduction	33
3.2. Electronic Properties Of The Cuprates	34
3.3. Charge-Transfer Excitons In Underdoped Oxychlorides	43
3.3.1. Origin Of The Observed Features	44
3.3.2. Dispersion Of The CT-Exciton	49
3.4. Evolution Of The Charge Carrier Plasmon	53
4. EELS On Transition-Metal Dichalcogenides	67
4.1. Introduction	67
4.2. Basic Properties	68
4.3. Plasmon Dispersion	74
4.4. Possible Relation To Pnictides	86
A. Properties Of The EELS Electrons	91

List of Figures

2.1. The EELS scattering geometry	12
2.2. Momentum transfer in the a - b -plane of the sample	14
2.3. The LINDHARD function	21
2.4. The static LINDHARD function for different dimensions	23
2.5. Schematic view of the PEIERLS transition in 1D	24
2.5.1. The linear chain (undistorted)	24
2.5.2. The linear chain (distorted)	24
2.6. Plasmon and single-particle excitations in the RPA	25
2.7. The dielectric function in the DRUDE-LORENTZ-model	29
2.7.1. The dielectric function of a metal	29
2.7.2. The dielectric function of an insulator	29
2.8. Schematic view of the EELS spectrometer	30
2.9. The characteristics of the electron beam	31
2.9.1. Energy Resolution	31
2.9.2. Momentum Resolution	31
2.10. EELS sample On TEM grid	31
3.1. The crystal structure of $\text{Ca}_{2-x}\text{Na}_x\text{CuO}_2\text{Cl}_2$ and $\text{La}_{2-x}\text{Sr}_x\text{CuO}_4$	34
3.2. The metal-insulator transition in the single-band HUBBARD model	36
3.3. MOTT vs. charge-transfer insulator	37
3.4. The CuO_2 plane of the undoped cuprates	38
3.5. The motion of a single hole in an antiferromagnet	40
3.6. The generic phase diagram of the cuprates	41
3.7. The FERMI surface of cuprates	42
3.8. $\text{Ca}_{1.9}\text{Na}_{0.1}\text{CuO}_2\text{Cl}_2$: BRAGG spectra	44
3.9. Comparison of the EELS intensity in $\text{Sr}_2\text{CuO}_2\text{Cl}_2$ and $\text{Ca}_{2-x}\text{Na}_x\text{CuO}_2\text{Cl}_2$	45
3.10. Charge-transfer exciton within the CuO_2 plane	45
3.11. The one-dimensional chain compound Sr_2CuO_3	47
3.12. Optical conductivity for Sr_2CuO_3 and $\text{Sr}_2\text{CuO}_2\text{Cl}_2$	47
3.13. $\text{Ca}_{2-x}\text{Na}_x\text{CuO}_2\text{Cl}_2$: resistivity and optical conductivity	50
3.14. $\text{Sr}_2\text{CuO}_2\text{Cl}_2$: exciton dispersion	50
3.15. $\text{Ca}_{2-x}\text{Na}_x\text{CuO}_2\text{Cl}_2$: x - and q -dependence of the loss function	51
3.15.1 $x = 0.05$, $q \parallel (100)$	51
3.15.2 $x = 0.05$, $q \parallel (110)$	51
3.15.3 $x = 0.10$, $q \parallel (100)$	51
3.15.4 $x = 0.10$, $q \parallel (110)$	51

3.16. $\text{Ca}_{1.95}\text{Na}_{0.05}\text{CuO}_2\text{Cl}_2$: the dispersion of the charge-transfer exciton	52
3.16.1 $q_{\parallel}(100)$	52
3.16.2 $q_{\parallel}(110)$	52
3.17. $\text{Ca}_{1.9}\text{Na}_{0.1}\text{CuO}_2\text{Cl}_2$: plasmon dispersion	54
3.18. $\text{Bi}_2\text{Sr}_2\text{CaCu}_2\text{O}_{8+\delta}$: plasmon dispersion	55
3.19. $\text{Ca}_{1.9}\text{Na}_{0.1}\text{CuO}_2\text{Cl}_2$: angular dependence of the loss function I	56
3.19.1.300 K	56
3.19.2.30 K	56
3.20. $\text{Ca}_{1.9}\text{Na}_{0.1}\text{CuO}_2\text{Cl}_2$: plasmon intensity vs. angle.	57
3.21. $\text{Ca}_{1.9}\text{Na}_{0.1}\text{CuO}_2\text{Cl}_2$: angular dependence of the EELS intensity II	57
3.22. $\text{Ca}_{1.9}\text{Na}_{0.1}\text{CuO}_2\text{Cl}_2$: spectral weight variations within the CuO_2 plane	58
3.23. Effects of glassy order in the CuO_2 plane	61
4.1. What are transition-metal dichalcogenides?	68
4.2. Polymorphs of the transition-metal dichalcogenides	69
4.3. The crystal structure of the $2H$ modifications	70
4.4. Resistivity vs. temperature for several transition-metal dichalcogenides.	71
4.5. $2H\text{-TaSe}_2$: FERMI surface	72
4.6. $2H\text{-TaSe}_2$: EELS intensity	74
4.7. $2H\text{-TaSe}_2$: EELS intensity in the energy range of the charge carrier plasmon	75
4.8. $2H\text{-TaSe}_2$: temperature dependence of the superstructure	76
4.9. $2H\text{-TaSe}_2$: plasmon dispersion	76
4.10. $2H\text{-TaSe}_2$: plasma frequency vs. temperature	77
4.11. $2H\text{-TaS}_2$ and $2H\text{-NbSe}_2$: plasmon dispersion	78
4.12. $2H$ -modification: spectral weights	78
4.13. $2H$ -modifications: normalized plasmon dispersion	79
4.14. $2H\text{-TaSe}_2$: EELS intensity after potassium intercalation	79
4.15. $2H\text{-TaSe}_2$ and $2H\text{-TaS}_2$: dispersion after potassium intercalation	80
4.16. $2H$ -modification: plasmon dispersion after potassium intercalation	81
4.17. $2H\text{-TaSe}_2$ and $2H\text{-NbSe}_2$: density of states	84
4.18. $2H\text{-TaSe}_2$ and $2H\text{-NbSe}_2$: reflectivity	88

1. Motivation

WHEN atoms come together to form a single crystal the result is quite a remarkable object. People visiting mineralogical exhibitions enjoy its beauty which is a mere consequence of the regular arrangement of the atoms inside of it. Nonetheless, most of the visitors might find it astonishing to learn that it is the absence of regularity—their *low* symmetry—which makes them interesting from a more scientific point of view. Although it may sound surprising at first, it is precisely this lack of symmetry which results in an aching toe when trying to kick a stone on the beach—a fact that everybody believes immediately. This particular manifestation of a so called “broken symmetry”—in the case of the crystal this is the broken translational invariance—is one of the rare examples of this phenomenon which are known already since ages. The other one is probably magnetism which was already familiar to the ancient Greeks and Chinese. It was however only the advent of modern experimental and theoretical methods that allowed scientists to figure out that a piece of a solid may intrinsically host a myriad of other and even more exotic symmetry-broken phases. P. W. ANDERSON nicely paraphrased this in 1972 by remarking that “More is different!” [1]. Nowadays it is certainly not overstated to say that each particular degree of freedom an electron has in a simple atom will eventually find itself forming its own specific ordered phase inside a solid. The spin may order to form different magnetic ground states, the occupation of particular wavefunctions may condense into orbital order, ferroelectricity can arise as a consequence of ordered dipole moments, superconductivity may be induced by the pairing of electrons into pairs and even the charges of the electrons can be ordered under certain circumstances.

Even more importantly it was found in recent years that different ordering phenomena quite often reside in close proximity to each other and that only small changes in an external parameter like the temperature, pressure or magnetic field may suffice to swap a system from one phase to a possibly totally different one. All this can be traced back to the often strong coupling between the constituents of the solid, with the electron-electron interaction being of special relevance. It is therefore not surprising that compounds containing elements with $3d$ - or $4f$ -electrons are ubiquitous in this particular field of solid-state physics often referred to as “strongly-correlated electron physics”. Typical examples are superconductivity in cuprate-, heavy-fermion- or re-

1. Motivation

cently even iron-based superconductors or magnetic-, charge- and orbital-order in systems containing manganese.

All the above mentioned types of order have consequences that are observable in the laboratory and allow to probe the different phases in great detail. There appear more or less sharp phase transitions that are traditionally probed by second derivatives of the free energy like the magnetization or the specific heat. Moreover and also more interesting in the context of the present work is the fact that a broken symmetry always results in particular excitations that are observable in a spectroscopic experiment. Typical examples for this are acoustic phonons for the case of the broken translational invariance, magnons if the rotational symmetry in spin-space is broken or phasons when the charges become periodically modulated. These acoustic branches of the quasiparticle spectrum follow from the GOLDSTONE theorem which basically states that every broken global symmetry results in the appearance of a massless bosonic mode. These excitations can in principle be probed by spectroscopic methods—magnons and phonons are routinely investigated by neutron scattering for example. Nevertheless, inelastic electron scattering which forms the experimental method employed throughout this work does not provide access to those kinds of modes. While it is not sensitive to magnetic degrees of freedom rendering magnons invisible, it can potentially detect phonons or low lying charge excitations but still they are normally not detected due to an insufficient resolution in energy.

If, however, the gauge symmetry of the electromagnetic field becomes broken as in the case of a plasma [2, 3] another optical—or massive, in the language of particle physics—mode appears that is called plasmon in the solid-state literature. This is the analog of the up to now still speculative HIGGS mechanism in particle physics and one may therefore extend ANDERSON's above given statement to "More is ahead!".

Disentangling the properties of plasmons is one of the traditional tasks for inelastic electron scattering and the present thesis will basically do exactly this for two compound classes that can be considered as paradigms for all the things mentioned above.

The outline of this work is as follows: In Ch. 2 the experimental method and some vocabulary required for the later discussion are introduced. Ch. 3 starts with some general remarks on cuprates—the nowadays already traditional high-temperature superconductors. The focus is on the electronic properties, in particular in the underdoped region of the phase diagram where antiferromagnetism, spin-/charge-order and superconductivity can be found. The first experimental part deals with the doping dependence of the charge-transfer excitations between copper and oxygen and their momentum dependence, exemplified on the model system $\text{Ca}_{2-x}\text{Na}_x\text{CuO}_2\text{Cl}_2$. In addition for doping concentrations above the metal-insulator transition the behavior of the charge-carrier plasmon is investigated which turns out to be highly anomalous. In Ch. 4 the focus will

be on systems which were known to show charge- and superconducting order already well before the discovery of the cuprates, namely the transition-metal dichalcogenides. Again, the main point of interest will be the behavior of the charge-carrier plasmon that exhibits a behavior that differs substantially from the generic expectation for ordinary metals. Finally, we discuss a possible relation between the dichalcogenides and the recently discovered iron-based superconductors based on possible similarities in their optical properties.

A final remark on units. Whenever formulas appear in the text it may happen that natural constants and proportionality factors are treated with little care. This is done for convenience but also in order to emphasize the main physical statements. Only in the rare cases when explicit numbers are needed every parameter is (hopefully) plugged in properly.



2. Electron Energy-Loss Spectroscopy

2.1. Introduction

OUR understanding of the microscopic mechanisms governing the world around us crucially depends on the fact of being able to perform accurate measurements for systems of different complexity, ranging from atoms or molecules to condensed matter like liquids and solids. To this end scattering of different probe particles has played an indispensable role ever since the beginning of the 20th century when RUTHERFORD first employed α -particles to study the nature of the atom [4]. The decades since then have seen an enormous development of experimental and theoretical facilities and, as a consequence, there is a wealth of information available on the electronic structure of matter. Nowadays scattering experiments are routinely employed to study quantum objects over many orders of magnitude in energy, ranging from lattice and spin dynamics in solids on the meV to hadron physics on the GeV or even TeV scale.

For a solid electrons form an important ingredient and they carry a charge as a particularly important degree of freedom. With the things mentioned above it cannot be considered as a surprise that there are also well established scattering methods for this channel available: (resonant) inelastic x-ray and electron scattering. The latter one, also termed electron energy-loss spectroscopy (EELS) has been and probably still is the *de facto* standard method to measure the dynamics of collective charge modes in a solid since the pioneering efforts of RUTHEMANN and LANG in the 1940s [5–8]. In addition, state of the art transmission electron microscopes are equipped with suitable detectors to measure chemical compositions of materials by investigating core edges with very high spatial resolution [9].

The spectrometer employed for the present work was, however, built with different purposes in mind and is optimized not for high spatial but momentum resolutions. With this at hand it becomes possible to measure k -space dynamics of different types of excitations in a wide range of samples from simple metals to complex oxides and even molecular solids.

2. Electron Energy-Loss Spectroscopy

In the following we will first of all describe the general principle of an EELS experiment in transmission*, supplemented by some theoretical remarks, basically about scattering in general and the role and properties of the dielectric function for the interpretation of the EELS data. Finally some facts about experimental subtleties like sample preparation and the spectrometer performance will be listed.

2.2. Working Principle

The basic principle of an EELS experiment is shown in Fig. 2.1. A beam of rather fast (see Appendix A) electrons is focused on a thin (≈ 100 nm) film of the sample under investigation. While passing through the sample a fraction of the beam electrons is scattered an angle θ away from the initial direction defined by k_0 . This leads to a momentum- (q) and energy-transfer (ω) and will as a consequence leave the sample in an excited state, which is characterized by the energy and momentum it acquired from the electrons in the beam.

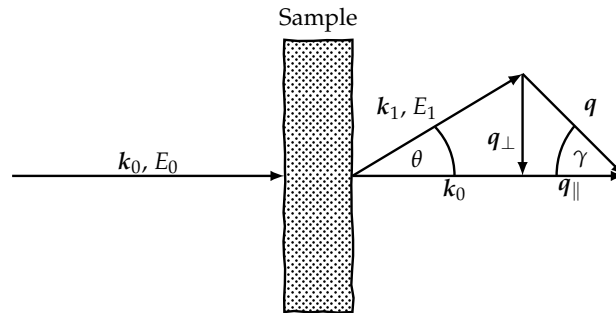


FIGURE 2.1.: The basic scheme for an EELS experiment in transmission. The electrons with incoming momentum k_0 and energy E_0 are focused on the sample and scattered under an angle θ . The momentum transfer q which takes place during the scattering process results in an energy transfer ω in the sample.

2.3. Theoretical Remarks

The aim of this section is to establish the connection between the microscopic excitations caused by the electron energy-loss spectroscopy process to the intensity which is measured at the detector of the EELS spectrometer. This is of great importance in order to understand what is actually observed in the experimental spectra and it allows in principle to calculate the EELS response with the help of microscopic theories.

*It is also possible to perform EELS in reflection to study, e. g., surface dynamics, but we will not elaborate on this in the remainder of this work.

2.3.1. Kinematics

The scattering preserves energy and momentum conservation

$$\begin{aligned} \mathbf{k}_0 &= \mathbf{k}_1 + \mathbf{q} \\ \omega &= E_0 - E_1. \end{aligned}$$

According to Fig. 2.1 the momentum transfer \mathbf{q} can be decomposed into components parallel and perpendicular to the incoming momentum \mathbf{k}_0

$$q^2 = q_{\parallel}^2 + q_{\perp}^2.$$

The energy loss ω that causes the excitations within the solid can be related to the momentum transfer \mathbf{q} via

$$\omega = \frac{q^2}{2m} \cong \frac{(k_0^2 - k_1^2)}{2m}.$$

Now it is important to realize that the primary energy of the electrons is rather high ($E_0 = 172$ keV in the present case) which in turn leads to a large value of $k_0 \sim 230 \text{ \AA}^{-1}$ (see Eq. A.2). Comparing this to typical extensions of a BRILLOUIN zone inside a solid which are of the order 1 \AA^{-1} one arrives at small scattering angles θ and therefore

$$q_{\perp} = k_1 \sin \theta \cong k_1 \theta \cong k_0 \theta.$$

In addition, one obtains from the cosine theorem (see Fig. 2.1)

$$k_1^2 = k_0^2 + q^2 - 2k_0q \cos \gamma \cong k_0^2 - 2k_0q \cos \gamma.$$

Therefore the excitation energy reads

$$\omega \cong \frac{(k_0^2 - k_1^2)}{2m} \cong \frac{k_0}{m} \cdot q \cos \gamma = \frac{k_0}{m} \cdot q_{\parallel}.$$

For a typical energy-loss of $\omega \sim 10$ eV and experimentally observed scattering angles of $\theta \sim 0.25^\circ$ we obtain the important result

$$\frac{q_{\parallel}}{q_{\perp}} = \frac{m\omega}{k_0^2 \theta} \sim 10^{-3}$$

and so the momentum transfer can be considered to be confined entirely to the sample plane perpendicular to the incoming electron beam. To obtain information beyond this particular plane one has to rotate the sample with respect to the beam for this will create a projection parallel to \mathbf{k}_0 proportional to $\sin \zeta$, with ζ being the angle between the sample normal and \mathbf{k}_0 .

2. Electron Energy-Loss Spectroscopy

In addition to the possibility of inelastic scattering processes which lead to a finite energy loss it is also possible to perform BRAGG scattering by setting the energy-loss to zero. This allows the analysis of the lattice structure and is an important tool in particular for investigations on single-crystals where the electronic properties may depend on the direction in the reciprocal lattice. With the above derived two-dimensionality of the momentum transfer it is clear that one may write

$$\mathbf{q}_\perp \equiv \mathbf{q} = \mathbf{q}_0 e^{i\phi}$$

and as can be seen from Fig. 2.2 by varying either ϕ or q_0 it is possible to adjust \mathbf{q} within the reciprocal lattice in order to find directions fulfilling the BRAGG condition which may then be taken to measure, e. g., the dispersion of a particular excitation along a well defined axis.

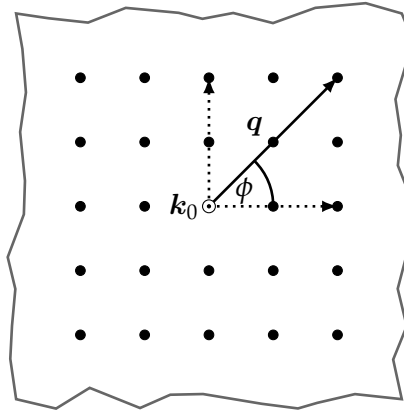


FIGURE 2.2.: A sketch of the momentum transfer in the a - b -plane (note the direction of \mathbf{k}_0 compared to Fig. 2.1) for the special case of a square lattice. Whenever the momentum transfer \mathbf{q} connects two points of the reciprocal lattice the BRAGG condition is fulfilled and there appears a peak in the elastic scattering

2.3.2. Scattering Theory

The essential quantity which is of interest for all inelastic scattering experiments is the doubly differential cross section [10–14]

$$\frac{d^2\sigma}{d\Omega d\omega}$$

It describes the probability of detecting a particle in a solid angle element $d\Omega$ having lost an energy $d\omega$ compared to its initial energy E_0 and this is exactly the intensity

2.3. Theoretical Remarks

which is measured in an EELS experiment shown in Fig. 2.1. The cross section can be shown to be given by

$$\frac{d^2\sigma}{d\Omega d\omega} = \sum_{n_0, n_1} |\langle n_1, k_1 | H_{int} | n_0, k_0 \rangle|^2 \delta(E_{n_0} + E_0 - E_{n_1} - E_1), \quad (2.1)$$

with the initial (final) states of the incoming (outgoing) electrons

$$|k_l\rangle \propto e^{ik_l r} \quad l = 0, 1$$

and the corresponding ones for the sample $|n_l\rangle$. In writing Eq. 2.1 use is made of the BORN approximation which assumes only weak interaction of the electrons with the sample. This is equivalent to demand that the initial and final states can be written as simple products

$$|n_l, k_l\rangle = |n_l\rangle |k_l\rangle .$$

The interaction between the sample and the scattered electrons is driven by the COULOMB potential which reads

$$H_{int} = \frac{e^2}{q^2} .$$

With this, one is lead to the result

$$\frac{d^2\sigma}{d\Omega d\omega} = A(\mathbf{q}, \omega) \cdot S(\mathbf{q}, \omega)$$

with

$$A(\mathbf{q}, \omega) = \frac{1}{q^4}$$

and

$$S(\mathbf{q}, \omega) = \frac{1}{N} \sum_{n_0, n_1} p_{n_0} \left| \langle n_1 | \sum_j e^{iqr_j} | n_0 \rangle \right|^2 \delta(E_{n_0} - E_{n_1} + \omega) .$$

The term $A(\mathbf{q}, \omega)$ and $S(\mathbf{q}, \omega)$ are the RUTHERFORD cross-section and the dynamic structure factor, respectively. While the former arises due to the particular nature of the COULOMB potential and is specific for the case of electron scattering[†] the latter describes the response of the sample, i. e., the spectrum of possible excitations and is therefore the quantity of interest in a scattering experiment.

[†]In particular the appearance of the $1/q^4$ term leads to a limited applicability of electron energy-loss spectroscopy in momentum space. In contrast to that inelastic x-ray scattering does not suffer from this drawback which allows measurements up to rather high values of momentum transfer, without such a dramatic loss of countrate. This flexibility has already been employed to invert the response function from the (\mathbf{q}, ω) - to the (\mathbf{r}, t) -domain thereby allowing the extraction of real-space dynamics of density fluctuations in real solids see, e. g., Refs. 15, 16.

2. Electron Energy-Loss Spectroscopy

It was VAN HOVE who first realized the close relationship between the structure factor and the density-density correlation function [17] which can be established with the definition of the density operator

$$\rho(\mathbf{r}) = \sum_j \delta(\mathbf{r} - \mathbf{r}_j) = \frac{1}{V} \sum_q \rho_q e^{i\mathbf{q}\mathbf{r}} \iff \rho_q = \sum_j e^{-i\mathbf{q}\mathbf{r}_j}, \quad (2.2)$$

its HEISENBERG representation

$$\rho(\mathbf{q}, t) = e^{iH_0 t} \rho(\mathbf{q}) e^{-iH_0 t},$$

the definition of the δ -function

$$\delta(E_{n_0} - E_{n_1} + \omega) = \frac{1}{2\pi} \int dt e^{i(E_{n_0} - E_{n_1} + \omega)t},$$

and the completeness relation for the states $\sum_i |i\rangle \langle i| = \mathbb{1}$.

It reads

$$\begin{aligned} S(\mathbf{q}, \omega) &= \frac{1}{N} \sum_{n_0, n_1} p_{n_0} \left| \langle n_1 | \sum_j e^{i\mathbf{q}\mathbf{r}_j} | n_0 \rangle \right|^2 \delta(E_{n_0} - E_{n_1} + \omega) \\ &= \frac{1}{2\pi N} \int dt e^{i\omega t} \sum_{n_0} p_{n_0} \langle n_0 | \rho_{\mathbf{q}}(t) \rho_{-\mathbf{q}}(0) | n_0 \rangle \\ &= \frac{1}{2\pi N} \int dt e^{i\omega t} \langle \rho_{\mathbf{q}}(t) \rho_{-\mathbf{q}}(0) \rangle_T \\ &= \frac{1}{2\pi N} \int dt e^{i\omega t} \int d^3\mathbf{r} d^3\mathbf{r}' e^{-i\mathbf{q}(\mathbf{r}-\mathbf{r}')} \langle \rho(\mathbf{r}, t) \rho(\mathbf{r}', 0) \rangle_T, \end{aligned}$$

where we introduced the notation $\langle O \rangle_T = \sum_i p_i O_{ii} = \sum_i p_i \langle i | O | i \rangle$. Therefore it is always the spectrum of the density fluctuations which is probed in a scattering experiment.

With the help of the KUBO formalism of linear-response theory [18] (for the present case see also [19]) and the fluctuation-dissipation theorem one may establish a relation between the dynamical structure factor $S(\mathbf{q}, \omega)$ and a quantity which is an actually more familiar one, namely the dielectric function $\epsilon(\mathbf{q}, \omega)$. This is an example of a very general principle in statistical physics, namely the fluctuation-dissipation theorem which always connects some sort of correlation function (the density-density correlation in this case) with a response function $\epsilon(\mathbf{q}, \omega)$ [20, 21]

$$S(\mathbf{q}, \omega) = \frac{q^2}{4\pi e^2} \frac{1}{1 - e^{-\beta\omega}} \text{Im} \left(-\frac{1}{\epsilon(\mathbf{q}, \omega)} \right).$$

For typical electronic excitation energies $\omega \gg 1/T$ and we may neglect the BOSE factor in the previous relation to obtain the final result

$$\frac{d^2\sigma}{d\Omega d\omega} = \frac{\text{const.}}{q^2} \text{Im} \left(-\frac{1}{\epsilon(\mathbf{q}, \omega)} \right), \quad (2.3)$$

which relates the intensity measured in an EELS experiment to the dielectric function $\epsilon(\mathbf{q}, \omega)$ the quantity which provides access to the electronic structure of a sample under investigation.

A brief remark is in order. The relation Eq. 2.3 is a typical one for spectroscopy where the intensity measured at the detector is always proportional to the imaginary part of a retarded GREEN'S $G(\mathbf{k}, \omega)$ function. Another typical example for this is photoemission where under certain approximations the current reads (see, e. g., Ref. 22)

$$\mathbf{j}(\mathbf{k}, \omega) \propto A(\mathbf{k}, \omega) = \text{Im } G(\mathbf{k}, \omega).$$

This can be understood because the spectral function $A(\mathbf{k}, \omega)$ in the photoemission case or the loss function in the case of EELS describe the distribution of possible excitations in the many-body system via the LEHMANN-representation [23] in the sense that each transition which can be observed as a peak (actually this corresponds to a pole of the Green's function) in an experiment carries a characteristic weight which is determined by the corresponding spectral function. The important consequence of this is that the experimental spectrum always yields only an *implicit* relation for the electronic structure $\omega(\mathbf{k})$ and as experimentalist one can only hope to make judgments on it by tracking the spectral function. In reality even this interpretation is often hampered by the influence of other factors like matrix elements.

2.4. The Dielectric Function

As it was shown in Sect. 2.3.2 (Eq. 2.3) it is the dielectric function $\epsilon(\mathbf{q}, \omega)$ which provides the main ingredient for the signal measured in an electron energy-loss spectroscopy-experiment. It is therefore instructive to introduce some of its properties which are particularly relevant for the later discussions. A relation which may be employed to define $\epsilon(\mathbf{q}, \omega)$ is

$$\mathbf{E}(\mathbf{r}, t) = \int d\mathbf{r}' \int dt \epsilon^{-1}(\mathbf{r}, \mathbf{r}', t - t') \mathbf{D}(\mathbf{r}', t').$$

On a macroscopic scale the system may be considered to be homogeneous and therefore the dielectric function depends only on the difference $\mathbf{r} - \mathbf{r}'$ which translates the above relation after a FOURIER transform into

$$\mathbf{E}(\mathbf{q}, \omega) = \epsilon^{-1}(\mathbf{q}, \omega) \mathbf{D}(\mathbf{q}, \omega). \quad (2.4)$$

From classical electrodynamics it is well known that the electric field \mathbf{E} and the displacement \mathbf{D} are caused by the total and external charges, respectively

$$i\mathbf{q} \cdot \mathbf{D}(\mathbf{q}, \omega) = \rho_{ext}(\mathbf{q}, \omega)$$

2. Electron Energy-Loss Spectroscopy

$$i\mathbf{q} \cdot \mathbf{E}(\mathbf{q}, \omega) = \rho_{tot}(\mathbf{q}, \omega),$$

where the total charge density is given by

$$\rho_{tot}(\mathbf{q}, \omega) = \rho_{ext}(\mathbf{q}, \omega) + \rho_{ind}(\mathbf{q}, \omega),$$

with the *a priori* unknown reaction of the system, contained in the induced charge density $\rho_{ind}(\mathbf{q}, \omega)$. With the relations given above it is however possible to connect it to the external sources (that are assumed to be known, by setting appropriate conditions in the laboratory) with the help of the dielectric function

$$\rho_{ind}(\mathbf{q}, \omega) = \left(\frac{1}{\epsilon(\mathbf{q}, \omega)} - 1 \right) \rho_{ext}(\mathbf{q}, \omega). \quad (2.5)$$

This is an important relation because it shows that in the case of vanishing $\epsilon(\mathbf{q}, \omega)$ the system hosts an intrinsic instability, i. e., there is a redistribution of the charges without an external driving force. It also shows that $\epsilon(\mathbf{q}, \omega)$ or more precisely $\epsilon^{-1}(\mathbf{q}, \omega)$ contains the response of the system to an external perturbation.

Another quantity of interest is the susceptibility

$$\chi(\mathbf{q}, \omega) = \frac{\rho_{ind}(\mathbf{q}, \omega)}{v_{ext}(\mathbf{q}, \omega)} \quad (2.6)$$

where $v_{ext}(\mathbf{q}, \omega)$ stands for the external potential that is created by the external charge density according to the POISSON equation. It is possible to relate the susceptibility to the dielectric function according to

$$\frac{1}{\epsilon(\mathbf{q}, \omega)} = 1 + v_q \chi(\mathbf{q}, \omega), \quad (2.7)$$

with $v_q = 1/q^2$ the FOURIER transform of the COULOMB potential. In the following we will describe some properties of $\epsilon(\mathbf{q}, \omega)$ or equivalently $\chi(\mathbf{q}, \omega)$ for a simple model of interacting electrons, namely the jellium which is at the heart of the so called random-phase approximation.

2.4.1. The Electron Gas In RPA

It is not the aim of this paragraph to give an extensive treatment of the subject because there are excellent and comprehensive reviews available (see, e. g., Refs. 24–29). The purpose is to introduce some ideas that will be of relevance in the subsequent discussion of the data. The starting point is the HAMILTONIAN for the jellium-model, i. e., the toy-model of electrons interacting with a homogeneous positive background. It reads

$$H = \sum_{\mathbf{k}} \omega_{\mathbf{k}} c_{\mathbf{k}}^{\dagger} c_{\mathbf{k}} + \sum_{\mathbf{k} \neq 0} \frac{2\pi e^2}{k^2} \left(\rho_{\mathbf{k}}^{\dagger} \rho_{\mathbf{k}} - N \right) = \sum_i \frac{p_i^2}{2m} + \sum_{\mathbf{k} \neq 0} \frac{2\pi e^2}{k^2} \left(\rho_{\mathbf{k}}^{\dagger} \rho_{\mathbf{k}} - N \right) \quad (2.8)$$

2.4. The Dielectric Function

with the single particle energies ω_k , the fermionic operators c_k , the density operator ρ_k given by Eq. 2.2 and the number operator N . With the help of the equation of motion

$$\ddot{\rho}_k = - [[\rho_k, H], H],$$

one may verify that

$$\ddot{\rho}_k + \omega_p^2 \rho_k = - \sum_i \left(\frac{\mathbf{k} \cdot \mathbf{p}_i}{m} + \frac{k^2}{2m} \right)^2 e^{-i\mathbf{k}r_i} - \sum_{q \neq k} \frac{4\pi e^2}{mq^2} \mathbf{q} \cdot \mathbf{k} \rho_{k-q} \rho_q \quad (2.9)$$

with the plasma frequency

$$\omega_p \equiv \sqrt{\frac{4\pi n e^2}{m}}, \quad (2.10)$$

which was first derived for classical plasmas in Ref. 30. The rather cumbersome Eq. 2.9 may be simplified by realizing that the first term on the right-hand side is of the order $(kv_F)^2 \rho_k$ and that the two coupled density oscillations in the second term will average to zero provided their phases are chosen *randomly*. This is what led BOHM and PINES [31] to introduce the term random-phase approximation (RPA) for this particular description. With this it is clear that the density of the electron gas will oscillate at a characteristic frequency ω_p pretty much like a harmonic oscillator provided that its wavelength is longer than a characteristic cutoff $1/q_c$

$$\frac{k^2 v_F^2}{\omega_p^2} \ll 1 \iff k^2 \ll q_c^2.$$

The quanta of these collective density fluctuations were first coined plasmons by DAVID PINES in Ref. 32. For higher momenta the collective motion of the electron gas as a whole loses its meaning and the individual properties of the single electrons become more important.

Instead of the density n which is actually the characteristic property of the electron gas it is another parameter which is often found in the literature, namely the WIGNER-SEITZ radius defined as

$$r_s = \frac{1}{a_0} \left(\frac{3}{4\pi n} \right)^{1/3}$$

with a_0 the BOHR radius. It measures the mean distance between two electrons in the system and it provides access to the ratio of the kinetic to the correlation energy. The latter point can be seen from the fact that the kinetic energy of the electrons scales with the FERMI energy according to

$$E_{kin} \sim E_F = \frac{k_F^2}{2m_0} \sim n^{2/3} \sim r_s^{-2}$$

2. Electron Energy-Loss Spectroscopy

whereas the correlation energy between the electrons scales with r_s^{-1} . Hence, it follows that

$$\frac{E_{kin}}{V_c} \sim \frac{E_F}{V_c} \sim \frac{r_s}{r_s^2} = \frac{1}{r_s} \xrightarrow{r_s \ll 1} \infty \iff n \rightarrow \infty$$

which means that in the high-density limit the kinetic energy dominates the correlation energy. This seems to be paradoxical at first sight because one would expect strong interactions between the electrons in a very dense plasma. Although this is of course the case (the correlation energy diverges in the high-density limit), it is overcompensated by the kinetic term as a consequence of the PAULI principle. It is however important to realize that the r_s -values for realistic metallic systems like the alkali metals lie in the range $r_s = 2 \dots 6$ [25]. Therefore one may expect some influences of the electron-electron interaction on the electronic properties already of simple metals (see the discussion on correlation effects in the next section).

Given its importance for the interpretation of the EELS spectra, the density-density correlation or susceptibility $\chi(\mathbf{q}, \omega)$ forms another quantity which is worth studying. It can be calculated with the help of Eq. 2.8 the result being

$$\chi(\mathbf{q}, \omega) = \frac{\chi^0(\mathbf{q}, \omega)}{1 - v_q \chi^0(\mathbf{q}, \omega)}$$

with the susceptibility of the non-interacting system

$$\chi^0(\mathbf{q}, \omega) = \frac{2}{V} \sum_{\mathbf{k}} \frac{n_{\mathbf{k}+\mathbf{q}}^0 - n_{\mathbf{k}}^0}{\omega - (\omega_{\mathbf{k}+\mathbf{q}}^0 - \omega_{\mathbf{k}}^0) + i\delta}, \quad (2.11)$$

where the $n_{\mathbf{k}}^0$ refer to the occupation numbers of the free system and $\delta \rightarrow 0^+$. Together with Eq. 2.7 the dielectric function in the RPA is given by

$$\epsilon(\mathbf{q}, \omega) = 1 - v_q \chi^0(\mathbf{q}, \omega)$$

which is frequently referred to as the LINDHARD function [33] in the literature. It has several important properties in both variables which shall be discussed briefly (an exhaustive treatment of its properties may be found in the references given at the beginning of this section and additionally in [34]).

From Eq. 2.5, Eq. 2.7 and the remarks made there it is clear that finding the zeros of $\epsilon(\mathbf{q}, \omega)$ or equivalently the points where $\chi^0(\mathbf{q}, \omega) = v_q^{-1}$ is of particular interest. For this Fig. 2.3 shows the behavior of $\text{Re} \chi^0(\mathbf{q}, \omega)$ as a function of energy. As can be seen there exists a dense manifold of poles whenever $\omega = \omega_{\mathbf{k}+\mathbf{q}}^0 - \omega_{\mathbf{k}}^0$. Between these singularities there are points which fulfill the required condition to produce a zero in $\epsilon(\mathbf{q}, \omega)$. These points contain the single-particle excitations, i. e., the formation of particle-hole pairs. But there is another solution which is outside the single-particle

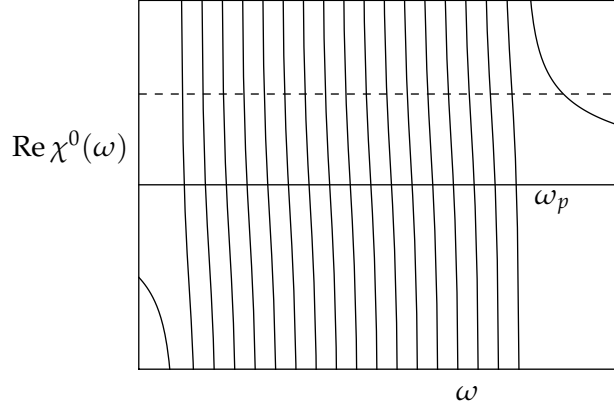


FIGURE 2.3.: The susceptibility as a function of energy. The horizontal dashed line indicates the position where $\text{Re } \chi^0(\omega) = 1/v_q$ corresponding to possible electronic transitions. There is a very dense manifold of them corresponding to single-particle excitations and a collective mode—the plasmon—lying at ω_p .

continuum at higher energies which corresponds to a collective excitation in the electron gas. This is the plasmon mentioned above.

Furthermore, the susceptibility $\chi(\mathbf{q}, \omega)$ has (with respect to the energy variable) the typical property of a retarded GREEN'S function of being analytic in the upper half plane which it transmits via Eq. 2.7 also to the dielectric function. [‡] As a consequence of this the real and imaginary parts of $\text{Im}(-1/\epsilon(\omega))$ are connected via the well known KRAMERS-KRONIG relations

$$\begin{aligned} \text{Re} \left(\frac{1}{\epsilon(\mathbf{q}, \omega)} \right) - 1 &= \frac{1}{\pi} \mathcal{P} \int d\omega' \left[\frac{\text{Im} \left(\frac{1}{\epsilon(\mathbf{q}, \omega')} \right)}{\omega' - \omega} \right] \\ \text{Im} \left(\frac{1}{\epsilon(\mathbf{q}, \omega)} \right) &= -\frac{1}{\pi} \mathcal{P} \int d\omega' \left[\frac{1 - \text{Re} \left(\frac{1}{\epsilon(\mathbf{q}, \omega')} \right)}{\omega' - \omega} \right], \end{aligned} \quad (2.12)$$

which are an indispensable tool to deduce the complete dielectric function from the signal measured in the EELS spectrometer. With this at hand it is possible to derive, in principle, all optical constants like, e. g., the refractive index, the optical conductivity etc. [35]. It is, however, important to stress that for $q \neq 0$ the KRAMERS-KRONIG relations (Eq. 2.12) which are ubiquitous in the spectroscopic literature hold for the inverse of the dielectric function but *not* for $\epsilon(\mathbf{q}, \omega)$ itself because only $1/\epsilon(\mathbf{q}, \omega)$ fulfills the requirement

[‡]This is the reason why it is possible to identify the zeros of $\epsilon(\mathbf{q}, \omega)$ as transitions in the many-particle system which are always given as poles of a "suitable" GREEN'S function.

2. Electron Energy-Loss Spectroscopy

of a true response function, namely being determined entirely by *external* sources (cf. Eq. 2.5) that can be switched on and off at will. [§]

Besides the KRAMERS-KRONIG equations there exist more relations that are important for the evaluation of data as well as for the interpretation of theoretical models. They come in the shape of particular sum rules. The the most prominent one reads

$$\int_0^\infty d\omega \omega \operatorname{Im} \left(-\frac{1}{\epsilon(\mathbf{q}, \omega)} \right) = \frac{\pi}{2} \omega_p^2, \quad (2.13)$$

and it states that the strengths of possible transitions are not independent from each other but are balanced in such a way that enhancing the weight in a particular energy range of the spectrum by, e. g., the appearance of a phase transition will reduce the intensity in another energy window to keep the above given integral at a constant value. In practice, calculations as well as experiments are of course always restricted to a finite energy window and one may evaluate partial sum-rules according to

$$\int_{\omega_0}^{\omega_1} d\omega \omega \operatorname{Im} \left(-\frac{1}{\epsilon(\mathbf{q}, \omega)} \right) = \frac{\pi}{2} \omega_p^2 (n_{eff}/n), \quad (2.14)$$

that provide access to an effective number of charge carriers n_{eff} contributing to a particular type of excitation within a given energy range.

Concerning the momentum dependence of the LINDHARD function there is a peculiarity related to the dimensionality of the system. Evaluating the \mathbf{k} -sum in Eq. 2.11 results in different structures for the susceptibility with the most interesting behavior occurring for the one-dimensional electron gas [40] (see Fig. 2.4). In this case the FERMI “surface” consists only of two points separated by $2\mathbf{k}_F$ from each other and this leads to a strong singularity in the susceptibility. From Eq. 2.6 it can be seen that this scenario corresponds to the appearance of a spontaneous redistribution of the electron density—a so called charge-density wave (CDW)—in the system which was first predicted by PEIERLS in 1956 [41]. To avoid this singularity the system opens a gap at the FERMI surface and this is an archetypical route for a metal-insulator—in this case the so called PEIERLS—transition, a cartoon of which is shown in Fig. 2.5 for the particular case of a monoatomic chain with a half-filled band. Besides the electronic spectrum also other quasi-particle branches of a solid are effected by this singularity. Most prominently there appears a so called KOHN anomaly [42] which is a softening of the phonon mediating the transition from $-\mathbf{k}_F$ to \mathbf{k}_F . As can be seen from Fig. 2.4 for higher dimensions the effect is strongly reduced but may still be present whenever

[§]This has, among others, important consequences for possible (but so far only speculative) electronic mechanisms of superconductivity (see, e. g., Refs. 36, 37) which are a matter of long-term arguments between the students of V. L. GINZBURG from the LEBEDEV institute in Moscow and P. W. ANDERSON (for recent examples see Refs. 38, 39).

2.4. The Dielectric Function

the FERMI surface contains a substantial portion (a finite measure in the sum Eq. 2.11) of parallel segments that can be connected by a single \mathbf{q} vector. This scenario is called nesting and we will come back to this point in Ch. 4. In contrast to the perfect gapping of the electronic excitation spectrum occurring in 1D, in this case only the portions of the FERMI surface connected by the ordering vector \mathbf{q} become gapped which results in a so called pseudogap—an only partial suppression of the density of states at the FERMI level. Still, this is considered one of the prototypical routes to turn a metal into an insulator in 2D.

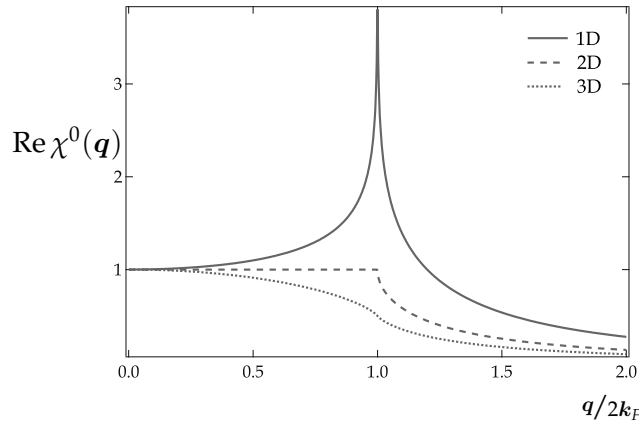


FIGURE 2.4.: The static susceptibility (Eq. 2.11) evaluated for different dimensions. Note the strong peak which is present for the one-dimensional case but missing for higher dimensions.

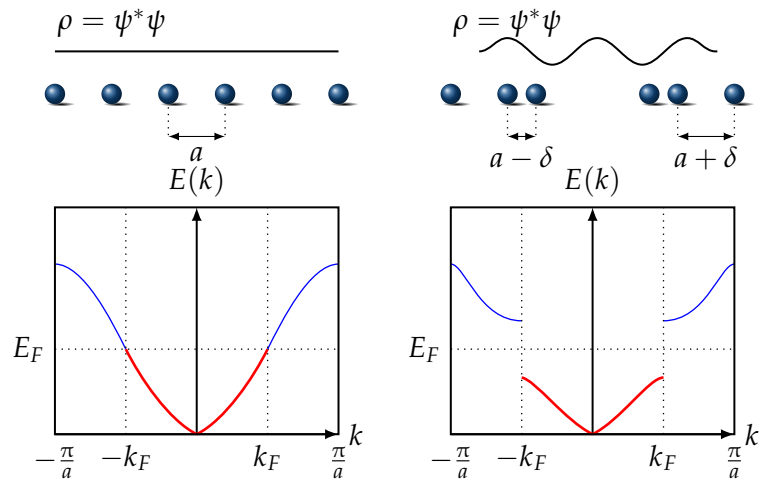
A feature of special relevance for the later discussions is the momentum dependence of the plasma frequency, i. e., the plasmon dispersion which can be derived from the LINDHARD function under some assumptions. Expanding Eq. 2.11 yields (see, e. g., [25, 43])

$$\omega(\mathbf{q}) = \omega_p + \alpha \mathbf{q}^2 + \mathcal{O}(\mathbf{q}^4) \quad \alpha = \frac{3}{5} \frac{E_F}{\omega_p} \propto v_F^2. \quad (2.15)$$

This is the generic behavior of the collective modes in the RPA and there are numerous examples in the literature, that this is also realized for real materials. We will however observe and discuss partly remarkable deviations from this functional form in the following chapters. The intuitive reasoning for the positive plasmon velocity $\nabla_{\mathbf{q}} \omega_{\mathbf{q}}$ is the fact that it costs energy to compress the electron gas for shorter distances, i. e., higher momenta.

To conclude this section Fig. 2.6 summarizes the most important results for the relation between the single-particle and collective modes in the RPA. There is a continuum of particle-hole excitations which scales quadratically with momentum (due to the

2. Electron Energy-Loss Spectroscopy



2.5.1: The linear chain (undistorted) 2.5.2: The linear chain (distorted)

FIGURE 2.5.: Schematic view of the PEIERLS transition in 1D. The linear arrangement of the atoms in the left panel becomes unstable for the case of a half-filled band leading to a doubling of the unit cell accompanied by the appearance of a characteristic modulation of the charge density ρ (right panel).

implicitly assumed spherical FERMI surface) and a collective (optical, offset by the plasma frequency Eq. 2.10) mode—the plasmon—which is also quadratic in q and propagates freely without any damping up to a critical wave vector q_c where it starts to decay into particle-hole pairs.

2.4.2. Effects Beyond RPA

Of course the foregoing discussion of the RPA behavior of the electron gas is not the end of the story and real materials show a number of properties that may complicate a theoretical treatment significantly. Here we will briefly touch upon some of them which are of relevance for the later discussions. The first one will be the effect of correlations, i. e., electron-electron interaction and the second crystal local field effects. Unfortunately in the literature the nomenclature is misleading because both effects are often termed local field effects due to their shared feature of becoming more important for higher values of momentum, i. e., higher “locality”. Nevertheless they originate from entirely different physical phenomena, the former from the PAULI principle and the latter from the crystal structure of a solid and in order not to be too confusing here we will talk about correlation and local field effects, respectively.

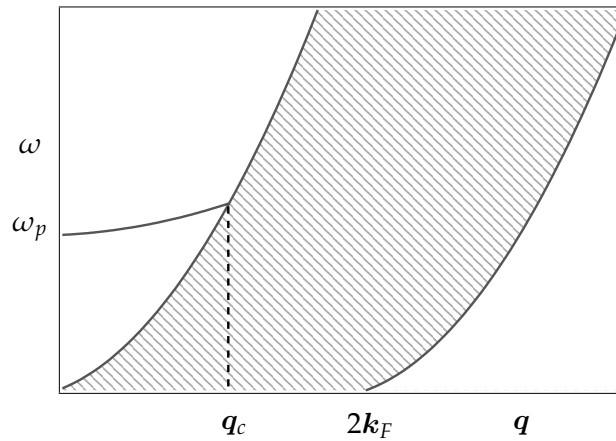


FIGURE 2.6.: The (\mathbf{q}, ω) -plane and the relation between the plasmon mode (solid line) and the single particle continuum (hatched area). In the RPA the plasmon exists only up to a critical momentum q_c where it enters the continuum and decays into particle-hole pairs.

Correlations

It was mentioned above that the EELS experiment basically probes the fluctuations in the density of the electron system and the essential quantity which characterizes those fluctuations in reciprocal space is the dynamical structure factor $S(\mathbf{q}, \omega)$. Of course it is possible to FOURIER transform this quantity to real space and the result of this is the dynamic pair distribution function

$$G(\mathbf{r}, t) = \int d\mathbf{q} d\omega e^{-i(\mathbf{q}\mathbf{r} - \omega t)} S(\mathbf{q}, \omega)$$

which

“In all cases ... describes the correlation between the presence of a particle in position $\mathbf{r}' + \mathbf{r}$ at time $t' + t$ and the presence of a particle in position \mathbf{r}' at time t' , averaged over \mathbf{r}' .” [17]

It is clear that for increasing momentum transfer the wavelength of the density fluctuations under investigation become shorter and one therefore probes more and more local properties. As a consequence the PAULI principle and the electron-electron repulsion become more and more effective leading to the exchange-correlation hole: around an electron the probability to find another electron is strongly reduced. This naturally reduces the density, or in other (classical) words the spring constant in Eq. 2.9, i. e., the plasma frequency becomes reduced for non-zero q which leads to deviations from the generic quadratic RPA plasmon dispersion. As a consequence in general there appears

2. Electron Energy-Loss Spectroscopy

a softening of the plasmon velocity $\nabla_{\mathbf{q}}\omega(\mathbf{q})$ for large momenta. Neglecting those effects yields negative values for the static pair distribution function $G(\mathbf{r}) = \int dt G(\mathbf{r}, t)$ which is of course an unphysical value and provides together with the violation of the compressibility sum rule [28, 44] severe shortcomings of the RPA approach. There are of course numerous efforts to incorporate those effects into a proper theoretical treatment of the electron gas. We will come back to this point in Sect. 4.3 when discussing the plasmon dispersion in the transition-metal dichalcogenides.

Crystal Local Fields

The reasoning which led to Eq. 2.4 is no longer justified for a periodic solid where the symmetry is lowered to that of the underlying BRAVAIS lattice. Naturally this has also consequences for the optical properties of a solid which were first studied by EHRENREICH, COHEN [45], ADLER [46] and WISER [47]. The periodicity within a crystal leads to the condition

$$\epsilon(\mathbf{r}, \mathbf{r}', t) = \epsilon(\mathbf{r} + \mathbf{R}, \mathbf{r}' + \mathbf{R}, t)$$

for the dielectric function with \mathbf{R} a lattice vector. The appearance of different bands in a solid together with the existence of the reciprocal lattice lead to a more cumbersome expression for the susceptibility in Eq. 2.11 which now reads

$$\begin{aligned} \chi_{GG'}(\mathbf{q}, \omega) &= \frac{2}{V} \sum_{n, n', \mathbf{k}} \langle n', \mathbf{k} | e^{-i(\mathbf{q} + \mathbf{G})\mathbf{r}} | n, \mathbf{k} + \mathbf{q} \rangle \langle n, \mathbf{k} + \mathbf{q} | e^{-i(\mathbf{q} + \mathbf{G}')\mathbf{r}'} | n', \mathbf{k} \rangle \times \\ &\times \frac{f(\omega_{n, \mathbf{k} + \mathbf{q}}) - f(\omega_{n', \mathbf{k}})}{\omega - (\omega_{n, \mathbf{k} + \mathbf{q}} - \omega_{n', \mathbf{k}}) + i\delta} \end{aligned} \quad (2.16)$$

with the notation $\chi_{GG'}(\mathbf{q}, \omega) \equiv \chi(\mathbf{q} + \mathbf{G}, \mathbf{q} + \mathbf{G}', \omega)$. In contrast to Eq. 2.11 the single particle energies carry now a band index n and the numerator (f stands for the FERMI function) is supplemented by matrix elements between the different BLOCH states $|n, \mathbf{k}\rangle$. From this the dielectric function follows to be

$$\epsilon_{GG'}^{-1}(\mathbf{q}, \omega) = \delta_{GG'} + v_{\mathbf{q} + \mathbf{G}} \chi_{GG'}(\mathbf{q}, \omega),$$

which leads to a more complex expression for the electric field \mathbf{E}

$$\mathbf{E}(\mathbf{q} + \mathbf{G}, \omega) = \sum_{\mathbf{G}'} \epsilon_{GG'}^{-1}(\mathbf{q}, \omega) \mathbf{D}(\mathbf{q} + \mathbf{G}', \omega).$$

Therefore a monochromatic external source $\mathbf{D}(\mathbf{q}, \omega)$ (or the corresponding external charge density) creates microscopic electric fields with the same frequency but different spatial components on length scales of the unit cell. The field-components with $\mathbf{G} \neq \mathbf{G}'$

are called crystal local field effects. For small values of momentum one averages over several unit cells the result being the macroscopic response given by

$$\epsilon(\mathbf{q}, \omega) = \frac{1}{\epsilon_{\mathbf{G}\mathbf{G}'}^{-1}(\mathbf{q}, \omega)|_{\mathbf{G}=\mathbf{G}'=0}}.$$

This means in particular that for higher values of q one cannot, in general, neglect the influence of the lattice potential and one has to take the crystal local field effects into account [48]. From the experimental point of view caution is always required as these processes are known to modify peak positions and heights upon leaving the center of the BRILLOUIN zone [49]. From Eq. 2.16 one can however see that these effects are characteristic features of a particular crystal- and the resulting band-structure and one may therefore expect that similar compounds are subject to similar crystal local field effects.

2.4.3. The Drude-Lorentz-Model

After the more general arguments in the last section we will now discuss a particular model for the energy dependence of the dielectric function in a solid, namely the DRUDE-LORENTZ-model [35, 50]. Though very simple it is nevertheless widely employed as it provides an easy understanding of the physical processes behind optical properties and the vocabulary for their description. In addition it has the advantage of following the causality principle in the sense that the real and imaginary parts automatically fulfill the KRAMERS-KRONIG relations Eq. 2.12. There are of course refinements to it—the so called extended DRUDE-model—but we will not employ this here (see however Ref. 51 for an introduction).

The starting point for the treatment within the (conventional) DRUDE-LORENTZ-model is a classical ansatz for the electron movement assuming them to be describable by a driven harmonic oscillator where the external field forms the inhomogeneity in the equation of motion, i. e., the driving force oscillates with a characteristic frequency ω . The outcome of the straightforward calculation for the dielectric function is

$$\epsilon(\omega) = 1 + \omega_p^2 \sum_i \frac{f_i}{\omega_{i_0}^2 - \omega^2 - i\gamma_i \omega}.$$

Here the f_i are the oscillator strengths that measure the transition probability in the dipole regime according to

$$f_i = 2\omega_{i_0} |\mathcal{M}_i|^2 \quad \mathcal{M}_i = \langle i | \mathbf{r} | 0 \rangle = \int d\mathbf{r} \varphi_i^* \mathbf{r} \varphi_0$$

2. Electron Energy-Loss Spectroscopy

where $|0\rangle$ and $|i\rangle$ are considered to be BLOCH states in the case of a solid, $\omega_{i_0} \equiv \omega_i - \omega_0$ describes the energy of the transition and the γ_i are the dampings of the excitations, i. e., their inverse lifetimes. As can be seen $\epsilon(\omega) \in \mathbb{C}$ and we can split it according to

$$\begin{aligned}\epsilon_1(\omega) &= 1 + \omega_p^2 \sum_i \frac{f_i(\omega_{i_0}^2 - \omega^2)}{(\omega_{i_0}^2 - \omega^2)^2 + \gamma_i^2 \omega^2} \\ \epsilon_2(\omega) &= \omega_p^2 \sum_i \frac{f_i \gamma_i \omega}{(\omega_{i_0}^2 - \omega^2)^2 + \gamma_i^2 \omega^2},\end{aligned}$$

In the special case of a metallic system the electrons are assumed to be free, i. e., $\omega_0 \equiv 0$ which reduces the above equations to

$$\begin{aligned}\epsilon_1(\omega) &= 1 - \omega_p^2 \sum_i \frac{f_i}{\omega^2 + \gamma_i^2} \\ \epsilon_2(\omega) &= \omega_p^2 \sum_i \frac{f_i \gamma_i}{\omega(\omega^2 + \gamma_i^2)}.\end{aligned}$$

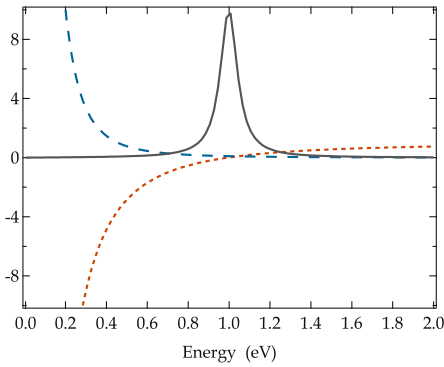
and Fig. 2.7 summarizes the qualitative behavior of the three quantities $\epsilon_1(\omega)$, $\epsilon_2(\omega)$ and $\text{Im}(-1/\epsilon(\omega))$ for a single oscillator. The most important feature is that for a non-metallic system the peak in the loss function does not necessarily correspond to the value of the true transition at $\omega = \omega_0$ which can be seen from the condition

$$\text{Im}\left(-\frac{1}{\epsilon(\omega)}\right) = \frac{\epsilon_2(\omega)}{\epsilon_1^2(\omega) + \epsilon_2^2(\omega)} \xrightarrow[\epsilon_1(\omega)=0]{\epsilon_2(\omega) \ll 1} \infty.$$

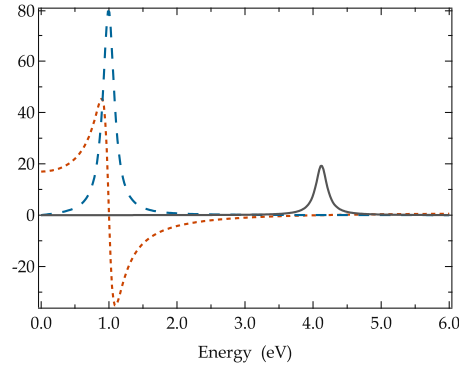
The exact position of the loss function peak can be evaluated according to

$$\frac{d}{d\omega} \text{Im}\left(-\frac{1}{\epsilon(\omega)}\right) \stackrel{!}{=} 0 \quad \xleftrightarrow{\gamma \rightarrow 0} \quad \omega = \sqrt{\omega_0^2 + \omega_p^2} \stackrel{\omega_0 \ll \omega_p}{=} \omega_p, \quad (2.17)$$

which in this case (vanishing damping) corresponds exactly to the second zero of $\epsilon_1(\omega)$. For a metallic system the loss function peaks exactly at $\omega = \omega_p$ which is also the point where $\epsilon_1(\omega) = 0$, in agreement with what has been said on the general properties of the electron gas in the last section. Another subtlety of the loss function is the fact that in contrast to ϵ_2 (and quantities derived therefrom, in particular the optical conductivity) $\text{Im}(-1/\epsilon(\omega))$ is *not* simply a linear superposition of two oscillators, i. e., two neighboring transitions are decoupled in ϵ_2 but they do interfere with each other in $\text{Im}(-1/\epsilon(\omega))$ in a way that depends on the values of the parameters in the DRUDE-LORENTZ-MODEL. As a rule of thumb one can keep in mind that they always try to repel each other.



2.7.1: The dielectric function of a metal



2.7.2: The dielectric function of an insulator

FIGURE 2.7.: The loss function $\text{Im}(-1/\epsilon(\omega))$ (solid line), ϵ_1 (short dashed line) and ϵ_2 (long dashed line) for a single oscillator as a function of energy in the DRUDE-LORENTZ-Model. The model parameters are $\omega_0 = 0, \omega_p = 1 \text{ eV}, \gamma = 0.1 \text{ eV}$ (left panel) and $\omega_0 = 1 \text{ eV}, \omega_p = 4 \text{ eV}, \gamma = 0.2 \text{ eV}$ (right panel). In both cases $f_i = 1$ as the oscillator strengths obey the sum rule $\sum_i f_i = 1$ [50].

2.5. Experimental Details

This part intends to give an at least brief account of what constitutes actually the main part of the work, namely the everyday business in the laboratory. ^{||}

2.5.1. The Spectrometer

The experimental setup employed is a purpose-built transmission electron energy-loss spectrometer developed and constructed mainly by J. FINN [52]. It became very famous by enlightening the doping mechanism in high- T_c superconductors [53] and has, since then, proved to be a valuable tool for investigations on a number of issues related to the electronic structure of solids (for an incomplete overview see, e. g., [54]) partly due to some specialties it has making it particularly appropriate for the desired investigations:

- high energy and momentum resolution (see Fig. 2.9)
- sample on ground potential \Rightarrow easy sample exchange and manipulation
- possibility of *in situ* intercalation

As a detailed description of the spectrometer is far beyond the scope of the present work, only the main features shall be addressed here. For an elaborate discussion see

^{||}According to I. Y. POMERANCHUK the book of physics has two volumes: volume one is pumps and manometers and volume two is quantum field theory. As an experimentalist one routinely faces volume one often leaving not enough time to deal with volume two.

2. Electron Energy-Loss Spectroscopy

[52]. The main parts can be seen in Fig. 2.8. The electron source consists of a tungsten

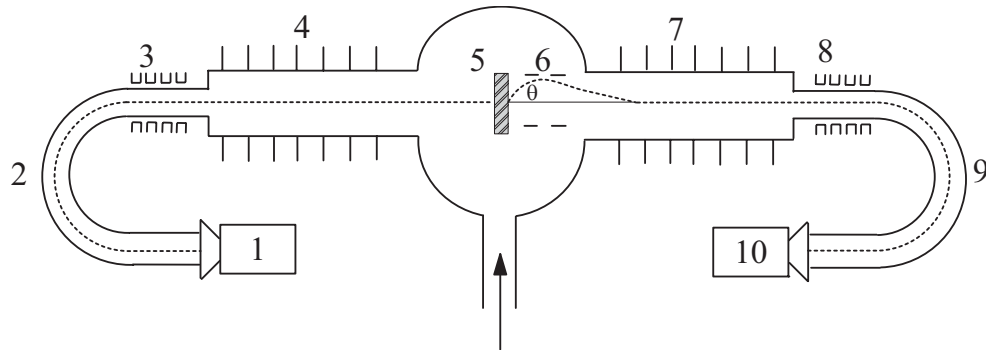


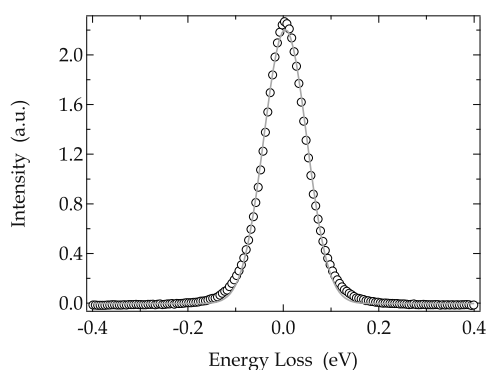
FIGURE 2.8.: The EELS spectrometer (schematically) according to Ref. 52: electron source (1); monochromator (2); zoom lenses (3,8); accelerator (4); sample (5); deflection plates (6); decelerator (7); analyzer (9); detector (10) The arrow indicates the fast entry for the samples.

cathode followed by a lens system that focuses the electron beam on the entrance of the monochromator. Afterward the electron beam is guided by so called zoom lenses to the accelerator producing the high value of incoming energy $E_0 = 172$ keV. Momentum selectivity is achieved by two pairs of horizontal and vertical deflection plates, the voltage of which can be directly translated into momentum transfer, forcing the scattered electrons back on the optical axis. After being decelerated the electrons reach the analyzer and finally the detector where a photo multiplier produces the signal transferred to the computer.

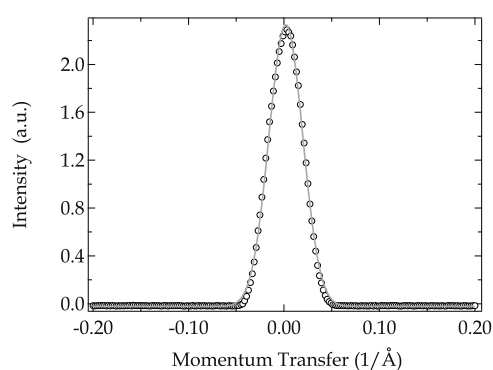
In addition to what is shown in Fig. 2.8 in the course of this work a helium flow-cryostat was installed on the spectrometer which allows to measure in a temperature range $T \approx 20 \dots 400$ K. It is possible to employ different beam characteristics for optimal investigations on distinct types of electronic excitations (valence or core transitions). The settings required for a certain beam are stored in files containing all necessary adjustments for the power supplies, deflection plates and so on. Nevertheless each beam is tuned before a new sample is loaded for best possible performance and Fig. 2.9 shows the properties of the beam that was used to collect the majority of the experimental data shown in the following.

2.5.2. Sample Preparation

From Fig. 2.1 it is obvious that the experiments are performed in a transmission geometry. Therefore having thin samples (with a thickness of only about 100 nm) forms an issue of particular importance and is the main criterion whether or not a system can be investigated by electron energy-loss spectroscopy. There are several possibilities to



2.9.1: Energy Resolution



2.9.2: Momentum Resolution

FIGURE 2.9.: The energy and momentum resolution curves for the pure electron beam (without sample). The data are fitted to GAUSSIANS (solid lines). The obtained FWHM values are $\Delta E \approx 65$ meV and $\Delta q \approx 0.03 \text{ \AA}^{-1}$, respectively.

obtain the required thickness of the films depending on the microscopic structure of the particular compound. For the present work samples were prepared either by cutting thin slices from a macroscopic single crystal with the help of an ultramicrotome—a special device allowing precise cuts with the help of a diamond knife—or cleaved with the help of adhesive tape which was afterwards dissolved in acetone. In all cases the films are put on standard electron-microscopy grids (see Fig. 2.10), mounted in a sample holder and then transferred to the spectrometer.

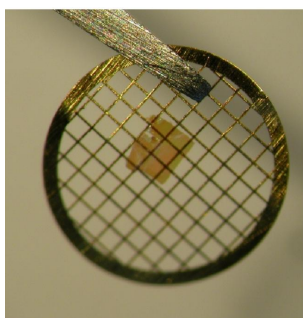


FIGURE 2.10.: A typical snapshot of a single crystal placed on a standard TEM grid (diameter of ≈ 5 mm) intended for usage in the EELS spectrometer. The image shows a TiOCl sample prepared with the help of adhesive tape and is reproduced here with kind permission from R. KRAUSS.



3. EELS On Underdoped Cuprates

3.1. Introduction

GIVEN the myriad of publications and known facts about cuprates one may ask whether it is possible to add anything new to their story which has not been said already in one or the other way. In fact since their discovery by BEDNORZ and MÜLLER [55] the cuprates have become *the* paradigm for a lot of—now already longstanding—topics in condensed matter physics and triggered tremendous developments in the theoretical treatment of solids, accompanied by remarkable progress of important experimental issues like the growth of high-quality single crystals and spectrometer performance.

However, somebody new to the field will quickly realize that the puzzle is not yet solved. Instead he will perhaps get the feeling that the truth seems to be hidden behind some magical curtain: There appear “pseudo”-gaps, cuprates are “unconventional” superconductors which show “anomalous” behavior not only in their “strange”-metal phase to mention just a few of the phrases that appear ubiquitously in the literature. In addition there are considerable arguments in particular about the mechanism behind the superconductivity with a strong party in favor of spin-mediated pairing (see, e. g., [56, 57] for recent reports) arguing a lot with the advocates of phonons (see [58] for a recent comprehensive summary) and there is also a, though smaller, community favoring electronic excitations (for an introduction [59]) as the mediator between the electrons.*

All these things are basically driven by low-energy physics occurring in the vicinity of the FERMI surface. In the following we will—for most of the time—focus on processes that happen on a higher energy scale on the order of some eV and only occasionally have reason to come back to this “low-energy battlefield”. Still, we will also find “anomalous” behavior that has been unknown so far to the cuprates story.

*There is a joke alleged to have circulated in the community in the early days of the cuprates hype that nicely captures the existing rivalries: Two high- T_c researchers are sentenced to death but each of them is allowed to express one last wish in front of the king. Researcher number one says: “His Majesty, I will readily disappear from mother earth, but before that, please, let me explain you my point of view about the cuprates.” This causes researcher number two to jump up and beg: “Oh no, please kill me first!”

3. EELS On Underdoped Cuprates

3.2. Electronic Properties Of The Cuprates

This is a vast field and still a matter of intense debate. Therefore we will not even try to cover it to any satisfactory level of completeness. A more exhaustive overview can be found in numerous reviews, e. g., [60–63].

The crystal structures of two archetypal representatives of the different cuprate families— $\text{Ca}_{2-x}\text{Na}_x\text{CuO}_2\text{Cl}_2$ and $\text{La}_{2-x}\text{Sr}_x\text{CuO}_4$ —are shown in Fig. 3.1. Though they differ in some respects (the former contains a rare-earth element, the latter does not) they exhibit all the features the cuprates became famous for. They are layered perovskite-like materials with rather complex unit cells consisting of numerous atoms all sharing the main ingredient of the cuprates mystery: the CuO_2 plane. To be more precise in $\text{La}_{2-x}\text{Sr}_x\text{CuO}_4$ there is an octahedron of oxygen atoms surrounding the copper site. This led to the initial belief that the additional apical oxygens are of relevance for the mechanism of high-temperature superconductivity (HTSC) in the cuprates as also other families show this structural subtlety. But the detection of superconductivity in $\text{Ca}_{2-x}\text{Na}_x\text{CuO}_2\text{Cl}_2$ at $T_c \sim 25$ K [64] clearly showed that the essentials are hidden within the 2D arrangement of the copper and oxygen atoms which will be discussed below.

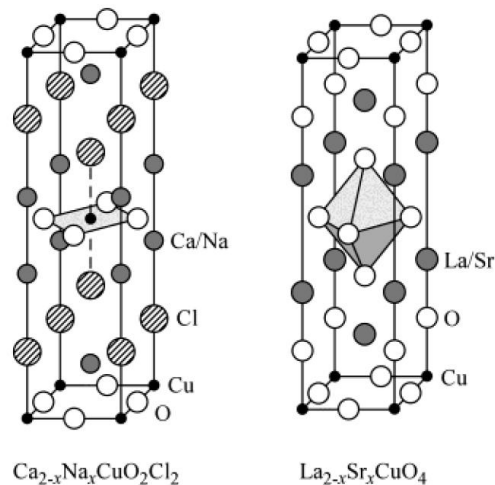


FIGURE 3.1.: The crystal structure of $\text{Ca}_{2-x}\text{Na}_x\text{CuO}_2\text{Cl}_2$ and $\text{La}_{2-x}\text{Sr}_x\text{CuO}_4$. Both compounds are nearly identical except for the missing apical oxygen in the $\text{Ca}_{2-x}\text{Na}_x\text{CuO}_2\text{Cl}_2$. Image taken from Ref. 65.

In a purely ionic picture one may simply count the valencies in the undoped La_2CuO_4 system to realize that Cu is in a $3d^9$ configuration, i. e., a single hole is left in an otherwise completely filled d -shell. Due to the presence of the crystal field the d -levels which are degenerate in free space split and as it turns out [66] the remaining

3.2. Electronic Properties Of The Cuprates

hole is primarily of $d_{x^2-y^2}$ character. Now, in the band picture of simple metals the result would be a half-filled band leading to a metallic ground state. However, this is not what is observed in the undoped cuprates. Instead they are insulators [67] with antiferromagnetic order [68] which disappears only well above room-temperature. This clearly points to the breakdown of simple band theory in this case and signals the presence of strong electron-electron interactions. It was MOTT who introduced the concept of a metal-insulator transition driven by electron-electron interaction which is nowadays called a MOTT insulator [69] and the drosophila for its theoretical treatment is the single-band HUBBARD model

$$H = - \sum_{i,j,\sigma} t_{ij} c_{i,\sigma}^\dagger c_{j,\sigma} + U \sum_i n_{i,\sigma} n_{i,-\sigma}$$

pioneered by GUTZWILLER, KANAMORI and HUBBARD. The operators $c_{i,\sigma}^{(\dagger)}$ annihilate (create), in this case, a hole on lattice site i with spin projection σ and $n_{i,\sigma} = c_{i,\sigma}^\dagger c_{i,\sigma}$ counts the electrons on a particular site. The two parameters in the model are the hopping term t and the famous HUBBARD U which mimics the COULOMB interaction of the electrons. Depending on their ratio one may distinguish three different regimes for the single-particle spectral function shown in Fig. 3.2. In the non-interacting case $W \gg U$ there exists a quasiparticle band of width $W \propto t$ around the FERMI level which becomes weakened upon increasing U —accompanied by the appearance of satellite features at finite energy—and finally totally absent in the strong-coupling regime $W < U$ where there appear well separated lower (occupied) and upper (unoccupied) HUBBARD bands. It is exactly this disappearance of quasiparticle weight that causes the MOTT transition for interactions larger than some critical value on the order of the bandwidth.

Experimentally the ratio t/u may be altered in a number of different ways. Typical approaches are either chemical or mechanical pressure to change predominantly the numerator or doping which, in a first approximation, lowers the denominator by screening the HUBBARD term via the presence of additional charge carriers.

Naturally this has important consequences for all experimental probes, in particular for the optical response. In the framework of dynamical mean-field theory (DMFT) which provides an exact description of strong-correlation physics (at least in the limit of infinite dimensions) [70] the optical conductivity may be written as the auto-correlation of the single-particle spectral function $A(\omega)$

$$\sigma(\omega) \propto \frac{t^2}{\omega} \int_{-\infty}^{\infty} d\omega' A(\omega') A(\omega' + \omega) [n_F(\omega') - n_F(\omega' + \omega)]$$

which was extensively studied in Refs. 71, 72. For the non-interacting case the optical response consists of a well-defined DRUDE peak centered at zero energy caused by the

3. EELS On Underdoped Cuprates

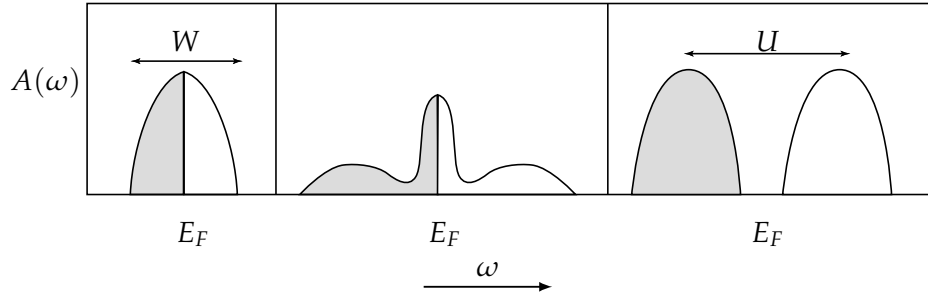


FIGURE 3.2.: A schematic view of the metal-insulator transition in the single-band HUBBARD model. For $W \gg U$ (left panel) there is a well defined quasiparticle peak in the single-particle spectral function $A(\omega)$. In the intermediate regime $W \approx U$ (middle panel) there appear satellite structures which develop into the upper and lower HUBBARD band for $W < U$ (right panel). Shaded regions correspond to the occupied part of the spectrum.

intra-band transitions within the quasiparticle band. On the contrary, in the strong-coupling limit ($U \gg W$) there is a pronounced charge gap and the response consists of a very broad and incoherent feature reflecting the electronic transitions from the lower to the upper HUBBARD band. In the intermediate case the DRUDE and HUBBARD features are supplemented by transitions between the HUBBARD bands and the quasiparticle branch which results in a characteristic three-peak structure. In the cuprates community the third feature has been termed mid-infrared peak due to its energetic position.

Though, the exact strength of the correlations in the cuprates is still a matter of debate [73] there is consensus that indeed U is by far the largest energy scale in the problem ([61, 66]). This means that the cuprates may be approached from the strong coupling side and one may therefore perform a perturbative treatment of the HUBBARD model in the small parameter $t/u \ll 1$ which, in second order, yields the $t - J$ -model

$$H = - \sum_{i,j,\sigma} t_{i,j} \tilde{c}_{i,\sigma}^\dagger \tilde{c}_{j,\sigma} + J \sum_{i,j} \left(\mathbf{S}_i \cdot \mathbf{S}_j - \frac{1}{4} n_i n_j \right)$$

with $J = 4t^2/u$. Here a double occupancy of a site is explicitly forbidden by the projected hopping operators $\tilde{c}_{j,\sigma} = c_{j,\sigma}(1 - n_{j,-\sigma})$ (see, e. g., [66, 74]). Though a system described by this model is highly correlated the kinetic energy term proportional to t still plays an important role as it establishes an antiferromagnetic order. This is caused by a lowering of the total energy of the system via virtual hopping processes between neighboring sites that are only possible in the case of alternating spins on adjacent copper atoms thereby favoring the antiferromagnetic alignment of the copper spins [74]. All this makes the HUBBARD model or its strong-coupling cousin the $t - J$ -model very appealing as they are obviously able to predict many of the features observed experimentally in

3.2. Electronic Properties Of The Cuprates

the cuprates and they therefore confirm what P. W. ANDERSON initially supposed [75]. Nevertheless the story is actually much more involved and this is due to the strong hybridization of the copper with the oxygen degrees of freedom.

In a seminal paper which appeared already before the discovery of the cuprates ZAA-NEN, SAWATZKY and ALLEN suggested a classification of transition-metal oxides which characterizes different compounds not only in terms of the hopping matrix element t and the value of the HUBBARD U but also with the help of an additional parameter, the so called charge-transfer energy Δ which measures the difference between the highest occupied oxygen level and the lowest unoccupied level of the transition-metal ion. In a conventional MOTT insulator $\Delta > U$ and one can indeed consider the rather narrow and therefore strongly correlated (un)occupied transition metal $3d$ orbitals as the (upper) lower HUBBARD bands, respectively. In the opposite case, however, when $\Delta < U$ there is a broad and uncorrelated oxygen $2p$ manifold which separates the two HUBBARD branches. One therefore describes compounds showing this behavior more precisely as charge-transfer insulators as in this case the lowest possible electronic transitions occur between oxygen and the transition metal and therefore imply a transfer of charges between the anion and the cation.

In the beginning of the research on the cuprates it was not clear whether they fall in one or the other regime. However, high-energy spectroscopy helped to clarify the situation. Employing EELS it was possible to show that doping holes which effectively moves the chemical potential towards the occupied part of the spectrum strongly effects the oxygen edges while leaving the copper states mostly unaffected. This was the experimental proof that the lowest hole addition states are predominantly of oxygen character classifying the cuprates as charge-transfer insulators [53].

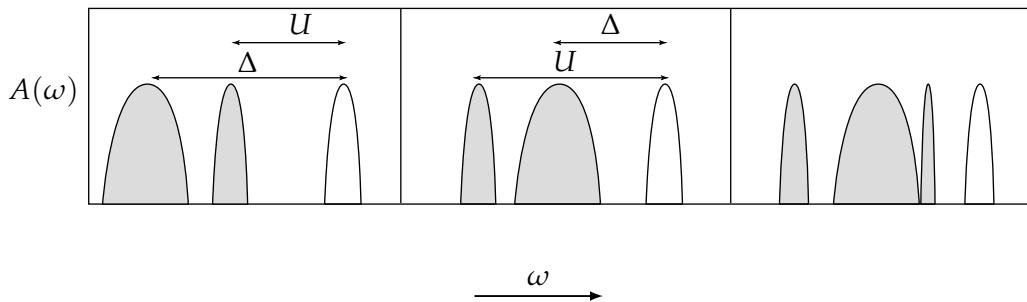


FIGURE 3.3.: MOTT (left panel) vs. charge-transfer insulator (middle panel). The right panel shows in addition the appearance of a sharp resonance within the charge-transfer gap due to the formation of a ZHANG-RICE-singlet which becomes gradually filled upon doping charge carriers into the CuO_2 plane. The image is highly schematic as in general one has to distinguish between bonding, anti-bonding and non-bonding combinations of the oxygen and copper orbitals (see, e. g., [66] for details).

3. EELS On Underdoped Cuprates

This suggests that the oxygen degrees of freedom may play an essential role for a proper understanding of the electronic structure and also calls for an extension of the single-band HUBBARD model taking into account the p_x - and p_y -orbitals seen in Fig. 3.4. The result of such a multiband approach is the EMERY model [76]

$$\begin{aligned}
 H = & \epsilon_p \sum_{i\sigma} n_{p\sigma}^i + \epsilon_d \sum_{i\sigma} n_{d\sigma}^i + t_{pd} \sum_{\langle ij \rangle \sigma} (d_{i\sigma}^\dagger p_{j\sigma} + \text{h.c.}) + t_{pp} \sum_{\langle ij \rangle \sigma} (p_{i\sigma}^\dagger p_{j\sigma} + \text{h.c.}) \\
 & + U_d \sum_{i\sigma\sigma'} n_{d\sigma}^i n_{d\sigma'}^i + U_p \sum_{i\sigma\sigma'} n_{p\sigma}^i n_{p\sigma'}^i + U_{pd} \sum_{\langle ij \rangle} n_d^i n_p^j
 \end{aligned} \tag{3.1}$$

with the on-site energies ϵ_p and ϵ_d , the COULOMB repulsions U_p , U_d and U_{pd} and the hopping integrals t_{pp} and t_{pd} where p and d label oxygen and copper sites, respectively. The operators create and annihilate holes in the corresponding orbitals and the notation $\langle ij \rangle$ implies summation over pairs of nearest neighbors. The realization of the charge-transfer insulator situation in the cuprates implies that the original HUBBARD term $U = U_d$ is the largest energy scale and therefore $\Delta \equiv |\epsilon_p - \epsilon_d| < U_d$.

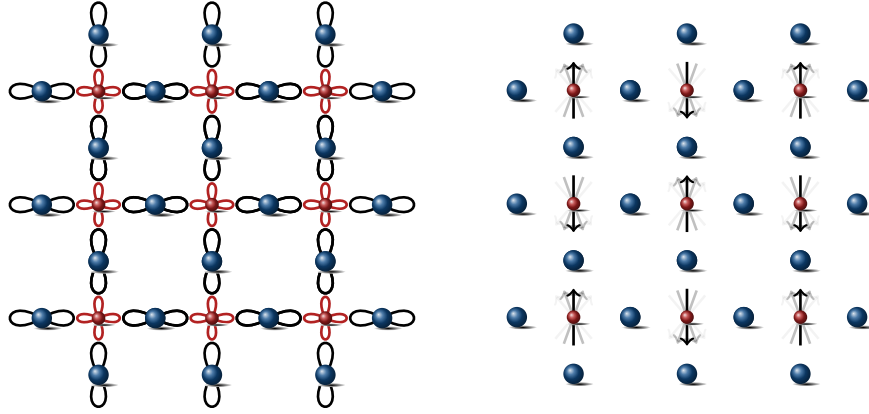


FIGURE 3.4.: The CuO_2 plane of the undoped cuprates. Small (large) circles correspond to Cu (O), respectively. The left panel shows the orbitals involved in the EMERY model (Eq. 3.1) whereas the right panel sketches the antiferromagnetic order on the copper sites. The distinction between the left and right image is, of course, artificial and employed here only for better visibility. In reality spins and orbitals are simultaneously present.

The model Eq. 3.1 is a formidable task to analyze and a simplification is highly desirable. ZHANG and RICE could show that this is indeed possible [77]. As discussed above, additional charges will occupy oxygen hole states and the strong overlap between oxygen and copper will lead to an interference with the holes that are present on the copper sites. Now, there are two possibilities. The two spins may align either parallel to form a triplet or—and this is the situation which is energetically favored and therefore realized—antiparallel to form a singlet which is then called a ZHANG-RICE-singlet. With

3.2. Electronic Properties Of The Cuprates

this it is possible to consider the physics of the cuprates in terms of an effective approach with the ZRS forming the lower and the unoccupied branch of the copper $3d$ spectrum the upper HUBBARD band thereby returning to the simpler description in terms of the single-band HUBBARD or the $t - J$ model. Naturally, the strong hybridization between copper and oxygen that can be anticipated from the orbital configuration shown in Fig. 3.4 is also present for the case of zero doping and therefore the ZHANG-RICE band is always present and the single hole within the unit cell will fluctuate between copper and oxygen leading to a dynamic occupation of the ZRS. If, however, additional charge carriers are introduced into the system the band derived from the ZRS will become gradually occupied. This in turn leads to a breakdown of the charge gap which is on the order of some eV in the undoped compounds and low-lying charge excitations become possible between occupied and unoccupied states within the ZR band. Nevertheless, this does not imply that doping leads immediately to a conventional conductor. Instead, metallic features like a zero-frequency DRUDE response set in only after a finite amount of charges has been introduced (see below).

An important issue related to the doping of holes into the CuO_2 plane shown in Fig. 3.4 is the resulting strong disturbance of the antiferromagnetic background which becomes gradually destroyed upon increasing hole doping (see, e. g., [78, 79]). But it is not only the antiferromagnetism that becomes affected by the charges. Effects occur also the other way around, in particular the spin configuration dresses the doped charges, the resulting quasiparticle being a so called spin-polaron. Again, these phenomena had been known already before the cuprates were discovered [80, 81] but they naturally revived the interest in the problem of a single hole in an antiferromagnet. The authors of Ref. 82 could show that there are indeed quasiparticle solutions, i. e., there are well defined peaks in the single-particle spectral function

$$A(\mathbf{k}, \omega) = \text{Im } G(\mathbf{k}, \omega)$$

where the coherent (quasiparticle) part of the propagator is given by

$$G(\mathbf{k}, \omega) = \frac{Z_{\mathbf{k}}}{\omega - \Sigma(\mathbf{k}, \omega)} \quad Z_{\mathbf{k}} = \left(1 - \frac{\partial}{\partial \omega} \Sigma(\mathbf{k}, \omega) \right)^{-1},$$

with the quasiparticle weight $Z_{\mathbf{k}}$ and the self-energy $\Sigma(\mathbf{k}, \omega)$ arising from a diagrammatic series for the hole propagator interacting with the propagator for the spin excitations created during the movement of the hole in the presence of the antiferromagnetic order. As in ordinary FERMI liquid theory the self-energy term gives rise to an effective mass according to

$$\frac{1}{m_{ij}} = \frac{\partial^2}{\partial k_i \partial k_j} \omega_{\mathbf{k}} = Z_{\mathbf{k}} \left. \frac{\partial^2}{\partial k_i \partial k_j} \Sigma(\mathbf{k}, \omega) \right|_{\omega=\omega_{\mathbf{k}}}$$

3. EELS On Underdoped Cuprates

where ω_k gives the energy of the quasiparticle pole. It can be shown that in the parameter range relevant for the cuprates

$$J = \frac{4t^2}{U} \ll t$$

$Z_k \sim J/t \ll 1$ [82]. In addition the bandwidth of this dressed spin-polaron is renormalized from the bare value t down to J . A graphical representation of these effects is shown in Fig. 3.5 from which it becomes obvious that the hopping of a single hole in an otherwise antiferromagnetic surrounding creates chains of frustrated spins (sometimes also called strings) that lead to an enhancement of the exchange energy scaling linearly with the length of the string. This produces a confining potential that binds the hole to the site where it was initially created. Experimentally this behavior was indeed observed in the ARPES spectra of the oxychloride $\text{Sr}_2\text{CuO}_2\text{Cl}_2$ [83] though also other explanations have been put forward for their understanding. In particular LAUGHLIN argued that the observed dispersion reflects the decay of the photo-hole indicating the presence of spin-charge separation [84].

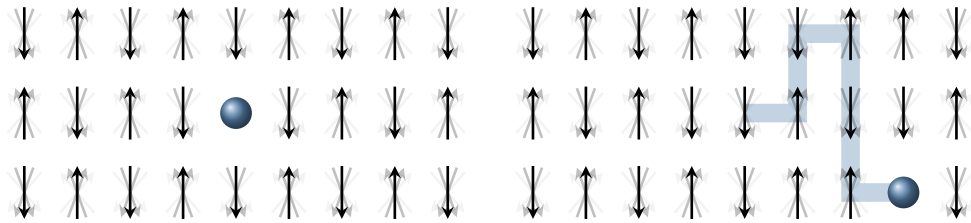


FIGURE 3.5.: The motion of a single hole in an antiferromagnet. It is clearly seen that a hole (solid circle) created at a particular site (left panel) leaves behind a chain of frustrated spins (right panel) along its path (thick solid line). This is accompanied by a large mass enhancement for the hole propagation.

If the doping is pushed further, things get even more involved and this is also the region where most of the arguments take place. Macroscopically, the behavior is probably best reflected in the generic phase diagram shown in Fig. 3.6.

As already mentioned above the antiferromagnetic order becomes quickly destroyed upon hole doping and what emerges is a phase that is often referred to as the pseudogap observed in a large variety of experimental probes [85–87]. There is a widespread belief within the community that charges in this so called underdoped (labeled as UD in Fig. 3.6) range of the phase diagram are agglomerated into regular patterns termed stripes or checkerboards [88–90] forming domain walls for the diminished but still present antiferromagnetism. A problem of particular relevance in this regard is whether these inhomogeneities promote or suppress superconductivity. There is evidence for either possibility. On the one hand it is known that in the lanthanum-based cuprates the superconducting T_c is strongly reduced [91] at the doping concentration of $x = 0.125$

3.2. Electronic Properties Of The Cuprates

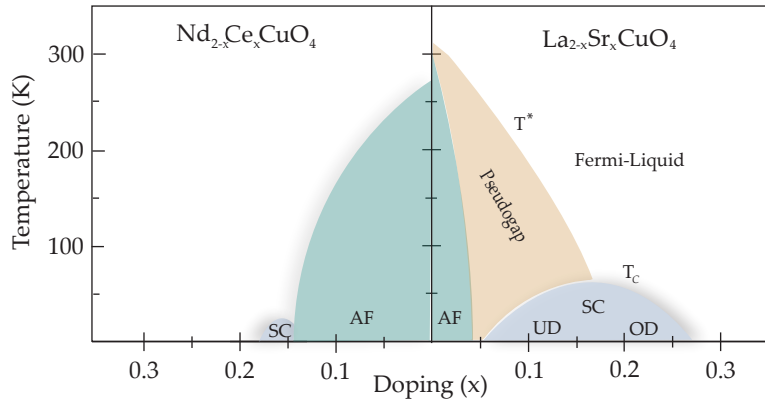


FIGURE 3.6.: The generic phase diagram of the cuprates. The hole-doped (right) side is of particular relevance in this work. There the antiferromagnetism (AF) which characterizes the parent compounds disappears quickly upon hole-doping and the most complicated phase, often called pseudogap phase sets in. At even higher doping concentrations the superconducting dome appears which contains the underdoped (UD), optimally doped (OP) and the overdoped (OD) regimes. For still higher carrier concentrations one finally recovers a phase which can be described in terms of a FERMI liquid picture.

where stripes are very robust [88]—an effect that has been termed “ $1/8$ -anomaly”. On the other hand theoretical models incorporating fluctuating stripes [92] are able to reproduce the 40 meV resonance mode that is observed in neutron scattering and argued—by many researchers (see, e. g., [56])—to be the boson required[†] to bind the COOPER pairs in the superconducting state.

Besides the spin degrees of freedom the charges are naturally of great interest. It is known from transport measurements [67] that upon doping there is a metal-insulator transition which is also consistent with the increase of spectral weight in the low-energy region and finally the appearance of a DRUDE-like response in the optical conductivity [93, 94], in accord with what has been discussed in relation to Fig. 3.2.

A typical hallmark of a metal is of course the FERMI surface and its development is another big open issue. It is known to exist in optimally and overdoped systems [22] for $T > T_c$ and Fig. 3.7 gives a schematic view of it. The peculiar $d_{x^2-y^2}$ -shape of the superconducting order parameter [95] leaves only a point along the $(0,0) \rightarrow (\pi,\pi)$ line ungapped below T_c and therefore the area of momentum space around this point is called the nodal region. In contrast to that on the underdoped side of the superconducting dome the FERMI surface becomes destroyed already at temperatures above T_c signaling the onset of the pseudogap. What remains are disconnected segments of the original FERMI surface the length of which shrink with decreasing temperature

[†]It is not even clear whether a coupling boson is at all necessary to bind the charges into pairs [38].

3. EELS On Underdoped Cuprates

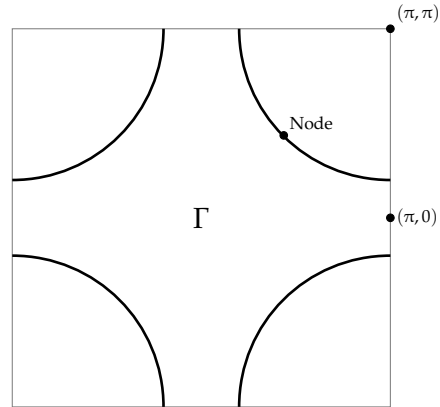


FIGURE 3.7.: A schematic view of the FERMI surface of cuprates in the optimally and overdoped regime of the phase diagram. The point labeled as ‘Node’ marks the position where the superconducting gap is zero.

[96] and doping [97]. This phenomenon was coined “arc” by NORMAN *et al.* [98]. If the temperature is then further lowered down to T_c the phase space for superconductivity is strongly reduced and the true superconducting gap opens only along the arc [97]. Therefore currently there is increasing experimental evidence for a so called dichotomy between electrons from the nodal and antinodal direction: below T_c not all the electrons enter the superconducting condensate because a substantial part is no longer available being tied already by the pseudogap. This leads some researchers to ask if “Two gaps make a high-temperature superconductor?” [99]. In remarkable disagreement with this, quantum oscillation experiments [100, 101] indicate the existence of small (closed) pockets instead of disconnected arcs and there are now arguments that, due to some peculiar feature of the photoemission matrix element, these pockets simply appear as arcs in the ARPES spectra. This is a completely open field which will probably not be settled in the near future due to a well-known problem persisting since the very beginning: not all samples can be measured with all spectroscopies leaving plenty of space for speculations.

To summarize this short and very incomplete overview of the present status on the cuprates-physics one may say that the endless efforts spent for a better understanding of the electronic properties of the cuprates already led to a wealth of information on all kinds of details but the very essential question, how the MOTT insulator *transforms* into an unconventional superconductor upon adding just a slight amount of charges, remains to a large extend unsolved. Of course, the disagreement on the precise pairing mechanism is not satisfying, but it is not so much the superconducting phase that is complicated to understand. Instead the underdoped regime with its plethora of

3.3. Charge-Transfer Excitons In Underdoped Oxychlorides

different ground states: antiferromagnetism, charge-ordered and superconducting phases where only small changes in one experimental parameter like doping, pressure etc. might be enough to disturb this fragile equilibrium thereby replacing one order by the other forms the biggest puzzle.

We are going to add some pieces to it in the following.

3.3. Charge-Transfer Excitons In Underdoped Oxychlorides

Now, we turn to the investigation of the doping dependence of the CT processes between copper and oxygen investigated for the special case of the $\text{Ca}_{2-x}\text{Na}_x\text{CuO}_2\text{Cl}_2$ system. It is known that single crystals of those compounds are very air-sensitive which provides a substantial obstacle for the preparation of films thin enough for EELS measurements as described in Sect.2.5.2. To avoid oxidation of the single crystals grown and provided by the group of H. TAKAGI [65] as far as possible the samples were cut by S. PYON with the help of the microtome under nitrogen atmosphere. Indeed, the films obtained in this way turned out to be well defined single crystals as can be seen from Fig.3.8 which exemplarily shows the lattice structure for $\text{Ca}_{1.9}\text{Na}_{0.1}\text{CuO}_2\text{Cl}_2$ as measured in the EELS spectrometer with the help of elastic scattering. The sharp BRAGG-peaks observed correspond to the reciprocal lattice vectors parallel to the copper-oxygen bonds (labeled (100), equivalent to $\Gamma \rightarrow (\pi, 0)$ in Fig.3.7) and diagonal to them (labeled (110), equivalent to $\Gamma \rightarrow (\pi, \pi)$ in Fig.3.7) and their fourfold symmetry (not shown) with respect to the angle within the CuO_2 plane (see Fig.2.2) proves that the square lattice indeed survived the elaborate sample preparation procedure, at least within the resolution of the spectrometer.

Naturally, the next step is to investigate the behavior of the loss function[‡] for different values of the charge carrier concentration. A first overview for $q = 0.1 \text{ \AA}^{-1}$ is provided by Fig.3.9 where we see numerous things that will be disentangled in the following. As the reference spectrum we take the data for $\text{Sr}_2\text{CuO}_2\text{Cl}_2$ as described in [102, 103]. There is zero intensity up to about 1.5 eV followed by a well pronounced double peak structure[§] that is also reported for optical spectra of $\text{Sr}_2\text{CuO}_2\text{Cl}_2$ [104, 105], the actual

[‡]According to Eq.2.3 the intensity measured and also displayed is only proportional to the loss function. Nevertheless, we will often ignore this and simply take this proportionality as an equality. In any case, the axis label always provides the correct description.

[§]It should be noted that when the $\text{Sr}_2\text{CuO}_2\text{Cl}_2$ data were measured, the beam performance shown in Fig.2.9 was not yet available. Therefore, in principle it would be interesting to repeat these measurements with higher resolution. As no single crystals with $x = 0$ were available in the course of this work the data shown in Fig.3.9 are nevertheless taken for comparison.

3. EELS On Underdoped Cuprates

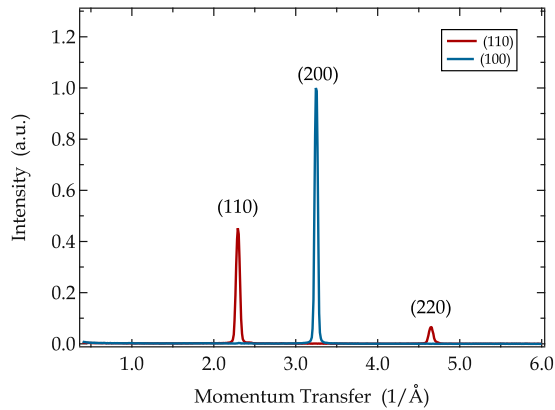


FIGURE 3.8.: The BRAGG spectra for $\text{Ca}_{1.9}\text{Na}_{0.1}\text{CuO}_2\text{Cl}_2$ in the high-symmetry directions shown in Fig. 3.7. The values in parentheses give the corresponding MILLER indices and their positions are in fair agreement with the structural data described in Ref. 65.

parent compound $\text{Ca}_2\text{CuO}_2\text{Cl}_2$ (see Fig. 3.13) and also other cuprate parent compounds [106]. In contrast to that for the $\text{Ca}_{1.95}\text{Na}_{0.05}\text{CuO}_2\text{Cl}_2$ spectra there is intensity in the tail of the elastic line (which has not been subtracted for this very purpose) and the two features seen in the insulating case merge into a single sharp structure situated roughly halfway between the two humps seen in the $\text{Sr}_2\text{CuO}_2\text{Cl}_2$ case. For still higher doping values (the $\text{Ca}_{1.9}\text{Na}_{0.1}\text{CuO}_2\text{Cl}_2$ spectra) the single sharp feature between 2 eV and 2.5 eV is further softened and even more intriguingly—and in sharp contrast to the case of zero and five percent doping—the spectra for the two shown lattice directions become *different*. For momentum transfer parallel to the copper oxygen bonds (left panel in Fig. 3.9) the single peak already visible in the $\text{Ca}_{1.95}\text{Na}_{0.05}\text{CuO}_2\text{Cl}_2$ spectra acquires significant spectral weight in the shown energy range whereas it loses substantial strength for the (110) direction (right panel in Fig. 3.9) in favor of an intensity enhancement around 1 eV. According to the tetragonal lattice structure one would expect symmetric spectra within the CuO_2 plane, i. e., spectra for a constant doping concentration should be independent of the angle within the CuO_2 plane, which is obviously not the case for $\text{Ca}_{1.9}\text{Na}_{0.1}\text{CuO}_2\text{Cl}_2$. This points to some kind of symmetry breaking which is discussed in more detail in Sect. 3.4. Before that we will focus on the behavior in the 2.0 – 2.5 eV range.

3.3.1. Origin Of The Observed Features

To begin the discussion, one should probably comment on why Fig. 3.9 compares spectra of a particular insulator ($\text{Sr}_2\text{CuO}_2\text{Cl}_2$) with the doped counterparts of another one ($\text{Ca}_{2-x}\text{Na}_x\text{CuO}_2\text{Cl}_2$). The main reason for this are the difficulties in the growth of

3.3. Charge-Transfer Excitons In Underdoped Oxychlorides

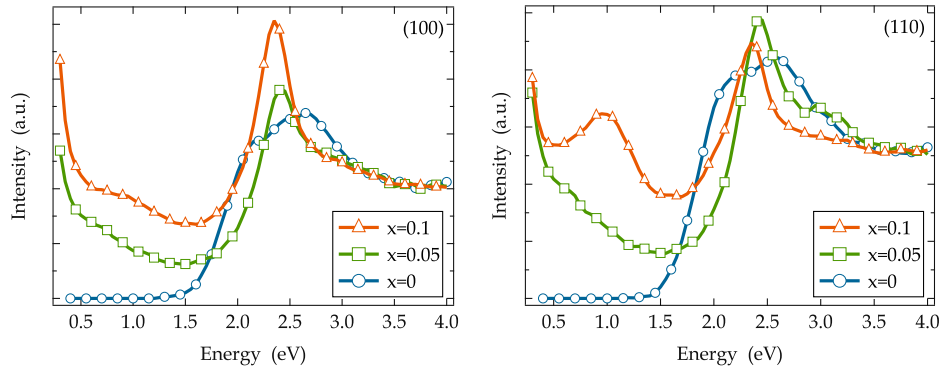


FIGURE 3.9.: The doping evolution for the EELS intensity in the low energy region for $\text{Sr}_2\text{CuO}_2\text{Cl}_2$ (blue circles) and $\text{Ca}_{2-x}\text{Na}_x\text{CuO}_2\text{Cl}_2$ for momentum transfers parallel to $\Gamma \rightarrow (\pi, 0)$ (left panel) and $\Gamma \rightarrow (\pi, \pi)$ (right panel) for $q = 0.1 \text{ \AA}^{-1}$. For comparison, the spectra are normalized on the high-energy side between 3.5 eV and 4 eV. The $\text{Sr}_2\text{CuO}_2\text{Cl}_2$ data are reproduced from [102, 103].

$\text{Ca}_2\text{CuO}_2\text{Cl}_2$ single crystals which were not available for the present study. Nevertheless, as Ca and Sr have the same valency they can be considered iso-electronic. They do, of course, differ in size but as both ions are well separated from the CuO_2 plane (see Fig. 3.1) which is the main structural unit as discussed above this effect will be neglected in the following.

As can be seen from Fig. 3.9 the undoped compounds show a well pronounced gap. This is in agreement with what has been said in Sect. 3.2 reflecting the insulating behavior. To understand what microscopic mechanisms drive the finite intensity above the gap edge it is important to realize that EELS creates by definition particle-hole pairs. Together with the fact that the lowest possible electronic transitions within the CuO_2 plane correspond to charge-transfer excitations between oxygen and copper (see Fig. 3.3) the resulting object can be visualized as shown in Fig. 3.10.

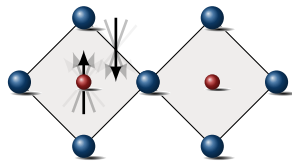


FIGURE 3.10.: The image shows two plaquettes from the CuO_2 plane in Fig. 3.4 with one electron transferred from oxygen to copper producing a particle-hole pair consisting of a ZHANG-RICE-singlet on the left and a copper $3d^{10}$ -site on the right plaquette.

Obviously, an electron is transferred from an oxygen atom of one plaquette (one CuO_4 -unit within the CuO_2 plane) to another one. What remains on the “donor-site”

3. EELS On Underdoped Cuprates

are two holes (the original one from the copper $3d^9$ -configuration and the one created by the charge-transfer) forming a ZHANG-RICE-singlet and the transferred electron fills up the d -shell of the copper on the “acceptor-site” to form a $3d^{10}$ -configuration. We will call such an object a charge-transfer-exciton in the following.

Although this seems straightforward given that the cuprates are generally accepted to be charge-transfer-insulators there have been considerable arguments in the literature [107–109] about the precise nature of these entities, mostly motivated by the presence of two features in close proximity to each other as indicated by the optical spectra on several cuprate families as discussed above. This suggests that the charge-transfer is actually more involved than what is shown in Fig. 3.10. In particular, the authors of Ref. 109 analyzed possible excitonic modes based on a group-theoretical analysis of possible transitions within the manifold of copper and oxygen states. The low energy feature seen in the $\text{Sr}_2\text{CuO}_2\text{Cl}_2$ spectra was attributed to a so called one-center exciton (OCE) and the higher one to a two-center exciton (TCE). While the latter one corresponds to the object shown in Fig. 3.10 and involves the p_σ -orbitals of oxygen shown in Fig. 3.4 the former describes a quasiparticle that is localized on a single plaquette—hence the name OCE—and involves p_π -states whose lobes are oriented perpendicular to the $d_{x^2-y^2}$ -orbital of the central copper ion. Although the OCE scenario is potentially of great interest because it would indicate the necessity of multiband approaches to describe the low-energy physics of the CuO_2 plane—even beyond the EMERY model that has been discussed in Sect. 3.2—we will argue below that there is no need and also no true experimental evidence for this approach.

To this end it is instructive to realize that besides the CuO_2 plane shown in Fig. 3.4 there exist other cuprate systems with different geometries that provide further insight into the physics of the more general class of copper-oxygen networks. In the following we will concentrate on Sr_2CuO_3 which forms a so called corner-sharing chain of Cu and O (see Fig. 3.11). It can be considered as a 1D cut through the CuO_2 plane and is therefore believed on the one hand to be equivalent to the “true” cuprates for polarizations parallel and on the other hand to reflect the physics of an isolated plaquette for polarizations perpendicular to the chain direction. This is of importance for the discussion whether or not OCE and TCE excitations are indeed realized because the TCE is extended over two plaquettes (and can therefore be observed in the Sr_2CuO_3 case only along the chain direction) whereas the OCE is confined to a single plaquette and should therefore be observable parallel *and* perpendicular to the chain. Indeed, the optical spectra of Sr_2CuO_3 [110, 111] observe two features in the 2 eV range for light polarizations parallel to the chain. There is however no feature in the absorption perpendicular to the chain direction but parallel to the plaquettes. This argues strongly

3.3. Charge-Transfer Excitons In Underdoped Oxychlorides

against the possibility of an OCE mode. We therefore abandon the notion of the OCE in the following.

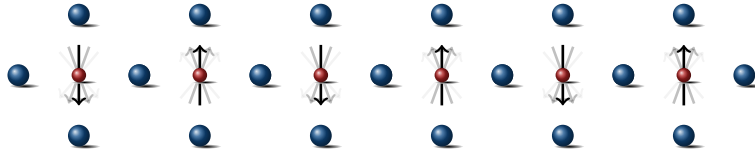


FIGURE 3.11.: A one-dimensional chain of corner-sharing copper (small circles) and oxygen (large circles) atoms realized in the compound Sr_2CuO_3 which can be understood as an analog of the CuO_2 plane along the chain axis but reflecting the physics of an isolated plaquette perpendicular to it.

So, what is the origin of the two-peak structure for the $\text{Sr}_2\text{CuO}_2\text{Cl}_2$ data? Again, optical experiments on Sr_2CuO_3 [112] prove rather helpful in this respect. For comparison and in order to facilitate the discussion Fig. 3.12 compares the behavior of the optical conductivity as reported for Sr_2CuO_3 in Ref. 112 with the one calculated via a KRAMERS-KRONIG transformation from the EELS data. Though they differ in their absolute values which possibly points to different sample qualities (impurity concentrations etc.) they both share a common behavior in the energy range of interest. There is a sharp peak slightly below 2 eV with a small additional hump on the high energy tail (around 2.5 eV) which translates to the double-peak structure in the loss function also for Sr_2CuO_3 [112]. Note that this behavior is also reported in the DMFT literature (see [113]).

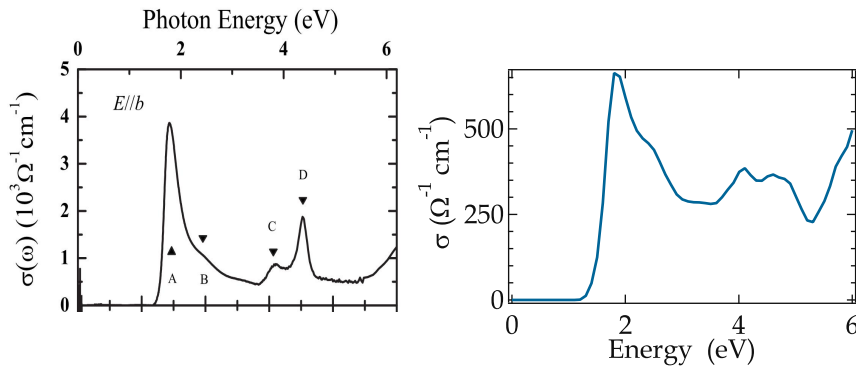


FIGURE 3.12.: The optical conductivity for Sr_2CuO_3 (left panel, reproduced from [112]) and $\text{Sr}_2\text{CuO}_2\text{Cl}_2$ (right panel) as derived by a KRAMERS-KRONIG transformation of the EELS intensity shown in Fig. 3.9. In both cases there is a sharp feature below 2 eV (labeled A in the left panel) followed by a small shoulder (labeled B).

Therefore, in agreement with Ref. 112, we identify the sharp feature in the conductivity (corresponding to the lower of the two features in the loss function) as the transition

3. EELS On Underdoped Cuprates

to the TCE shown in Fig. 3.10 and the hump on the high energy side to a resonance of this excitonic mode that can be understood as an unbound electron-hole pair, similar to the scattering states in a hydrogen atom. This scenario will turn out to provide a consistent description of all experimental phenomena as discussed in the remainder of this section.

As the authors of Ref. 112 correctly point out, the presence of a sharp peak in the conductivity spectra indicate the presence of a sizable intersite COULOMB-attraction which leads to the formation of the excitonic mode. Were it absent, the EELS spectra for $\text{Sr}_2\text{CuO}_2\text{Cl}_2$ would consist only of a single peak, caused by the resonance. This is similar to what is known for conventional semiconductors where the inclusion of electron-hole attraction between the valence and conduction band leads to a strong modification in the absorption spectrum and most importantly to the presence of sharp excitonic peaks that acquire substantial spectral weight in the energy region of the gap edge [114]. Nevertheless, the “exciton physics” in a strongly correlated system is much more involved than in conventional semiconductors, in particular due to the strong interference between the charge- and the spin-channel, exemplified already in Fig. 3.5 and further discussed below.

The theoretical foundation for the formation of a true excitonic mode is given by the extended single band HUBBARD model where in addition to the onsite repulsion U there is a nearest neighbor COULOMB term characterized by the parameter V that is known to produce a bound, i. e., excitonic state for $V > 2t$ in the one-dimensional and for higher values in the two-dimensional case [115–118]. On qualitative grounds one can understand this in a straightforward manner at least for the 1D case: the excitation energy for a particle-hole pair on nearest neighbor sites is given by $\Delta E = U - V$, instead of U were they created further apart from each other. If the hopping parameter t is not too large compared to the COULOMB attraction parametrized by V , the resulting object will have no reason to dilute into its constituents in order to gain kinetic energy. Remarkably, these bound states have been experimentally verified also in other transition-metal compounds like Ni halogenides [116] which points to their general importance for correlated electron systems.

Concerning the doping induced changes observed in Fig. 3.9 they are also readily explained within the above given framework. Naturally the introduction of additional charge carriers in the system will influence the exciton formation. This is due to the screening which will lower the binding energy of the exciton, for high enough dopant concentrations eventually even below the critical value to produce the bound state. Note, however that according to Fig. 3.13 at least for the $\text{Ca}_{1.95}\text{Na}_{0.05}\text{CuO}_2\text{Cl}_2$ sample the carrier density is not yet high enough to establish metallic behavior and therefore the screening may be too weak to reduce the probability for the creation of an

3.3. Charge-Transfer Excitons In Underdoped Oxychlorides

exciton to zero. Nevertheless, as a result of it the exciton will be strongly quenched and it will acquire less and less spectral weight thereby enhancing the resonance. Unfortunately the increasing intensity in the energy range up to 1 eV causes a lot of ambiguities when trying to subtract the elastic line which was therefore not removed in Fig. 3.9. Consequently it is also not possible to perform a reliable KRAMERS-KRONIG transformation for the $\text{Ca}_{2-x}\text{Na}_x\text{CuO}_2\text{Cl}_2$ spectra and the spectral weight redistribution between the exciton and the resonance cannot be truly quantified.

Lying in close proximity to each other the intensity-loss of the bound state will also shift the resonance mode to lower energies due to the non-linear superposition of two adjacent features in the loss function. This is all in line with what is observed in Fig. 3.9 where upon doping the double structure quickly disappears leaving a single feature behind that becomes increasingly softened upon doping. Further experimental evidence for this interpretation comes from doping dependent spectra where it is always the low energy part of the 2 eV structure that becomes more affected by additional charges, pointing to the excitonic origin of the excitation on the low energy side. This can be observed in $\text{La}_{2-x}\text{Sr}_x\text{CuO}_4$ [93], in the yttrium family [119], the optical conductivity of the $\text{Ca}_{2-x}\text{Na}_x\text{CuO}_2\text{Cl}_2$ system shown in Fig. 3.13 and even theoretical DMFT results [113] support this reasoning. In contrast to the observations in EELS, however, the experimental optical conductivity does not show an energetic shift upon doping. This is because—as pointed out already in Sect. 2.4.3— $\sigma(\omega) \propto \omega\epsilon_2(\omega)$ reflects a linear superposition of several excitations, i. e., changing the parameters of one oscillator will leave another one *unaffected*, as can be easily verified within the DRUDE-LORENTZ-model (Sect. 2.4.3).

3.3.2. Dispersion Of The CT-Exciton

Now we turn to the momentum dependence of the charge-transfer-exciton. To set the stage Fig. 3.14 summarizes what has been obtained for the parent compound and the corresponding spectra for the $\text{Ca}_{2-x}\text{Na}_x\text{CuO}_2\text{Cl}_2$ system are shown in Fig. 3.15. Again, the present section will lay the focus only on the features around 2 eV and the low-energy peculiarities are postponed until Sect. 3.4.

Already this superficial comparison reveals remarkable differences for the momentum dependence. The parent compound obviously shows a sizable dispersion (see also Fig. 3.16). This is in line with other reports from EELS [121] and with what has been observed—though with worse resolution—in x-ray scattering experiments on $\text{Ca}_2\text{CuO}_2\text{Cl}_2$ [122, 123]. In remarkable contrast to that, for the $\text{Ca}_{2-x}\text{Na}_x\text{CuO}_2\text{Cl}_2$ system the feature of interest is strongly localized and rapidly loses strength upon leaving the center of the BRILLOUIN zone. This behavior is obviously rather independent

3. EELS On Underdoped Cuprates

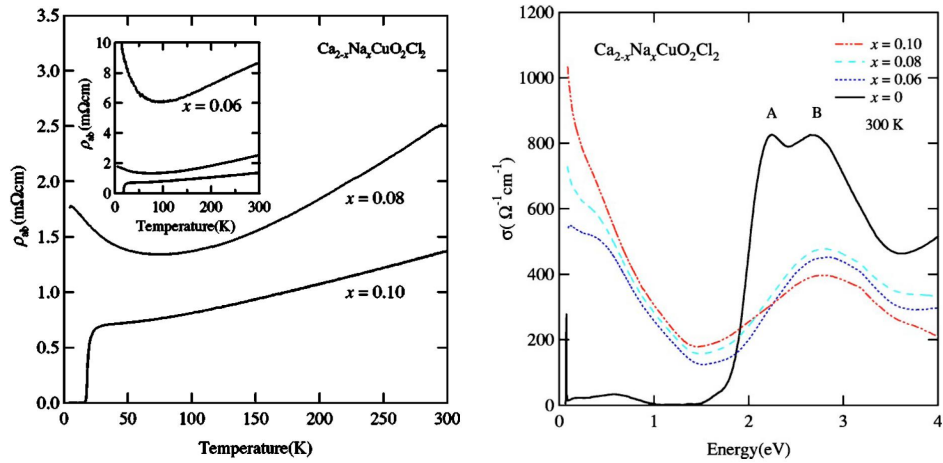


FIGURE 3.13.: The resistivity (left panel) and the optical conductivity (right panel) for the $\text{Ca}_{2-x}\text{Na}_x\text{CuO}_2\text{Cl}_2$ samples. Both panels show the typical behavior of the cuprates. There is insulating behavior for zero and small doping concentrations followed by a metal-insulator transition at larger values of x . Images taken from Ref. 120.

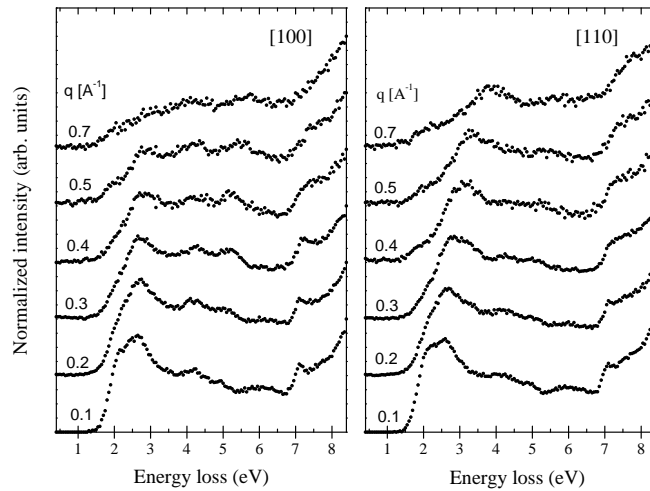


FIGURE 3.14.: The dispersion of the charge-transfer exciton in $\text{Sr}_2\text{CuO}_2\text{Cl}_2$ according to Ref. 102, 103. One can observe a sizable dispersion of the structure in both lattice directions.

of the exact doping concentration. To give a more quantitative impression of the different behavior for (non)zero doping Fig. 3.16 compares the dispersion of the main $\text{Sr}_2\text{CuO}_2\text{Cl}_2$ feature (around 2.5 eV in Fig. 3.9) with the peak seen in the doped samples

3.3. Charge-Transfer Excitons In Underdoped Oxychlorides

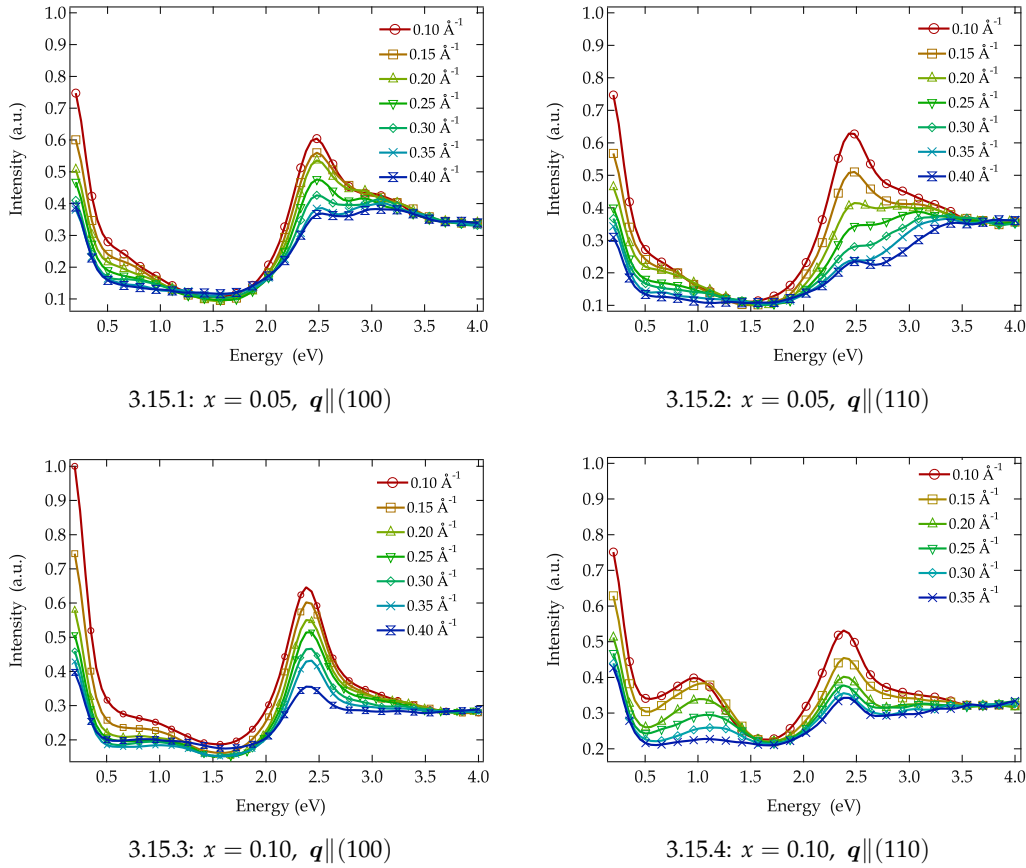


FIGURE 3.15.: The EELS intensity in $\text{Ca}_{2-x}\text{Na}_x\text{CuO}_2\text{Cl}_2$ for doping concentrations and lattice directions indicated in the subfigure captions. All spectra have been normalized on the high-energy side between 3.5 eV and 4 eV.

($\text{Ca}_{1.95}\text{Na}_{0.05}\text{CuO}_2\text{Cl}_2$ is taken as the example). The energy positions are taken to be the local maxima of the EELS intensity in the given energy range around 2 eV. Again, it is clearly visible that the insulator disperses significantly, in stark contrast to the data for $x > 0$.

As discussed in Sect. 3.2 the undoped cuprates show well pronounced antiferromagnetism. ZHANG and NG developed a theoretical understanding for the exciton dynamics in this particular case [108]. They elaborated that the geometry of the CuO_2 plane leads to four excitonic modes of different symmetry. Due to symmetry reasons only one of them is dipole active, i. e., can be excited in the limit $\mathbf{q} \rightarrow 0$ and it corresponds, in extension to the schematic view presented in Fig. 3.10 to a fourfold symmetric combination of oxygen contributions forming the additional hole around the central

3. EELS On Underdoped Cuprates

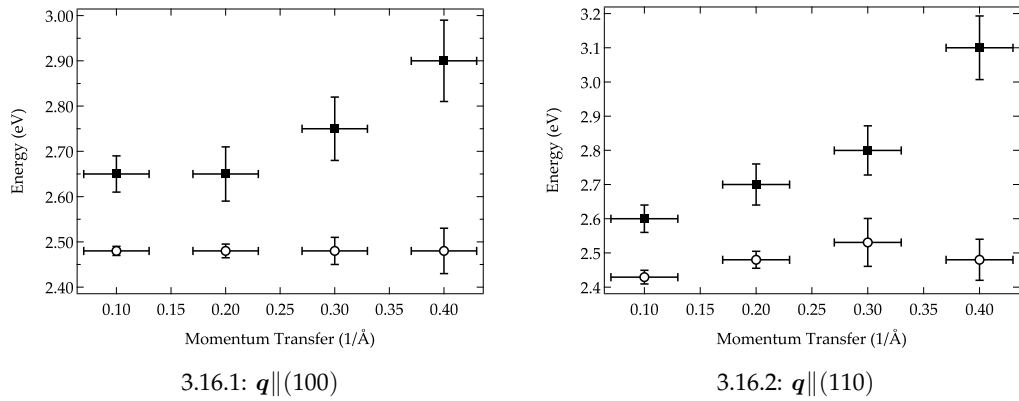


FIGURE 3.16.: The dispersion of the charge-transfer exciton as a function of momentum transfer for $\text{Ca}_{1.95}\text{Na}_{0.05}\text{CuO}_2\text{Cl}_2$ (open circles) and $\text{Sr}_2\text{CuO}_2\text{Cl}_2$ (solid squares).

copper site. Upon increasing momentum the different modes are allowed to propagate due to t_{pp} and t_{pd} discussed already in connection with Eq. 3.1. Now, the important thing to realize is that the binding of the two spinless objects forming the exciton shown in Fig. 3.10 leads to their ability to move through the lattice *without* disturbing the antiferromagnetic surrounding.^{||} This is in contrast to the processes discussed in relation with Fig. 3.5 where the frustration of the antiferromagnetic order led to a strong confinement of the single-particle excitations. We therefore conclude that the dispersion of the $\text{Sr}_2\text{CuO}_2\text{Cl}_2$ features is driven by the exciton which is essentially free with respect to the antiferromagnetism. It shifts to higher energies with increasing momenta (in agreement with the theoretical prediction of Ref. 108) thereby merging into the resonance. The remaining single feature that is observed for $q \geq 0.3 - 0.4 \text{\AA}^{-1}$ in Fig. 3.14 disperses further up. But this is always driven by the exciton which is however not resolved anymore at higher momenta. Therefore Fig. 3.16 tracks only the behavior of the (at $q = 0.1 \text{\AA}^{-1}$) second feature.

The fact that the $\text{Ca}_{2-x}\text{Na}_x\text{CuO}_2\text{Cl}_2$ spectra consist only of a single structure reveals that the exciton is strongly quenched which provides also the clue why the dispersion breaks down. The continuum state that survives the doping corresponds to an essentially unbound particle-hole pair. Though the antiferromagnetism is suppressed upon doping there remain fluctuations of the magnetic order at least on a local scale. Therefore with the particle and the hole created during the EELS process we have twice the situation shown in Fig. 3.5 with the same result: The magnetic order leads

^{||}There are hopping paths possible which would eventually disturb the spin order but they are only higher order corrections in a perturbative treatment and therefore negligible.

to a confinement observable as the absence of a dispersion in Fig. 3.15 and Fig. 3.16. Another contribution to this may come from the fact that the doped charges occupy randomly distributed ZHANG-RICE-singlets which act as scattering centers confining the wavefunctions of the particle and the hole forming the resonance to a small area within the CuO_2 plane. This corresponds to the famous disorder induced ANDERSON localization [124] and may be the dominant contribution for $x = 0.1$ as on the one hand the concentration of the ZHANG-RICE-singlets is already rather high and on the other hand the antiferromagnetism no longer effective enough in localizing the particle-hole pair.

3.4. Evolution Of The Charge Carrier Plasmon

Now we turn our attention to the increasing intensity around 1 eV in general and to the apparent asymmetry in the dielectric response for the two lattice directions in $\text{Ca}_{1.9}\text{Na}_{0.1}\text{CuO}_2\text{Cl}_2$ system (see Fig. 3.9 and Fig. 3.15) in particular.

Before discussing this intriguing behavior in more detail we shall establish the microscopic origin of the intensity increase for $E \leq 1$ eV. It has been discussed above that the doping leads to a strong increase of low-energy spectral weight and the optical conductivity presented in Fig. 3.13 is in accord with this. In recent years it has become clear, however, that the charge response in the underdoped regime is not just created by the emergence of a coherent DRUDE term. Instead, there is ample experimental evidence for at least two excitation channels in the infrared (IR) range of the spectrum [120, 125]. There is a coherent DRUDE term accompanied by a mid-IR structure of, to a large extent, still mysterious origin. This feature shows, among other things, a scattering rate that is nearly temperature independent which is in contrast to the DRUDE term narrowing considerably for lower temperatures. Both features should and also will in principle contribute to the intensity enhancement in the tail of the elastic line seen in Fig. 3.9 and Fig. 3.15. Nevertheless, we will neglect this two-component behavior and identify in particular the peak in the (110) direction of $\text{Ca}_{1.9}\text{Na}_{0.1}\text{CuO}_2\text{Cl}_2$ around 1 eV as the charge carrier plasmon, driven by the free charge carriers responsible for the DRUDE characteristic in the optical conductivity [93, 120, 125]. This is motivated by several experimental observations.

According to the resistivity data (see Fig. 3.13) $\text{Ca}_{1.9}\text{Na}_{0.1}\text{CuO}_2\text{Cl}_2$ shows metallic behavior which is also in line with the appearance of a rather well defined plasma edge in the reflectivity spectra leading to the optical conductivities of Fig. 3.13 [120]. In addition, also other cuprates in particular from the yttrium and bismuth families [126–130] and even electron-doped systems [131] are known to exhibit analogous behavior in their optical spectra and the peak around 1 eV has therefore also been attributed to the

3. EELS On Underdoped Cuprates

DRUDE plasmon in those cases. In addition the 1 eV-peak seems to be strong enough to produce a zero crossing in $\epsilon_1(\omega)$ (the defining condition of a plasmon), though this cannot be proved rigorously due to the ambiguities arising from the subtraction of the elastic line and the resulting impossibility of a reliable KRAMERS-KRONIG transformation. Moreover the peak shape for $q = 0.1 \text{ \AA}^{-1}$ does not reflect simple DRUDE-like behavior in the loss function. Nevertheless, the facts discussed above strongly argue in favor of the plasmon scenario for the 1 eV-feature in Fig. 3.15.4.

From Eq. 2.15 it is clear that an “ordinary” metallic plasmon should exhibit a quadratic dispersion. But this, as can be seen from Fig. 3.17, is obviously not the case.

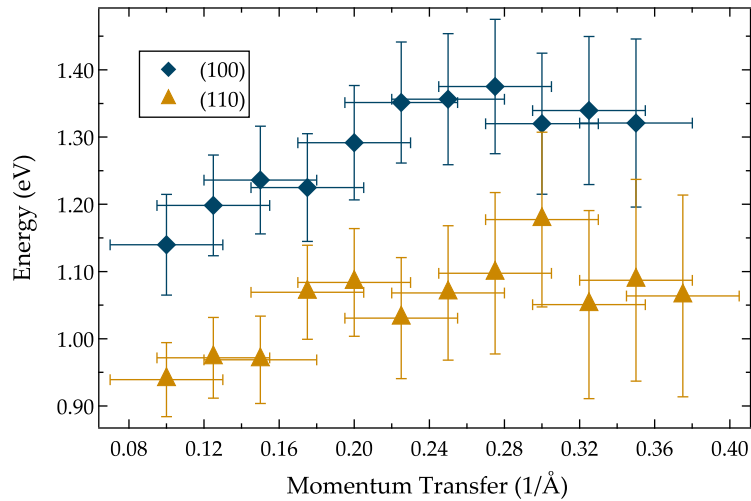


FIGURE 3.17.: Plasmon dispersion in $\text{Ca}_{1.9}\text{Na}_{0.1}\text{CuO}_2\text{Cl}_2$ along the two high-symmetry directions. Within the error bars the plasmon scales linearly with momentum and the bandwidth amounts to $\approx 200 \text{ meV}$ in the considered momentum range.

To avoid any ambiguities arising from the subtraction of the zero-loss peak the following procedure has been adopted to extract the curves shown in Fig. 3.17. For the (110) spectra the points in Fig. 3.17 simply track the peak position of the curves in Fig. 3.15.4. For the (100) direction the plasmon is strongly suppressed and in order to get any information about the plasmon position the points in Fig. 3.17 were obtained by extracting the zero crossing (between 1 eV and 1.5 eV) of the second derivatives from the data in Fig. 3.15.3. This explains the different onset energies for the two directions which should therefore be considered as an artifact of the data evaluation.[¶] The plasmon scales almost linearly with momentum and definitely not quadratically, at least for small momentum transfers. This is in contrast to the older reports for other cuprates mentioned above where in all cases the plasmon was found to show a

[¶]If the same procedure is applied to the (110) direction the onsets coincide within the error bars.

3.4. Evolution Of The Charge Carrier Plasmon

conventional RPA like q^2 behavior. As an example Fig. 3.18 reproduces the behavior for (optimally doped) $\text{Bi}_2\text{Sr}_2\text{CaCu}_2\text{O}_{8+\delta}$ reported in [128] and indeed in both high-symmetry directions the plasmon scales quadratically (note the quadratic scale on the momentum axis in Fig. 3.18!). Another striking feature is the strong reduction of the plasmon bandwidth. It amounts to more than 400 meV in $\text{Bi}_2\text{Sr}_2\text{CaCu}_2\text{O}_{8+\delta}$ and is lowered to roughly 200 meV for $\text{Ca}_{1.9}\text{Na}_{0.1}\text{CuO}_2\text{Cl}_2$. In the spirit of an RPA reasoning this suggests a smaller FERMI velocity for the underdoped $\text{Ca}_{1.9}\text{Na}_{0.1}\text{CuO}_2\text{Cl}_2$ compared to the optimally doped $\text{Bi}_2\text{Sr}_2\text{CaCu}_2\text{O}_{8+\delta}$ or, equivalently, a higher effective mass of the charge carriers. This may be understood realizing that the underdoped cuprates host a myriad of possible excitations that can couple to the charge carriers. To give just one specific example it was shown that there is a strong tendency of the additional holes to form polarons [132] which may lead to a dressing of the charges in close analogy to what has been said in Sect. 3.2 in relation to the string-formation.

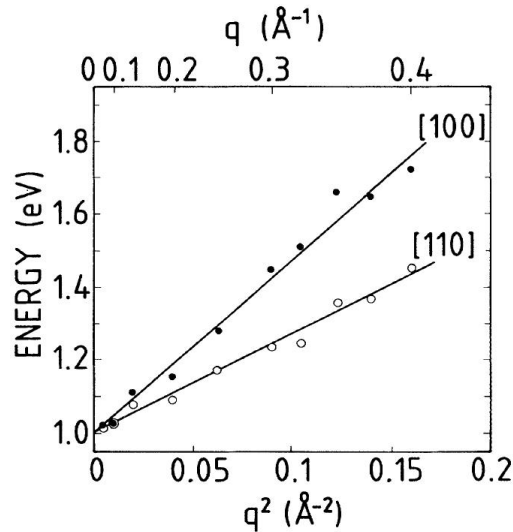


FIGURE 3.18.: The dispersion of the charge carrier plasmon for $\text{Bi}_2\text{Sr}_2\text{CaCu}_2\text{O}_{8+\delta}$ [128]. In both shown lattice directions the plasmon scales quadratically (note the quadratic scale on the abscissa), reminiscent of an “ordinary” metal. This is also consistent with the large FERMI surface extracted from this data [133].

In order to quantify the anisotropy in $\text{Ca}_{1.9}\text{Na}_{0.1}\text{CuO}_2\text{Cl}_2$ further, measurements have been performed over a wide range of temperatures and angles within the CuO_2 plane. The two maps shown in Fig. 3.19 summarize these results.

As can be seen there is a substantial angular range with an intensity enhancement around 1 eV at the expense of the charge-transfer-peak. This angular range is, though not perfectly symmetric, clearly located around the nodal region defined in Fig. 3.7 indicated by the dashed lines marking the different high-symmetry directions derived

3. EELS On Underdoped Cuprates

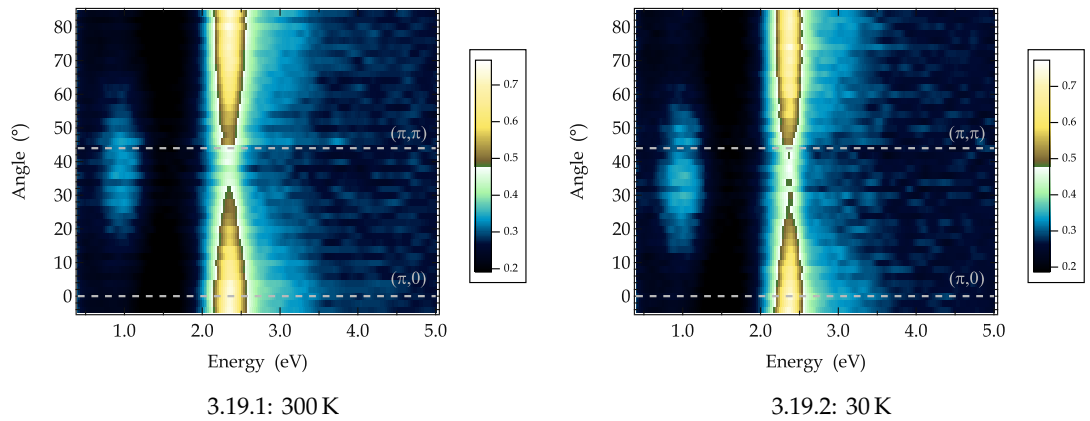


FIGURE 3.19.: The EELS intensity in $\text{Ca}_{1.9}\text{Na}_{0.1}\text{CuO}_2\text{Cl}_2$ displayed as a function of the angle with respect to the $(\pi, 0)$ direction as indicated in Fig. 3.7 for $q = 0.1 \text{ \AA}^{-1}$. There is an apparent increase of the signal around 1 eV in the vicinity of the nodal direction. The maps have been normalized on the high-energy side between 4 eV and 5 eV.

from the lattice structure shown in Fig. 3.8. From the comparison of the low- and high-temperature maps it is not directly clear whether or not the length of this “reef in front of the lagoon” changes its length with temperature. To this end Fig. 3.20 presents angular cuts at a constant energy-loss of 1 eV. For a more quantitative estimate the data points have been fitted to a single GAUSSIAN and the results of this fitting clearly argue against a temperature dependent shrinking or expansion of the 1 eV-peak but support the mismatch concerning the centering around the nodal direction. This asymmetry is rather puzzling, as the uncertainty of the spectrometer is normally less than the roughly ten degree mismatch between the peak maximum seen in Fig. 3.20 and the high-symmetry direction (π, π) .

Another instructive presentation of these phenomena is given by Fig. 3.21. It was produced by measuring constant energy cuts at three different energy-losses: $\Delta E = 1 \text{ eV}$ (the energy of the plasmon), $\Delta E = 2.4 \text{ eV}$ (the energy of the charge-transfer-peak) and $\Delta E = 4 \text{ eV}$. Then the first two cuts were divided by the third one which, as can be seen from the maps in Fig. 3.19, can be considered momentum independent. Obviously, there is a fourfold symmetry in the intensity swapping between the charge-transfer-peak and the plasmon. From this we can conclude that it reflects an intrinsic feature that is not caused by inhomogeneities resulting from the cutting of the crystals along a particular direction in the microtome. If this were the case, the symmetry would only be twofold as the knife would produce two distinguished axes: one parallel to the cutting direction and the other one perpendicular to it. In accord with Fig. 3.20 the symmetry breaking

3.4. Evolution Of The Charge Carrier Plasmon

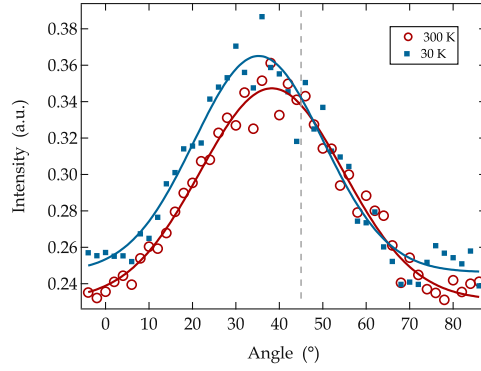


FIGURE 3.20.: A constant energy ($E = 1$ eV) cut through the maps from Fig. 3.19. The solid lines correspond to GAUSSIAN fits (central position: 35° (30 K), 38° (300 K); angular widths: 21° (30 K), 23° (300 K)). The dashed line indicates again the position of the node according to the BRAGG spectra (see Fig. 3.8).

turns out to be robust against temperature variations as there are no obvious changes, neither in the periodicity nor the amplitude of the effect between the lowest and highest achievable temperatures. This holds also for intermediate temperatures values (not shown). Finally, Fig. 3.22 shows the behavior of the normalized partial spectral weight

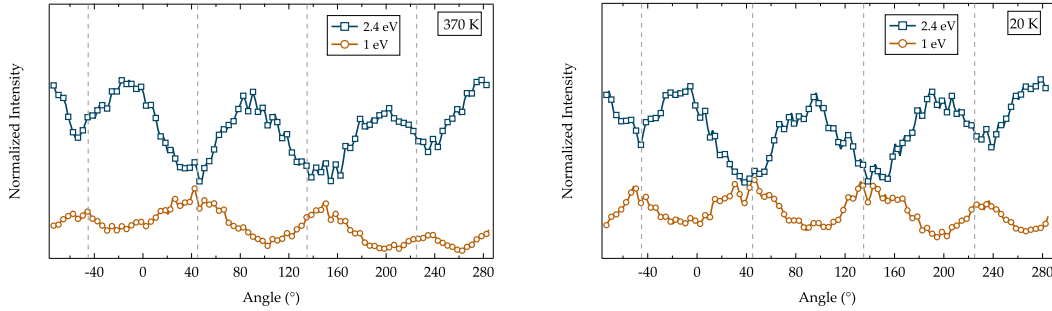


FIGURE 3.21.: The EELS intensity in $\text{Ca}_{1.9}\text{Na}_{0.1}\text{CuO}_2\text{Cl}_2$ displayed as a function of the angle for the given values of the energy-loss and temperature. The intensities have been normalized to a similar measurement at an energy-loss of 4 eV (not shown). The vertical dashed bars indicate “nodal” directions defined in Fig. 3.7 as determined from the crystal structure (Fig. 3.8).

$$W(\phi) = \frac{\int_{\omega_0}^{\omega_1} d\omega \omega \operatorname{Im} \left(-\frac{1}{\epsilon(\omega, \phi)} \right)}{\int_{\omega_0}^{\omega_1} d\omega \omega \operatorname{Im} \left(-\frac{1}{\epsilon(\omega, \phi_0)} \right)}, \quad (3.2)$$

evaluated between the low- (ω_0) and high-energy (ω_1) cutoff. The angle ϕ is measured with respect to the antinodal direction and ϕ_0 corresponds to the angle where the weight

3. EELS On Underdoped Cuprates

has its maximum (see the caption of Fig. 3.22 for details). Note that the calculated integrals do not directly measure the density of the charge carriers as given by Eq. 2.14 because the measured intensities are not given on an absolute scale via a KRAMERS-KRONIG transformation and the elastic line still contributes to the spectral weight in the vicinity of the low-energy cutoff (see also Fig. 3.15). But the anisotropy shown in Fig. 3.22 is definitely *not* caused by an angular dependent quasi-elastic line as the normalization indicated in Fig. 3.19 results also to elastic tails that are angular independent. Therefore we take the integrals shown in Fig. 3.22 as a qualitative measure of the charge density which is then inhomogeneously distributed, with the periodicity of 90° also observed for the intensities (Fig. 3.19 and Fig. 3.21). The plasmon carries most of the weight for $\omega \leq 2$ eV, which becomes overcompensated by the charge-transfer-peak for higher energy cutoffs. This could be expected already by visual inspection of Fig. 3.19 and remembering that the spectral weight is given by the first moment of the loss function. This is a remarkable fact given that the sum-rule for the loss function is actually independent of momentum as discussed in relation to Eq. 2.13. In other words the weights shown in Fig. 3.22 are expected to be the same for all angles if the integrals are evaluated up to high enough cutoffs, which is implicitly assumed to be the case for $\omega_1 = 3$ eV (see also the caption of Fig. 3.22).

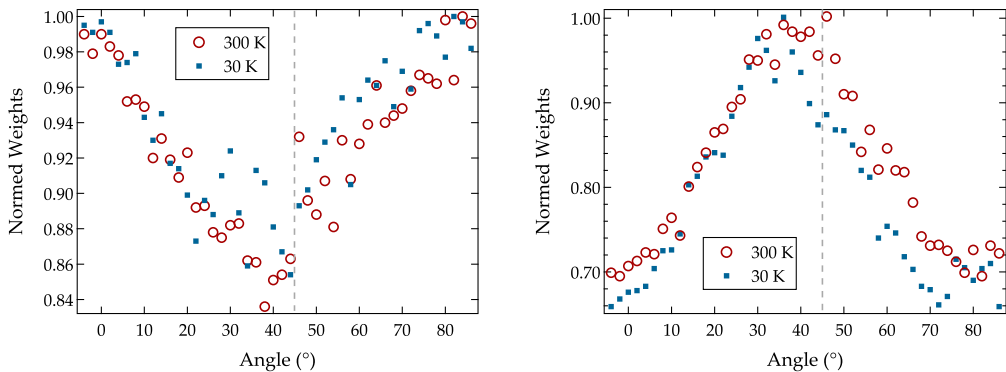


FIGURE 3.22.: The normed spectral weight (see Eq. 3.2) as extracted from the maps in Fig. 3.19 integrated between $\omega_0 = 0.5$ eV and $\omega_1 = 3$ eV, $\phi_0 = 0^\circ$ (left panel) and $\omega_0 = 0.5$ eV, $\omega_1 = 1.5$ eV, $\phi_0 = 40^\circ$ (right panel) as a function of the angle within the CuO_2 plane. For $\omega_1 > 3$ eV the results do not change as the energy where the weight is nearly independent of the angle lies around 2.5 eV.

To emphasize it from the very beginning, at present it is *not* clear what microscopic mechanisms are responsible for the intriguing findings described above. But, naturally there is room for speculations and in the following we are going to discuss possible scenarios for an at least qualitative understanding.

3.4. Evolution Of The Charge Carrier Plasmon

“Charge-Order Scenario” In general, i. e., for inhomogeneous systems the dielectric function described in Sect. 2.4 is a symmetric tensor of rank two

$$\epsilon = \begin{pmatrix} \epsilon_{xx} & \epsilon_{xy} & \epsilon_{xz} \\ \epsilon_{yx} & \epsilon_{yy} & \epsilon_{yz} \\ \epsilon_{zx} & \epsilon_{zy} & \epsilon_{zz} \end{pmatrix} \quad \text{with} \quad \epsilon_{ij} = \epsilon_{ji} \quad i, j \in \{x, y, z\}.$$

According to the general wisdom [65, 120, 134] and also the experimental finding from Fig. 3.8 $\text{Ca}_{2-x}\text{Na}_x\text{CuO}_2\text{Cl}_2$ is a perfect tetragonal system without any orthorhombicity or buckling that is often found in other cuprate families. Therefore following a group-theoretical analysis of this crystal symmetry [135, 136], the above given tensor is diagonal and has a particularly simple inverse

$$\epsilon = \begin{pmatrix} \epsilon_{xx} & 0 & 0 \\ 0 & \epsilon_{xx} & 0 \\ 0 & 0 & \epsilon_{zz} \end{pmatrix} \implies \epsilon^{-1} = \begin{pmatrix} \epsilon_{xx}^{-1} & 0 & 0 \\ 0 & \epsilon_{xx}^{-1} & 0 \\ 0 & 0 & \epsilon_{zz}^{-1} \end{pmatrix},$$

where the indices x, y, z correspond to the axes of the real and—even more importantly, in the present case—reciprocal lattice. Consequently the EELS response within the CuO_2 plane is given by

$$\frac{d^2\sigma}{d\Omega d\omega} \propto \text{Im} \left(\epsilon^{-1} \right) = \text{Im} \left(\epsilon_{xx}^{-1} \right),$$

and therefore *should be* isotropic in the plane, i. e., characterized by a single term in the limit $q \rightarrow 0$. As can be seen from the spectra of $\text{Ca}_{1.95}\text{Na}_{0.05}\text{CuO}_2\text{Cl}_2$ and also $\text{Sr}_2\text{CuO}_2\text{Cl}_2$ (cf. Fig. 3.9) in general this is fulfilled for the smallest possible values of momentum. Note, that setting the momentum transfer to $q \leq 0.1 \text{ \AA}^{-1}$ enhances the influence of surface scattering which will then dominate the spectrum [137] prohibiting a reliable data evaluation. Moreover the contribution of the elastic line will become more and more important in this momentum range. Motivated by the smallness of q —which amounts to only about 6% of the size of the BRILLOUIN zone in the experiments leading to the asymmetry for $\text{Ca}_{1.9}\text{Na}_{0.1}\text{CuO}_2\text{Cl}_2$ —one may consider this effect as being caused by the appearance of a second in-plane component in the dielectric tensor that is (for $q \equiv 0$) only possible for a twofold symmetric system [135, 136]. This leads naturally to charge- and/or spin-order scenarios.

On the one hand it was mentioned in Sect. 3.2 that the underdoped regime of the cuprates is characterized by the appearance of inhomogeneous charge- and spin-densities. In particular the system $\text{Ca}_{2-x}\text{Na}_x\text{CuO}_2\text{Cl}_2$ was reported to show a $4a_0 \times 4a_0$ superstructure (with a_0 the lattice constant)—called “checkerboard”—in the scanning-tunneling microscope (STM) for temperatures well below 1 K [138]. There is however

3. EELS On Underdoped Cuprates

experimental evidence for the absence of long-range bulk order from x-ray scattering for the compound with $x = 0.08$ [139]. This is in perfect agreement with what is observed in the EELS where no evidence of superstructure reflections (not even at low temperatures) could be found. It also agrees with the theoretical treatment of Ref. 140 where it was argued that the checkerboard is a peculiarity of the surface—probed by STM—and does not reflect the bulk behavior accessible for the EELS. On the other hand there is also evidence for short-range glassy behavior in the underdoped cuprates [90, 141, 142]. If there are stripe-like domains inside the CuO_2 plane they will create a so called nematic order by locally breaking the symmetry from C_4 down to C_2 . This leads naturally to the appearance of two in-plane components of the dielectric tensor [135, 136]. According to Refs. 141–144 the checkerboard pattern observed in the STM is compatible with this local symmetry breaking. Along such a stripe domain there will be metallic characteristics like easy charge propagation and also a large screening whereas perpendicular to it charges are confined and the screening is weak. If there was a single domain of this order there would, however, be a distinguished axis (parallel to the stripes) and the symmetry would really become broken on a large scale from tetragonal to orthorhombic. This is not what we observe. Instead there must be spatially separated domains of stripes that are perpendicular to each other. Otherwise there is no reason for perpendicular directions to produce an identical signal in EELS. A schematic account of the effect is given in Fig. 3.23. Note that the size of these domains must be substantial. Translating $q = 0.1 \text{ \AA}^{-1}$ to real space results in a typical length scale of $l \approx 60 \text{ \AA}$ which is significantly larger than the structures that appear as checkerboards in the STM. If they were smaller the wavelength of the EELS electrons would average over them, with the result being a homogeneous signal, in contrast to the experimental observation. The orientation of the domains is not necessarily constant in time. Instead they may be fluctuating [89]. But assuming that the reorientation of these glassy stripes involves also the lattice via electron-phonon coupling these fluctuations can be considered very slow compared to the short timescale of the EELS process so that the experimentally observed effect is just a snapshot of the order that has structure in space and time. It is also important to realize that the presence of charge order does not necessarily exclude the existence of well-defined quasiparticles. In $\text{La}_{2-x}\text{Ba}_x\text{CuO}_4$ with $x = 0.125$ a compound which is known to exhibit long-range order in the bulk, photoemission finds quasiparticle states along the nodal direction [145]. A similar effect is observed in $\text{Ca}_{2-x}\text{Na}_x\text{CuO}_2\text{Cl}_2$ [146].

There are nevertheless several problems related to this interpretation. It is known from $\text{La}_{2-x}\text{Sr}_x\text{CuO}_4$ that the stripes run along the diagonal direction for $x < x_c$ below but parallel to the principal axes for $x > x_c$ where x_c is the concentration of the metal-insulator transition [147] an effect also found in the nickelates [148]. As discussed

3.4. Evolution Of The Charge Carrier Plasmon

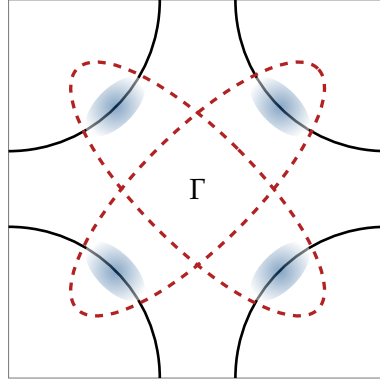


FIGURE 3.23.: Possible effect of a glassy order on the optical response. The ellipses describe different domains inside the CuO_2 plane with metallic (insulating) character along their long (short) axes. The solid barrels correspond to the underlying FERMI surface of the optimally doped compounds and the shading indicates the regions where the plasmon appears. The image is highly schematic as it combines real (ellipses) and reciprocal space (the FERMI surface). See text for details.

above $\text{Ca}_{1.9}\text{Na}_{0.1}\text{CuO}_2\text{Cl}_2$ is metallic but the metallicity seen in the EELS—reflected by the appearance of the plasmon—is obviously more pronounced along the diagonal direction which contradicts the foregoing. Note that the checkerboards in the STM are also oriented along the principal axes. Another effect that contradicts the observations discussed above is that in the compounds which are known to exhibit long-range order the anisotropy of the charge transport is strongly temperature dependent [149]. Maybe this can be reconciled assuming that a glassy like order is highly fluctuating and only locks in at very low temperatures which are not accessible in the EELS where cooling below $T \sim 20$ K is hampered by the transmission geometry. Finally, it is important to keep in mind that EELS never measures at $q = 0$. Therefore the above given reasoning concerning the appearance of a second in-plane component of the dielectric tensor—which is strictly valid only for zero momentum—should be handled with care, although it is nevertheless quite astonishing that the discussed effect has never been observed in any other system.

“Arc-Scenario” Another possible approach which does not directly require the existence of charge- and/or spin-order involves the development of the FERMI surface with doping. From ARPES investigations on the $\text{Ca}_{2-x}\text{Na}_x\text{CuO}_2\text{Cl}_2$ system it is known that the underdoped compounds exhibit the FERMI surface arc that was mentioned already in Sect. 3.2 [146, 150]. This means that well defined quasiparticles exist only in the nodal region whereas the spectrum in the antinodal region is dominated by broad features. Moreover the existence of the pseudogap leads to a strong suppression of

3. EELS On Underdoped Cuprates

the spectral weight away from the node. In other words in this region of momentum space the pseudogap, whatever its origin is, does not allow the existence of a metallic band that may host a plasmon as its characteristic feature in the two-particle channel. Therefore one may conclude that the intensity enhancement around 1 eV observed for momentum transfers parallel to the (100), i. e., the arc direction simply reflects the response of the FERMI surface arc. This, however, is misleading, for several reasons.

Starting from the perspective of the large FERMI surface of the overdoped compounds and employing a framework developed for $\text{Bi}_2\text{Sr}_2\text{CaCu}_2\text{O}_{8+\delta}$ where the susceptibility $\chi(\mathbf{q}, \omega)$ being related to the dielectric function via Eq. 2.7 can be expressed according to

$$\chi(\mathbf{q}, \omega) \propto \langle (\mathbf{q} \cdot \mathbf{v})^2 \rangle_{\text{FS}} + \frac{\langle (\mathbf{q} \cdot \mathbf{v})^4 \rangle_{\text{FS}}}{(\hbar\omega)^2} + \frac{1}{12} \left\langle (\mathbf{q} \cdot \mathbf{v}) \left(\mathbf{q} \cdot \frac{\partial}{\partial \mathbf{k}} \right)^2 (\mathbf{q} \cdot \mathbf{v}) \right\rangle_{\text{FS}} \quad (3.3)$$

with $\mathbf{v} = \nabla_{\mathbf{k}} E(\mathbf{k})$ and $\langle \dots \rangle_{\text{FS}}$ indicates an averaging over the FERMI surface [128, 133] it can be seen that the EELS signal within a particular direction \mathbf{q} is influenced by all other areas of the FERMI surface due to the averaging procedure. Consequently, the signal measured “in the nodal direction” always contains information from the region where the pseudogap is largest. Therefore the signal along the diagonal does not solely probe the arc. In addition the size of the pseudogap in underdoped cuprates is smaller than 100 meV—an energy scale well below the plasmon energy of 1 eV. In more conventional systems like silicon with a band gap of ~ 1.1 eV the volume plasmon located at 16.7 eV in this case behaves essentially as if it were created by free electrons [151] (in agreement with Eq. 2.17). Assuming this to be a generic feature of an electron gas, this implies that the pseudogap should not be visible at all in the EELS signal at the energies of the plasmon and therefore the plasmon should behave like in the optimally doped compounds. The data are in obvious conflict with this reasoning. Another point arguing against “arc physics” is the temperature independence of the angular range over which the plasmon is visible (cf. Fig. 3.20). This is in contrast to the behavior which is observed in ARPES where the arc clearly shrinks with decreasing temperature [96]. If EELS were indeed able to probe the arc, one should see its temperature dependence, which is not the case. Finally it is clear that the development of the FERMI surface with doping does not break the symmetry of the underlying lattice, i. e., independent of whether the underdoped compounds show arcs or closed pockets around the nodal direction there are four of them (one at each node) arranged in a tetragonal symmetry. It is therefore not clear how the shape of the FERMI surface alone can produce several components of the dielectric tensor, necessary to induce the anisotropic response in $\text{Ca}_{1.9}\text{Na}_{0.1}\text{CuO}_2\text{Cl}_2$.

3.4. Evolution Of The Charge Carrier Plasmon

“Momentum-Dependent Metal-Insulator Transition” There is another possible scenario which is certainly related to the physics of the FERMI arc and might even provide an explanation for its physical origin.

It was mentioned above that the metal-insulator transition in a strongly-correlated system is driven by the redistribution of spectral weight between the upper/lower HUBBARD band and the quasiparticle states in the vicinity of the FERMI level. There is a subtlety related to this [152, 153]. Considering first a conventional semiconductor with N sites, it is clear that the spectral weight for removing (adding) an electron from (to) the valence (conduction) band is $2N$. If such a system is doped with a single hole the chemical potential will shift into the valence band and the spectral weight for electron removal (addition) will become $2N - 1$ ($2N + 1$), with the weight for electron addition being distributed between a high-energy part (the conduction band) and a low-energy part (the empty state in the vicinity of the FERMI level). The important point to realize is that the high-energy part is *unaffected* by the doping and the low energy spectral weight simply scales with the doping.

This situation is different for a MOTT insulator in the strongly correlated regime ($U/t \gg 1$). There, both, the lower *and* the upper HUBBARD band have a weight equal to $N - 1$ when one hole is doped. This is because states in the upper HUBBARD band can only be occupied if the state in the lower HUBBARD band is already filled, which is not the case if a hole is doped (an electron is removed) from the chain. Simultaneously, there are two possibilities to add an electron near the FERMI level to the site which is empty. Hence, there occurs a transfer of spectral weight from the upper to the lower HUBBARD band, i. e., states are transferred from high to low energies with the low-energy weight scaling with twice the doping.

While the former two scenarios are particle-hole symmetric the special point behind the cuprates is that they are charge-transfer insulators. This means that in the localized limit ($t \rightarrow 0$) doping the system with electrons corresponds to the case of the MOTT insulator—because electrons are doped into the upper HUBBARD band—but the addition of holes with which we are concerned with in the $\text{Ca}_{2-x}\text{Na}_x\text{CuO}_2\text{Cl}_2$ system is reminiscent of the conventional band insulator. As a consequence one would, at first sight, not expect a spectral weight transfer between high and low energy scales. This situation changes considerably as soon as hybridization is switched on [153]. Then the ZHANG-RICE-singlet-band forms which has substantial contributions from the Cu d -orbitals. It is because of this effect that cuprates, though being of charge-transfer-type, also exhibit spectral weight transfer upon hole doping.

With this at hand it is also clear, how to relate the observations summarized in Fig. 3.19 to this scenario. The spectral weight around 1 eV corresponds to states created at the FERMI level around the nodal direction. Due to the EELS process—which probes

3. EELS On Underdoped Cuprates

collective excitations (see Ch. 2)—these states show up at finite energies but one may speculate that the arc seen in ARPES is just the single-particle image of the same physics. The prize the system has to pay for the enhancement of the quasiparticle states is a loss of weight in the upper HUBBARD band which explains the drop in the intensity around 2 eV in $\text{Ca}_{1.9}\text{Na}_{0.1}\text{CuO}_2\text{Cl}_2$. This spectral-weight depletion is, however, not accessible for photoemission where the unoccupied part of the spectrum is invisible.

This scenario is also compatible with theoretical investigations. Cluster extensions of DMFT [154, 155] and variational cluster approaches [156] indeed show that upon doping spectral weight at the FERMIL level is created first around the nodal direction, in agreement with the results shown in Fig. 3.19.

The problem with this approach is that the creation of a “nodal metal” [125] also preserves the symmetry of the lattice as this momentum dependent metal-insulator transition happens simultaneously around all four nodes in the BRILLOUIN ZONE. To reconcile this with the observed asymmetric signal which actually breaks the underlying lattice symmetry (see above) one has to postulate a momentum dependent joint-density of states [50] which produces the observed intensity oscillations. This is clearly a task for theory. A further drawback of this model is that the averaging (Eq. 3.3) also has to be performed and this always leads to the appearance of a “nodal signal” in the antinodal direction. The benefit compared to the “arc-physics” discussed in the ARPES community is that the energy scale involved in the spectral weight transfer is on the order of eV rather than the pseudogap range of meV. Therefore even EELS is sensitive to this physics and this may also provide the reason why the observed effect is so robust against temperature variations.

In conclusion there is an obvious dilemma and the way out of it is to perform more experiments. To this end several approaches may be taken. An effect of the pseudogap on the plasmon is rather unlikely due to the large mismatch in the involved energy scales. The spectral weight transfer is something which should be observable in other cuprates as well. Therefore one may probe $\text{La}_{2-x}\text{Sr}_x\text{CuO}_4$ or also $\text{Bi}_2\text{Sr}_2\text{CaCu}_2\text{O}_{8+\delta}$. The latter one has several additional advantages: it can be prepared rather easily for EELS, there are plenty of results from photoemission available that may help to relate the potential outcome to the properties of the observed arc and there are so far no reports about stripe-physics or other types of charge order so that this effect can be excluded in this case.

To disentangle the role of order on the plasmon peak it is necessary to investigate compounds which have proved to show charge- and/or spin-order, in particular from the lanthanum family or even the nickelates. If stripes are responsible for the anisotropic charge response, than one can expect even larger effects than those discussed above. In

3.4. Evolution Of The Charge Carrier Plasmon

particular there is a characteristic momentum—corresponding to the periodicity of the ordering pattern—that should be visible in the elastic channel as well as the electronic spectrum, i. e., the loss function.

Beyond this there is clearly a need for theoretical input that has to clarify how to understand the emergence of the collective mode on the background of a strongly incoherent single-particle spectrum.



4. EELS On Transition-Metal Dichalcogenides

4.1. Introduction

COMPARED to the cuprates the transition-metal dichalcogenides are much longer known. The first comprehensive experimental survey of their structural and electronic properties date back to the 1960s [157, 158]. Since then there are naturally numerous investigations on them but it is probably not overstated that interest in them changed with time. When first discovered it was quickly realized that they may be considered as prototype materials for the occurrence of charge-density waves (CDW) in low dimensions [158–160]. After the seminal contributions by LITTLE [161] and GINZBURG (for a review see [162], and in particular [163]) predicting possible superconductivity due to electron-electron interactions without the explicit need for a mediating phonon, research on these compounds was revived as it was realized that intercalating them with organic molecules can enhance the superconducting T_c [164, 165]. Taking these statements together already tells that the transition-metal dichalcogenides show several order parameters, most prominently CDW and superconductivity. The hype of the cuprates and the discovery that they also reveal—at least in some regions of their phase diagram—these two ordering phenomena in close proximity to each other breathed new fire into the research on the chalcogenides and with time claims appeared that cuprates and the transition-metal dichalcogenides share common features in particular concerning “pseudogap-physics” [166]. To be more precise there is evidence from ARPES that the temperature evolution of the pseudogap is universal between these two classes [167, 168] and also the optical properties argue for similarities namely the coexisting of metallic transport with a gap in the single-particle spectrum [169, 170] and even the presence of the still mysterious mid-IR peak [120, 125, 170] is observed in both material classes.

Another common feature of cuprates and dichalcogenides is the absence of a profound theoretical understanding of the mechanisms leading to the phase transitions, although in both cases there is a large amount of data available. Some scenarios for the CDW formation in the chalcogenides will be briefly mentioned below and there

4. EELS On Transition-Metal Dichalcogenides

are hints that the recently discovered superconductivity in the iron-pnictides [171] may add another piece to this puzzle.

4.2. Basic Properties

1 H Hydrogen 1.00794																	2 He Helium 4.003										
3 Li Lithium 6.941	4 Be Beryllium 9.012182																	10 Ne Neon 20.1797									
11 Na Sodium 22.989770	12 Mg Magnesium 24.3050																	18 Ar Argon 39.948									
19 K Potassium 39.0983	20 Ca Calcium 40.078	21 Sc Scandium 44.955910	22 Ti Titanium 47.867	23 V Vanadium 50.9415	24 Cr Chromium 51.9961	25 Mn Manganese 54.938049	26 Fe Iron 55.845	27 Co Cobalt 58.933200	28 Ni Nickel 58.6934	29 Cu Copper 63.546	30 Zn Zinc 65.39	31 Ga Gallium 69.723	32 Ge Germanium 72.61	33 As Arsenic 74.92160	34 Se Selenium 78.96	35 Br Bromine 79.904	36 Kr Krypton 83.80										
37 Rb Rubidium 85.4678	38 Sr Strontium 87.62	39 Y Yttrium 88.90585	40 Zr Zirconium 91.224	41 Nb Niobium 92.90638	42 Mo Molybdenum 95.94	43 Tc Technetium (98)	44 Ru Ruthenium 101.07	45 Rh Rhodium 102.90550	46 Pd Palladium 106.42	47 Ag Silver 107.8682	48 Cd Cadmium 112.411	49 In Indium 114.818	50 Sn Tin 118.710	51 Sb Antimony 121.760	52 Te Tellurium 127.60	53 I Iodine 126.90447	54 Xe Xenon 131.29										
55 Cs Cesium 132.90545	56 Ba Barium 137.327	57 La Lanthanum 138.9055	72 Hf Hafnium 178.49	73 Ta Tantalum 180.9479	74 W Tungsten 183.84	75 Re Rhenium 186.207	76 Os Osmium 190.23	77 Ir Iridium 192.217	78 Pt Platinum 195.078	79 Au Gold 196.96655	80 Hg Mercury 200.59	81 Tl Thallium 204.3833	82 Pb Lead 207.2	83 Bi Bismuth 208.98038	84 Po Polonium (209)	85 At Astatine (210)	86 Rn Radon (222)										
87 Fr Francium (223)	88 Ra Radium (226)	89 Ac Actinium (227)	104 Rf Rutherfordium (261)	105 Db Dubnium (262)	106 Sg Seaborgium (263)	107 Bh Bohrium (262)	108 Hs Hassium (265)	109 Mt Meitnerium (266)	110 (269)	111 (272)	112 (277)	113	114														
58 Ce Cerium 140.116	59 Pr Praseodymium 140.90765	60 Nd Neodymium 144.24	61 Pm Promethium (145)	62 Sm Samarium 150.36	63 Eu Europium 151.964	64 Gd Gadolinium 157.25	65 Tb Terbium 158.92534	66 Dy Dysprosium 162.50	67 Ho Holmium 164.93032	68 Er Erbium 167.26	69 Tm Thulium 168.93421	70 Yb Ytterbium 173.04	71 Lu Lutetium 174.967	90 Th Thorium 232.0381	91 Pa Protactinium 231.03588	92 U Uranium 238.0289	93 Np Neptunium (237)	94 Pu Plutonium (244)	95 Am Americium (243)	96 Cm Curium (247)	97 Bk Berkelium (247)	98 Cf Californium (251)	99 Es Einsteinium (252)	100 Fm Fermium (257)	101 Md Mendelevium (258)	102 No Nobelium (259)	103 Lr Lawrencium (262)

FIGURE 4.1.: The periodic table of the elements showing possible combinations to realize compounds in the family of the transition-metal dichalcogenides.

The family of the transition-metal dichalcogenides is huge. To give a first impression the periodic table shown in Fig. 4.1 summarizes the elements to realize their most important members. The general stoichiometry is TX_2 with a transition metal $T=Ti, Nb, Ta, \dots$ bound to two chalcogenides $X=S, Se, Te$. All members show layered structures with only weak VAN DER WAALS interlayer interactions and a stacking $X-T-X$. The layering allows several geometrical arrangements leading to numerous polymorphs which are labeled according to the scheme nP_α with n the number of layers in the unit-cell, P the polymorph indicating the bonding geometry between the transition-metal and the chalcogenide and α an optional letter that is used if the former two characteristics do not suffice to determine the structure uniquely. The two basic building blocks are the trigonal prismatic ($2H$) and octahedral ($1T$) arrangement which form polymorphs of their own but can also be combined into larger unit cells. An overview can be found in Fig. 4.2. In the following we will concentrate mostly on the $2H$ modification.

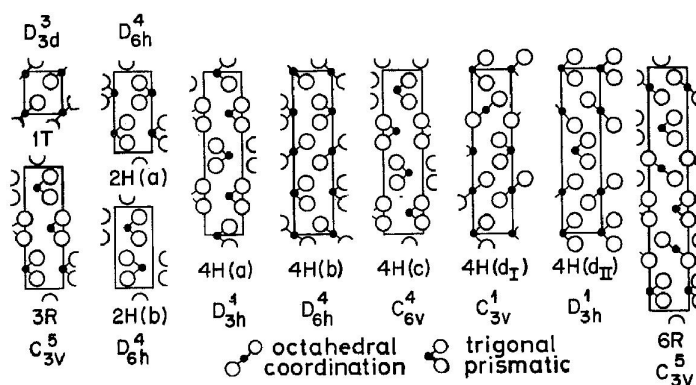


FIGURE 4.2.: The different polymorphs of the transition-metal dichalcogenides with the transition-metal (chalcogenide) shown as solid (empty) circles, respectively. The labels with(out) the superscript indicate the polymorph (point-group). Image taken from [160].

We will further limit ourselves to representatives containing group V elements, in particular $2H\text{-TaSe}_2$, $2H\text{-NbSe}_2$, $2H\text{-TaS}_2$ and $2H\text{-NbS}_2$. This is due to the fact that in an ionic picture the TX_2 stoichiometry with X^{2-} requires four valence electrons from the transition metal for the bonding. Therefore the members of group IV and IV have an empty and completely filled conduction band, respectively and only the five valence electrons of the group V elements form a half filled d_{z^2} band, and hence metallic behavior [165]. Indeed, the most interesting physical properties like the charge order and (multiband [172]) superconductivity are observed for the members of this group.

A more detailed impression of the $2H$ polymorph is depicted in Fig. 4.3. Obviously each transition-metal site sits in the center of a trigonal prism that is aligned along the crystallographic c -axis. Within the plane the transition-metal atoms are organized in a hexagonal pattern which naturally leads also to a hexagonal BRILLOUIN ZONE. From Fig. 4.2 it is clear that the different modifications are basically distinguished by the stacking along the c -axis and together with the layered structure one would conclude that the in-plane physics should be very similar.

Indeed bandstructure calculations [173–177] indicate that for both polymorphs the dominant orbital contribution to the density of states comes from the d_{z^2} states. However the different geometrical surroundings—the crystal field—seen by the transition metal in the octahedral and trigonal prismatic structure influence, in particular the d manifold [177]. This leads to different properties for the $2H$ and $1T$ modification. In particular the resulting FERMI surface pockets are substantially larger for the $2H$ resulting in a much higher electron density.

4. EELS On Transition-Metal Dichalcogenides

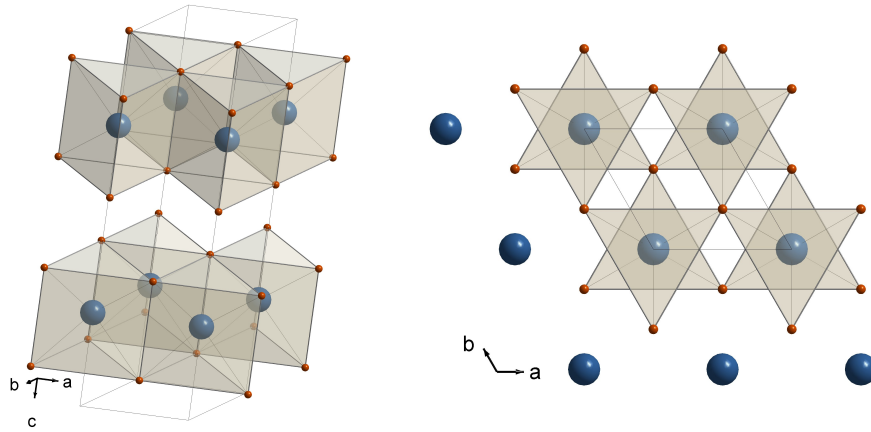


FIGURE 4.3.: The crystal structure of the $2H$ modifications. The perspective view in the left panel indicates the trigonal prismatic surrounding of the transition-metal (large blue circles) and the top-view (right panel) their hexagonal arrangement in the plane when considering more than one unit-cell.

Another, certainly related, difference lies in the much stronger CDW effects in the $1T$ polymorphs [178]. To this end Fig. 4.4 compares the temperature dependence of the resistivities for the most important members. There are anomalies in both families associated with the appearance of the charge order. While the phase transitions in the $1T$ polymorph partly lie above room temperature and invoke a strong increase of the resistivity, the ordering occurs at much lower temperatures for the $2H$ members and causes a *decreasing* resistivity. This forms a significant puzzle as it contradicts the simple expectation that the appearance of charge order opens up a gap on the FERMI level (see Fig. 2.5). We will briefly discuss possible reasons for this below when mentioning some of the proposed scenarios for the CDW origin.

A further peculiarity is provided by Tab. 4.1 where the transition temperatures to the superconducting and charge-ordered states are summarized.

All members, except for $2H\text{-NbS}_2$ (see also Fig. 4.4) exhibit a transition to a charge ordered phase and there is an obvious tendency for the two order parameters—superconductivity and CDW—to compete for the FERMI surface. In a mean-field approach this can be understood at least qualitatively as T_c and T_{CDW} are both depending on the density of states and if the CDW is strong enough to gap already a large portion of the FERMI surface there is little phase space left for superconductivity and the resulting T_c values tend to be rather small.

The subtle interplay between both orders is further corroborated by the observation that it is possible to “switch on” superconductivity by intercalating the host material with metallic donors [181–183]. In particular the recent observation of superconductivity

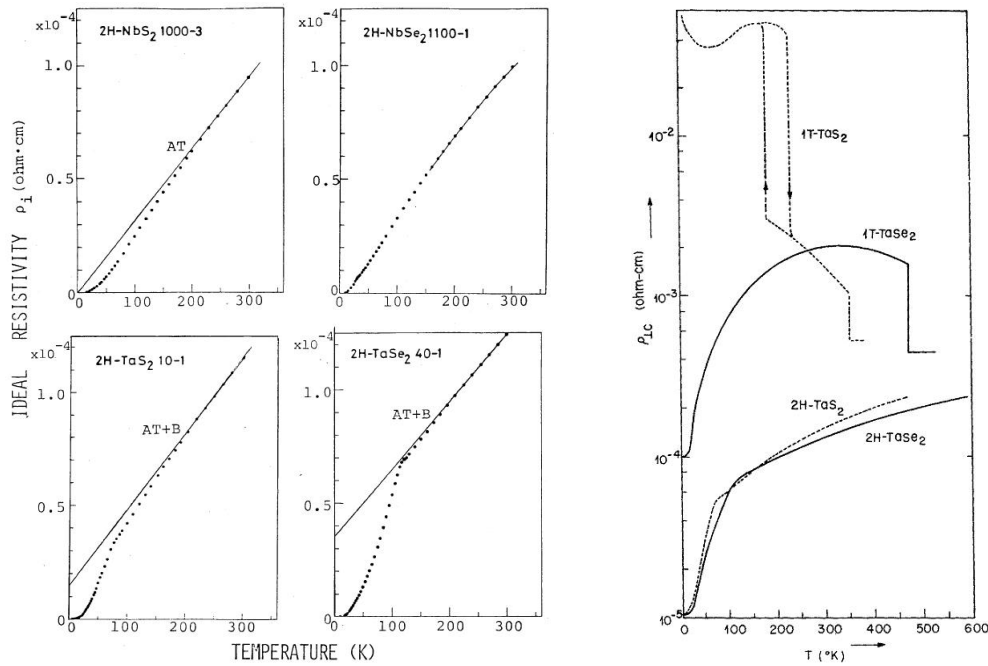


FIGURE 4.4.: Resistivity vs. temperature for several transition-metal dichalcogenides of the 2H modification taken from Ref. 179. There is a well pronounced kink for all compounds except for $2H\text{-NbS}_2$, indicating the absence of CDW order in this particular case (left panel). Comparison of the resistivities for representatives of the 1T and the 2H polymorphs taken from [160] (right panel).

TABLE 4.1.: Critical temperatures for the phase transition to the superconducting state (T_c) and the CDW ordered phase T_{CDW} for selected representatives of the 2H modification, taken from Refs. 158, 180 (see also Ref. 179). All T_{CDW} temperatures are for the transition to an incommensurate state. $2H\text{-TaSe}_2$ also has a commensurate phase that appears at about $T = 90$ K.

	T_c (K)	T_{CDW} (K)
$2H\text{-TaSe}_2$	0.15	120
$2H\text{-TaS}_2$	0.65	77
$2H\text{-NbSe}_2$	7.2	33.5
$2H\text{-NbS}_2$	6.1	—

induced by copper intercalation into $1T\text{-TiSe}_2$ [184] triggered substantial interest; all the more because this compound appears rather special in that it seems to be a rare manifestation of the so called excitonic insulator [185]—a particular type of CDW ordered state that has been predicted to occur under certain circumstances [186, 187].

4. EELS On Transition-Metal Dichalcogenides

In any case the critical temperatures for the onset of superconductivity remain below 10 K which is hard to access in the transmission geometry of the EELS and we therefore concentrate on the CDW in the following.

To gain a deeper insight into the processes related to the CDW transition Fig. 4.5 shows the Fermi surface of $2H\text{-TaSe}_2$ measured for temperatures above and below the transition to the charge-ordered state [167].

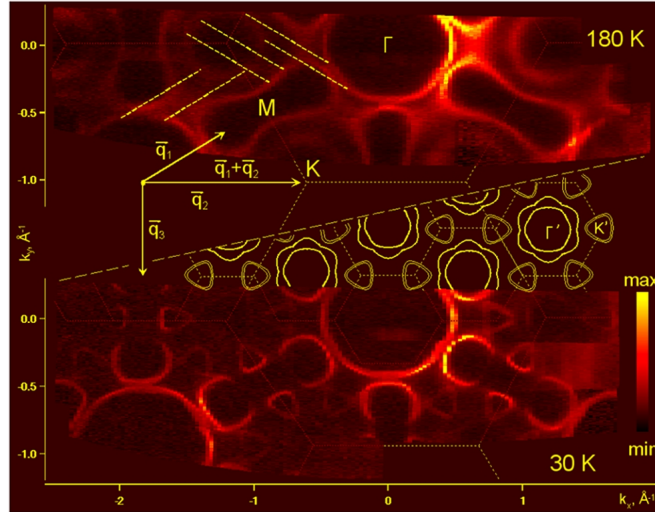


FIGURE 4.5.: The Fermi surface of $2H\text{-TaSe}_2$ and its reconstruction for temperatures above (upper panel) and below (lower panel) the transition to the commensurate CDW phase. The yellow arrows indicate the nesting vectors. Image taken from Ref. 167.

The electronic structure is indeed very complex. There are two bands observable. One is responsible for the electron-like pocket around the M point and the other one forms the hole-like barrels around Γ and K . In addition the onset of the charge-order causes a substantial folding of the bands accompanied by the occurrence of gaps in the single-particle spectrum which open predominately at those points that are connected by the nesting vectors. From similar measurements on $2H\text{-NbSe}_2$ [188] it is also known that these so called “hot-spots” are also the points where the superconducting gap is zero. This underlines once more the obvious competition between the two ordering phenomena and it points to a prominent role of the conventional PEIERLS-like nesting scenario for the origin of the CDW.

While this is certainly appealing and the majority of past investigations adopt this line of reasoning, there is evidence that other mechanisms might also be able to capture at least some parts of the relevant physics. It was realized early on that the conventional nesting scenario is not capable of describing the simultaneous appearance of gaps in the single-particle spectrum and the enhanced metallic character (see Fig. 4.4) in

the ordered state. Therefore the authors of Ref. 189 developed a different approach that relies on the presence of saddle points on the FERMION level that are connected by the CDW vector and the gap therefore opens only in this momentum range. With the gapping of these regions of high-density of states, the scattering of the charges is strongly reduced, leading to a drop in the resistivity when entering the ordered state. Later investigations revealed however that the saddle points are too far away from the FERMION level suppressing the required singularity in the susceptibility [173, 178] and that the corresponding points are not connected by the CDW vector [190]. This argues strongly against this often called saddle-point scenario.

More recently it has been argued that the coexistence of metallic conduction and the charge order can be understood with a peculiarity of the WANNIER functions (WFs) constructed from the d_{z^2} dominated band structure at the FERMION surface [191]. It could be shown that the particular shape of the WFs leads to an enhancement of the next-nearest-neighbor compared to the nearest-neighbor-hopping and this leads to a decoupling into three independent sublattices in the ordered states with one staying undistorted forming the reason for the still metallic conduction below T_{CDW} .

Other approaches based on an extended HUBBARD model emphasize different aspects for the explanation of the CDW transition and its competition with superconductivity [192]. There it is shown that only the combined effect of saddle-points and inter-site COULOMB interaction V may give rise to a singularity in the susceptibility and that it is the V -term that decides in favor of superconducting or charge order in that superconducting pairing is driven by spin-exchange and that enhanced fluctuations in the charge channel will enhance the CDW order. Hence the problem of which order appears first is basically one that relies on the strength of spin- and/or charge fluctuations. It is, however, not clear whether the COULOMB interaction in the $4d$ and $5d$ shells is strong enough to produce substantial spin fluctuations according to the mechanism discussed in Sect. 3.2.

To conclude this incomplete list of possible mechanisms for the CDW order there are also claims that it is “simply” the influence of momentum dependent electron-phonon coupling that drives the instability [193–195].

In summary the emerging picture is still unclear on the theoretical as well as on the experimental side and besides all these mostly weak-coupling scenarios there is also evidence for substantial many-body effects in the dichalcogenides and the recent discovery of superconductivity in iron-based compounds may open the door to add another possible source or at least contribution to the CDW mechanism. We come back to this point in Sect. 4.4.

4.3. Plasmon Dispersion

To give a first overview of the optical response in the $2H$ representatives Fig. 4.6 shows the EELS intensity for $2H$ -TaSe₂ in a large energy range for momentum transfer polarized along ΓM . Due to the D_{6h} symmetry of the lattice the signal is isotropic within the plane [135] and the spectrum looks identical in the ΓK direction. The observed behavior is consistent with earlier reports [157, 196]. There is a peak around 21 eV corresponding to the bulk plasmon and several interband transitions. From the above given discussion it is clear that the $2H$ modification is metallic and one can therefore expect the appearance of a DRUDE plasmon. Indeed this is observed at about 1 eV (indicated by the arrow). Its behavior will be our main concern in the following.

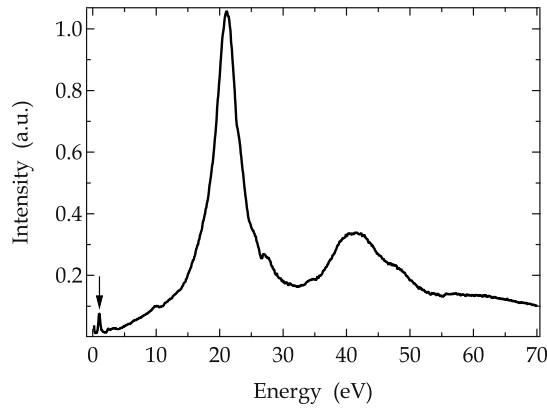


FIGURE 4.6.: The EELS intensity for $2H$ -TaSe₂ for $q = 0.1 \text{ \AA}^{-1}$ along ΓM . Besides several interband transitions and the volume plasmon around 21 eV there is the charge carrier plasmon indicated by the arrow. Except for details (see below) the response of the other representatives is very similar.

The momentum evolution in the low-energy region of the charge carrier plasmon is shown in the left panel of Fig. 4.7 along the ΓM direction of the BRILLOUIN zone. The dispersion is isotropic within the hexagonal plane and we therefore focus only on this particular polarization in the following. To minimize the influence of the elastic line the EELS intensity was fitted to a function of the form

$$\begin{aligned}
 I(\omega) &= I_0 \left[\zeta \exp(-\eta\omega^2) + \text{Im}(-1/\varepsilon(\omega)) \right] \\
 \varepsilon(\omega) &= 1 - \frac{\omega_p^2}{\omega^2 + i\gamma\omega}
 \end{aligned}
 \tag{4.1}$$

where ζ and η account for the behavior of the elastic line which is assumed to have a GAUSSIAN shape and the model dielectric function is the DRUDE behavior discussed in Sect. 2.4.3. The result of the fitting—after the subtraction of the GAUSSIAN part—is

4.3. Plasmon Dispersion

the loss function of the sample, multiplied by the intensity factor I_0 that contains all experimental details like the beam intensity or the sample quality. To obtain the true loss function $\text{Im}(-1/\epsilon(\omega))$ it is necessary to perform a KRAMERS-KRONIG transformation.

The plasmon obviously loses strength upon leaving the zone center and even more importantly it shifts to lower frequencies. This is in strong contrast to the generic metallic behavior with a *positive* dispersion discussed in relation to Eq. 2.15.

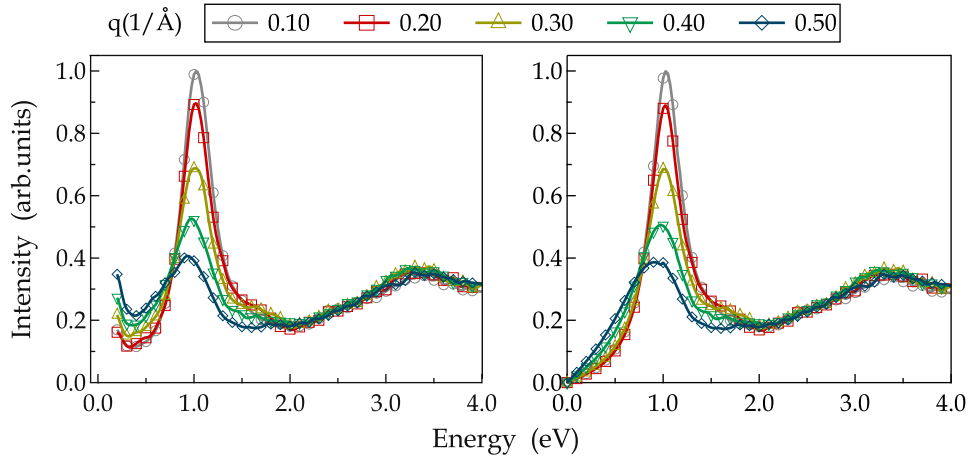


FIGURE 4.7.: The EELS intensity of $2H\text{-TaSe}_2$ in the energy range of the charge carrier plasmon before (left panel) and after (right panel) the subtraction of the elastic line according to Eq. 4.1 for the indicated values of momentum transfer polarized along ΓM . The spectra are normalized on the high-energy side. Image taken from Ref. 197.

To investigate the possible influence of the CDW order on this intriguing behavior similar spectra have been measured for $T = 60\text{ K}$. From Fig. 4.8 it is obvious that this temperature corresponds already to a well-ordered state with well pronounced superstructure reflections due to the rearrangement of the atoms within the transition-metal plane caused by the electron-phonon coupling.

The dispersion extracted from the local maximum of the EELS intensity is shown for temperatures above and below the transition to the commensurate CDW phase in Fig. 4.9. For all temperatures the plasmon velocity $v_p = \nabla_q \omega(\mathbf{q})$ is clearly negative and the bandwidth amounts to approximately 100 meV at room temperature and 150 meV in the ordered state for the considered momentum range. For higher values of momentum transfer the intensity below the plasmon peak is strongly enhanced (cf. Fig. 4.7). This makes it rather ambiguous to extract the plasmon behavior and we therefore restrict the discussion to $q \leq 0.5 \text{ \AA}^{-1}$ in the following.

In addition the onset energy shifts to higher values entering the ordered state. This is shown in more detail in Fig. 4.10 where the behavior for the loss function and ϵ_1

4. EELS On Transition-Metal Dichalcogenides

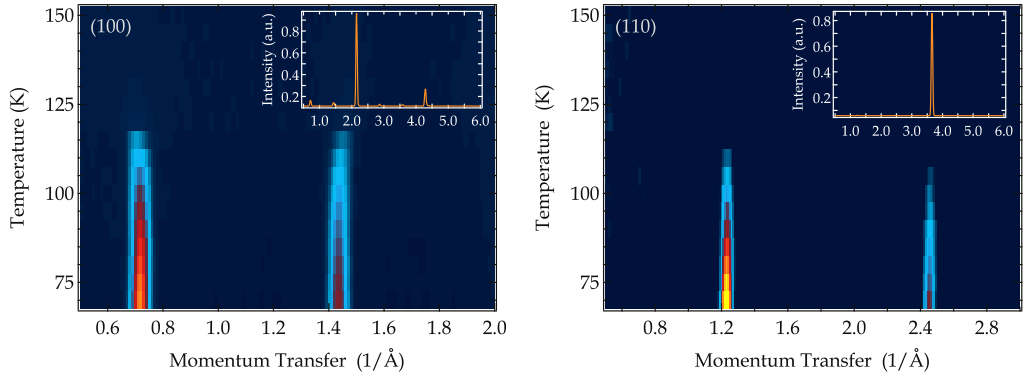


FIGURE 4.8.: Temperature dependence of the superstructure in $2H\text{-TaSe}_2$ parallel to the given lattice directions. The insets show a cut at $T = 70$ K thereby illustrating the ratio between the superstructure reflections and the main BRAGG peak. The intensity ratio for $q \parallel (110)$ amounts to $\approx 1/100$. Therefore the superstructure reflections are hardly visible in the right inset. The observed pattern is consistent with earlier reports [198–200] about the tripling of the in-plane lattice constant in the ordered state.

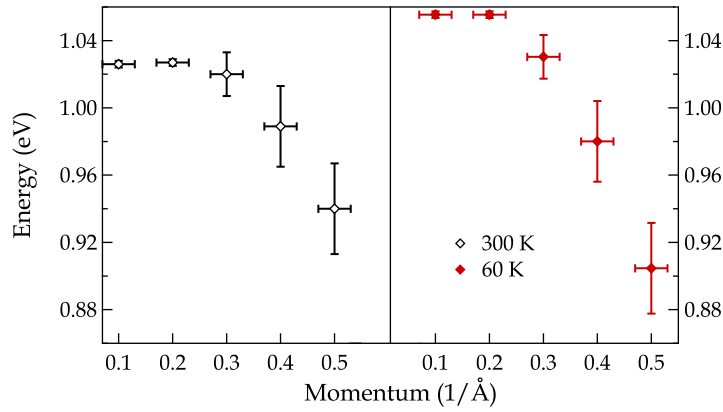


FIGURE 4.9.: The dispersion of the charge carrier plasmon in $2H\text{-TaSe}_2$ in the ΓM direction for temperatures above and below the transition to the CDW-ordered state as extracted from the peak maxima in Fig. 4.7. Image taken from Ref. 197.

is depicted. Obviously there is no change of the peak-shape upon cooling through the transition but there is clearly a blueshift of the zero-crossing in $\epsilon_1(\omega)$ causing the different onsets of the plasmon dispersion in Fig. 4.9. This behavior is consistent with earlier optical experiments [201]. There it was also discussed that this is not caused by the lattice contraction upon cooling which would lead to an enhanced electron density thereby enhancing the plasma frequency (cf. Eq. 2.10). Instead this effect is induced by the appearance of new interband transitions below the plasma energy that become

allowed owing to the band-folding in the CDW phase.* Interestingly systems where correlations are more pronounced like VO_2 show exactly the opposite trend, i. e., a red-shift of the plasmon upon cooling through the phase transition [202]. In this case the electron-electron interaction and the proximity to the MOTT insulator leads to a reduced density at the FERMI surface (see Fig. 3.2) and an enhanced effective mass, both lowering the plasma energy (see Eq. 2.10) when crossing the metal-insulator transition.

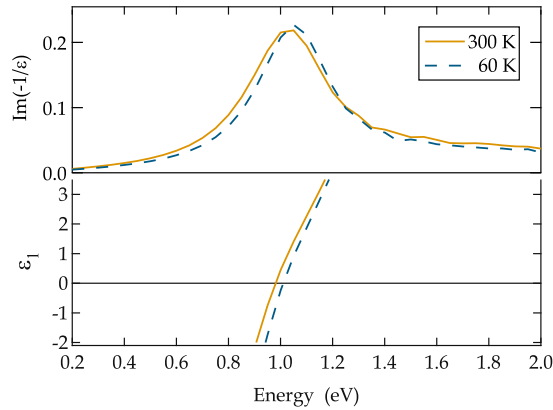


FIGURE 4.10.: The evolution of the loss function (upper panel) and ϵ_1 in the vicinity of the plasmon energy for temperatures above (solid) and below (dashed) the transition to the ordered phase for $2H\text{-TaSe}_2$.

Given the obviously robust observation of a negative plasmon dispersion in $2H\text{-TaSe}_2$ one may wonder whether this is a subtlety of $2H\text{-TaSe}_2$. From Fig. 4.11 it can however be seen that it is a general feature of the transition-metal dichalcogenides at least in the $2H$ modification. The spectral shape looks almost identical to the $2H\text{-TaSe}_2$ case and from this one may conclude that the underlying physics is universal.

This is further motivated by Fig. 4.12 where the spectral weight evolution with momentum is shown. In all cases the redshift of the plasmon energy is accompanied by a sizable loss of spectral weight in the energy range of the plasmon which together with Eq. 2.14 signals a loss of free charge carriers that could contribute to the plasmon.

Finally Fig. 4.13 summarizes the behavior of the plasmon dispersion for all the investigated compounds and compares it to the data reported in Ref. 203 for $2H\text{-NbS}_2$. There is an obvious discrepancy between this compound and all the others in that $2H\text{-NbS}_2$ clearly shows a positive slope. With the absence of a CDW transition in $2H\text{-NbS}_2$ (see Fig. 4.4) naturally the question arises whether these two phenomena may be linked.

*We still employ Eq. 4.1 to subtract the elastic line as the new transitions are not detected in the EELS. The same holds true for the opening of the CDW gap. The influence of both effects on the plasmon dispersion is discussed below.

4. EELS On Transition-Metal Dichalcogenides

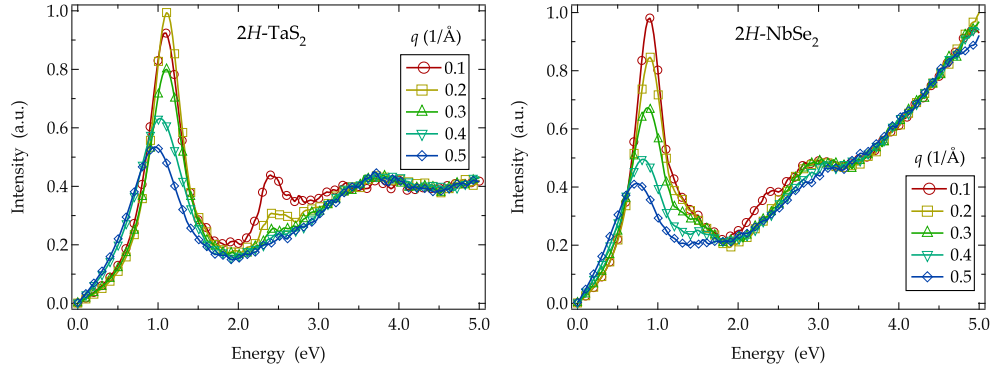


FIGURE 4.11.: Plasmon dispersion of $2H\text{-TaS}_2$ and $2H\text{-NbSe}_2$ after the subtraction of the elastic line according to Eq. 4.1 measured at room temperature. The behavior is analogous to Fig. 4.7 for $2H\text{-TaSe}_2$. The peak around 2.4 eV in $2H\text{-TaS}_2$ is probably an artifact of the employed electron-microscopy grid. The spectra are normalized on the high-energy side.

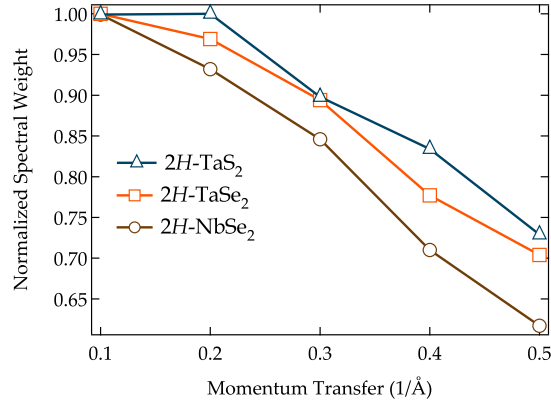


FIGURE 4.12.: The spectral weights of the plasmon peak integrated up to 2 eV normalized to their onset values for $q = 0.1 \text{ \AA}^{-1}$ for different representatives of the $2H$ -modification.

Therefore the dichalcogenides were intercalated *in situ* with potassium. This corresponds to doping additional electrons into the d_{z^2} conduction band and from earlier optical reports [204] it is known that this suppresses the CDW signatures, often even accompanied by a simultaneous enhancement of T_c [205]. From Fig. 4.14 it is clear that intercalation of K indeed causes, besides a blurring of the spectra due to the induced disorder, strong changes in the electronic structure in a large energy window. In particular there appear new interband transitions and more importantly the plasmon energy is lowered with increasing K concentration (see the inset).

This behavior was predicted in Ref. 201 in a tight-binding approach supplemented by a rigid-band model. Considering the narrow d_{z^2} band with a maximal filling of

4.3. Plasmon Dispersion

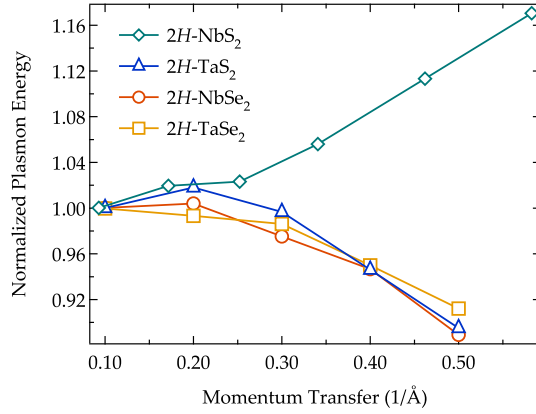


FIGURE 4.13.: The plasmon dispersion for different compounds of the 2H-modification. The energy positions are normalized to their onset values at $q = 0.1 \text{ \AA}^{-1}$: $\omega_p = 0.947 \text{ eV}$ (2H-NbS₂), $\omega_p = 1.095 \text{ eV}$ (2H-TaS₂), $\omega_p = 0.875 \text{ eV}$ (2H-NbSe₂) and $\omega_p = 1.024 \text{ eV}$ (2H-TaSe₂). The data for 2H-NbS₂ are reproduced from [203].

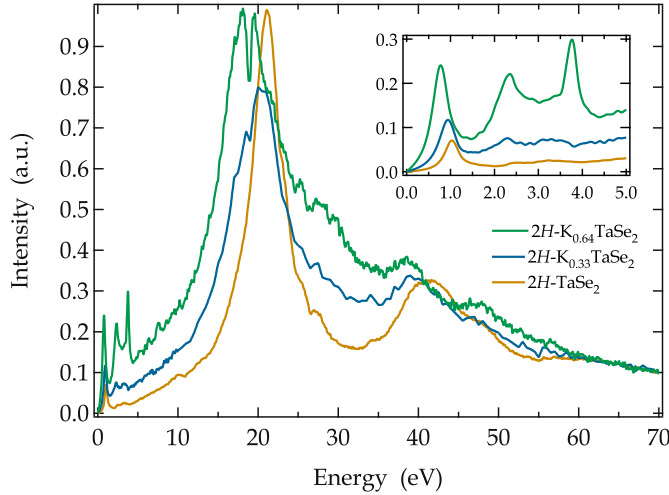


FIGURE 4.14.: The influence of potassium intercalation on the EELS signal. The doping concentration x is derived with the help of Eq. 4.2. The inset shows a close up view of the plasmon region. The sharp peak at about 4 eV corresponds to a K plasmon [25].

n_0 the half filling—corresponding to the plain system—leads to the highest plasmon frequency as shifting the chemical potential by adding either electrons or holes will lower the effective number of charges by filling or emptying pockets of the FERMI surface. The resulting plasma energy was shown to be given by

$$\omega_p^2 = \frac{4\pi n e^2}{m^* \epsilon_\infty} \left(1 - \frac{n}{n_0}\right), \quad (4.2)$$

4. EELS On Transition-Metal Dichalcogenides

which has a maximum for $n/n_0 = 0.5$. Under the precondition that the only parameter that changes upon doping is the density it is therefore possible to estimate the density and from this the doping concentration only by knowing the plasma frequency. Assuming a free-electron mass and that each potassium atom donates exactly one electron to the host one can derive doping values as high as $x \sim 0.8$ in the $2H-K_xTaS_2$ system. Note that according to this scenario for $x = 1$ the d_{z^2} band is completely filled and the system would then be insulating. Similar high numbers could be reached also in the $2H-K_xTaSe_2$ system. In principle one could cross-check this estimate by measuring the raising intensity of the potassium core edges and relate them to those of the transition metals. However, the high bandwidth of the unoccupied states in the dichalcogenides smears out the transition-metal edges the result being only poorly defined features. Therefore one has to rely on the estimates based on the density. Earlier photoemission investigations [206] employing sodium and cesium evaporation deduced $x_{Na} = 0.3$ and failed to extract a value for Cs. How reliable estimates from photoemission are for the EELS remains unclear because the former is a surface-sensitive technique and the concentration on the surface does not necessarily correspond to the bulk value. It might well be that the surface saturates at $x = 0.3$ but the bulk can host more potassium especially as the presence of a potassium plasmon in Fig. 4.15 signals a substantial alkali content inside the lattice.

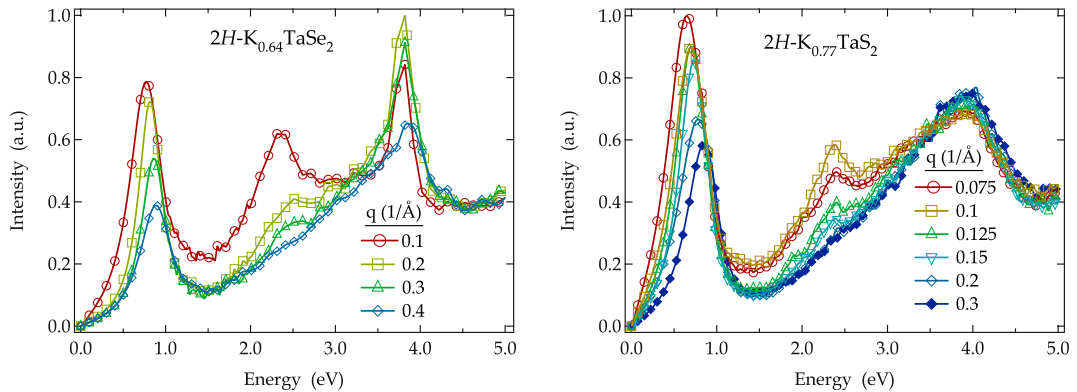


FIGURE 4.15.: The momentum dependence of potassium intercalated $2H-TaSe_2$ and $2H-TaS_2$. The spectra have been corrected for the elastic line according to Eq. 4.1 and are normalized on the high-energy side. Note the blue-shift of the plasmon peak that contrasts the behavior for the undoped compounds (Fig. 4.13 and Fig. 4.11)

The momentum dependence of the intercalated compounds is shown in Fig. 4.15. In remarkable contrast to the behavior reported in Fig. 4.13 and Fig. 4.11 the plasmon dispersion changed its slope after the intercalation. It is even possible to adjust the

value of the plasmon dispersion by suitably changing the potassium content as can be seen from Fig. 4.16.

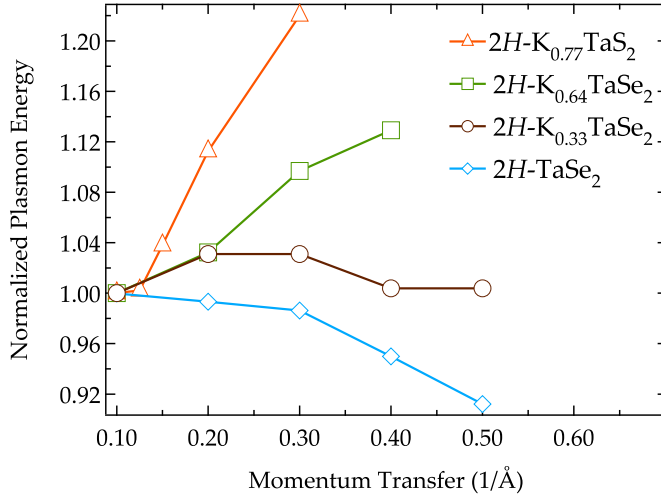


FIGURE 4.16.: The plasmon dispersion for different values of potassium intercalation normalized to their onset values at $q = 0.1 \text{ \AA}^{-1}$. The plain values are: $\omega_p = 1.02 \text{ eV}$ ($2H\text{-TaSe}_2$), $\omega_p = 0.93 \text{ eV}$ ($2H\text{-K}_{0.33}\text{TaSe}_2$), $\omega_p = 0.78 \text{ eV}$ ($2H\text{-K}_{0.64}\text{TaSe}_2$), $\omega_p = 0.65 \text{ eV}$ ($2H\text{-K}_{0.77}\text{TaS}_2$). Note the changing slope for increasing potassium content.

With the above mentioned observation of an intercalation-suppressed CDW order, one may consider the switching of the plasmon dispersion as supporting the notion of the interference of the CDW order with the plasmon. Though this is a potentially quite interesting idea, it is rather unlikely. First, the observed negative plasmon velocity in the plain compounds does not change much upon entering the ordered state and if one assumes that for $T < T_{\text{CDW}}$ a substantial part of the charges enter the CDW condensate then one would actually expect a downshift of the plasmon peak when crossing the phase transition due to a lowering of the number of the charges. While this effect is certainly at work it is obviously only of minor importance and it contradicts the above given observation of an enhancement of the plasmon energy due to the reorganized band structure which overcompensates the lowered electron density. Another point concerns the smallness of the gaps that open on the FERMİ surface. They are on the order of $50 \dots 100 \text{ meV}$ [167, 188, 207] and hence much smaller than the energy scale of the plasmon. As a consequence one would expect this low energy scale to be irrelevant for the collective mode (see also Eq. 2.17). This is also corroborated by the observation that the appearance of the CDW order, though leading to a substantial redistribution of the charges on the FERMİ level, hardly influences the plasmon behavior. In addition the FERMİ surfaces of $2H\text{-NbSe}_2$ and $2H\text{-TaSe}_2$ are not identical but the plasmon shows

4. EELS On Transition-Metal Dichalcogenides

virtually the same behavior. We therefore conclude that the plasmon dispersion is not caused by the CDW order. Moreover from the doping dependent spectra showing that doping immediately triggers a switching of the plasmon velocity, the deviating behavior for $2H\text{-NbS}_2$ is maybe purely accidental, in that the crystals employed for the investigations in Ref. 203 were perhaps non-stoichiometric. This is underlined by the instability of this compound during the growth process[†] also forming the reason why it was not possible to simply investigate $2H\text{-NbS}_2$ again. Finally, if the CDW order is able to interfere with the plasmon dispersion then one can naturally expect this to be observed even better in quasi 1D systems where the instability to form density order is much stronger (see Fig. 2.4). The experimental situation is, however ambiguous in that the blue bronze $\text{K}_{0.3}\text{MoO}_3$ which is known to undergo a PEIERLS transition [208] shows a positive plasmon slope [209] in the vicinity of the BRILLOUIN zone-center. In the organic charge-transfer salt TTF-TCNQ that also shows density ordering [210] there is admittedly a negative plasmon dispersion [211] but this was explained with correlation effects [212].

We take all this as evidence for the negative dispersion being a general feature of the pure dichalcogenides—most likely not driven by the CDW order—and are left with the question, how to reconcile it as this forms an interesting subject in itself.

To this end it is worthwhile to check if a negative plasmon dispersion has ever been observed before and if so, how the effect which strongly contradicts the generic behavior expected from the RPA was explained then. Indeed a negative plasmon velocity was found in elemental Cs [213, 214]. This observation triggered a lot of theoretical efforts as the alkali metals were initially believed to be nature's closest realization of a free electron gas. As the deviations from the RPA prediction are gradually enhanced for the heavier alkali metals with Cs having the largest WIGNER-SEITZ radius of $r_s = 5.62$ it was initially believed that the discrepancies are caused by the increasing importance of electron correlations. Those effects are incorporated in the dielectric function via a static [44] or dynamic [215] local-field correction $G(\mathbf{q}, \omega)$

$$\epsilon(\mathbf{q}, \omega) = 1 - \frac{v_q \chi^0(\mathbf{q}, \omega)}{1 + v_q G(\mathbf{q}, \omega) \chi^0(\mathbf{q}, \omega)}$$

which effectively reduces the coefficient of the quadratic term in the plasmon dispersion (Eq. 2.15, see also the remarks in Sect. 2.4.2). With this at hand it was possible to obtain a better quantitative agreement between theoretical predictions and the experimental plasmon data of the heavy alkali metals but no qualitative one, i. e., inclusion of correlations indeed lowered the plasmon bandwidth but it was not possible to change the sign of the plasmon velocity. Note, that in principle strong enough interactions

[†]H. BERGER, EPFL Lausanne, private communication

can give rise to a negative dispersion in classical plasmas [216, 217]. However, the r_s values required to achieve this are already in the range required for the formation of a WIGNER crystal and the clearly metallic features in the $2H$ -compounds rules out this as a possible reason for the negative dispersion. To make a long story short the Cs problem was finally settled to be more easily understood as an effect of the single-particle band structure as was shown in Ref. 218. By increasing the atomic number in the first row of the periodic table the unoccupied d -orbitals move closer to the FERMI level which opens up new excitation channels for interband transitions in the energy range above the plasma frequency. Due to the momentum dependence of the EELS matrix elements [219] these optically ($q = 0$) forbidden s - d transitions become accessible and gain more and more spectral weight for increasing values of momentum. Then, if one truncates the expansion of $\epsilon_1(\omega)$ in the vicinity of the plasmon already after the linear term

$$\epsilon_1(\omega) = \beta(\omega - \omega_p) \quad \beta = \left(\frac{d\epsilon_1}{d\omega} \right)_{\omega_p} > 0,$$

it is clear that additional interband transitions will lower the zero-crossing of ϵ_1 proportional to $\delta\epsilon_1/\beta$ where $\delta\epsilon_1$ contains the influence of the higher lying contributions. Similar, though in details differing conclusions concerning the importance of interband transitions were also obtained by the authors of Ref. 220.

To see whether a comparable effect is at work to explain the dispersion in the $2H$ -compounds one has to refer to the single particle density of states which is provided by Fig. 4.17. One can clearly see dominant contributions from the transition metal at the FERMI level. Possible interband transitions for $q \rightarrow 0$ lying above the plasmon energy are between the chalcogen p and the transition-metal d -states. This corresponds to the increasing EELS intensity for $\omega > \omega_p$ (see Fig. 4.7 and Fig. 4.11). For non-zero values of momentum there is obviously also a potentially rather large phase-space for transitions within the d -manifold. This is then in close analogy to the Cs case. The behavior reported in Fig. 4.17 further emphasizes the close similarity between $2H$ -TaSe₂ and $2H$ -NbS₂ and this provides further evidence that the different plasmon behavior shown in Fig. 4.13 is probably not intrinsic.

Besides interband transitions lying above the plasma edge, the band structure [194, 223, 224] in principle allows also excitations below the plasmon energy that are potentially hidden in the EELS signal due to a non-sufficient energy resolution and/or the appearance of the elastic line below the plasmon peak. From the optical data on $2H$ -TaSe₂ and $2H$ -NbSe₂ [170, 225, 226] there is indeed—though weak—evidence for an additional contribution below 1 eV which has to become weaker upon increasing momentum transfer in order to pull down the plasmon peak in the loss function. This is in line with the rather large values of the FERMI velocities of the involved bands

4. EELS On Transition-Metal Dichalcogenides

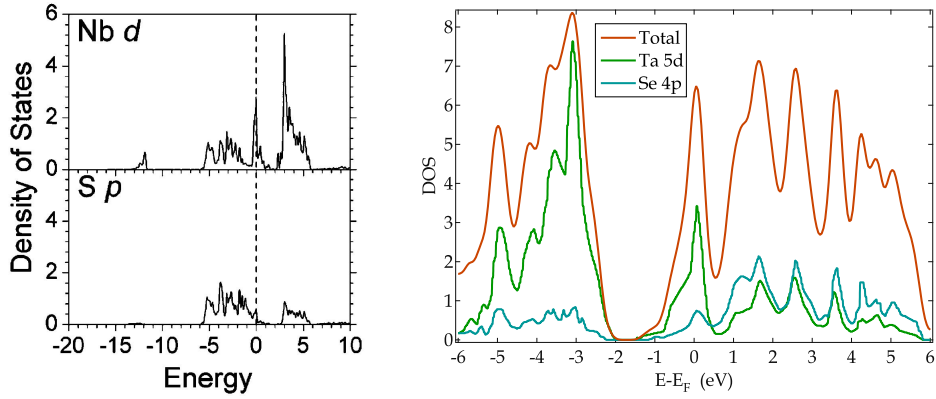


FIGURE 4.17.: The orbital projected density of states (DOS) for $2H\text{-NbS}_2$ (left panel) taken from Ref. 221 and for $2H\text{-TaSe}_2$ reproduced from Ref. 222.

within the hexagonal plane which indeed should lead to a decreasing spectral weight for the interband contribution for higher momenta. Apparently this contradicts the increasing intensity on the low-energy side of the plasmon when leaving the center of the BRILLOUIN ZONE (see , e. g., Fig. 4.7). Furthermore, the interband contribution appears weaker in $2H\text{-NbSe}_2$ but the plasmon shows essentially the same behavior and upon entering the CDW ordered state, the optical spectra [170, 225, 226] and also the transport data (see Fig. 4.4) all congruently show that below the phase transition the metallic character is strongly enhanced. This lowers the possible influence of additional contributions in the infrared. But even with this possibly diminished role of single-particle excitations, the plasmon still shows its negative dispersion (see Fig. 4.9 where the bandwidth is even larger in the ordered state) hindering a straightforward interpretation of the plasmon behavior in terms of interband transitions.

Except for the possible role of interband transitions on the plasmon dispersion there is, however, another factor arising from the single-particle band structure that may drive the plasmon dispersion which stayed widely unrecognized for the alkali metals. The authors of Ref. 227 could show that already *intraband* transitions alone are able to influence the plasmon in such a way as to soften upon increasing momentum transfer. They could prove that the coefficient α in front of the quadratic term of the plasmon dispersion (see Eq. 2.15) actually consists of two contributions. While the first one coincides with the expression given in Eq. 2.15 and is always positive, the second is much more complicated. For a single isotropic band it reads

$$\alpha_2 \sim \frac{k_F}{\omega_p} \operatorname{sgn} \left(\frac{dE(k)}{dk} \right)_{k=k_F} \left[\frac{\partial}{\partial(\ln k)} \operatorname{Tr} \left(m_0 \frac{\partial^2 E(k)}{\partial k_i \partial k_j} \right) \right]_{k=k_F} .$$

This rather cumbersome expression obviously vanishes only in the case of a spherical FERMI surface where the curvature or the effective mass is constant. But the weak deviations from the $E(k) = k^2$ behavior present in the alkali metals are already strong enough to make this term dominating the positive one [227]. Although the (in principle known) tight-binding geometry for the dichalcogenides [228] would allow an evaluation of the above given relation for α_2 the situation is even more complicated. The FERMI surface for $2H$ -TaSe₂ and $2H$ -NbSe₂ contains several sheets originating from different bands and forming electron- as well as hole-like pockets. It is neither clear how to augment the above given relation to incorporate the presence of several bands on the FERMI level nor what additional momentum dependence the matrix elements mediating the transitions between those bands (see also Eq. 2.16) may induce. This makes the whole problem highly non-trivial as in principle a knowledge of the FERMI surface and the wavefunctions is required in order to judge on the significance of these effects. Given that the importance of this second term was also shown for other systems with a simpler FERMI surface topology [133, 209, 229] it is easily conceivable that they cannot be neglected for the dichalcogenides in particular due to the presence of saddle-points in the band structure [189] which should make the role of the conduction-band curvature an even more serious one according to Ref. 227.

There is in principle room for more speculations on the possible origin of the peculiar plasmon behavior which involve, however, more exotic explanations. In general the collective mode spectrum can be expected to be more complex than just the simple optical plasmon mode of a homogeneous 3D electron gas. As first discussed by PINES [230] a solid containing two electronic subsystems with different masses can host an additional acoustic branch in the plasmon spectrum. In analogy with the case of phonons the acoustic and optical mode correspond to the in- and out-of phase oscillation of the two components. This situation is in principle realized in the dichalcogenides by the presence of several FERMI surface sheets originating from two different bands [167]. A similar effect is triggered by the bilayer nature of the unit cell which also allows for the presence of an additional acoustic mode [231].

The result of this could be a highly complicated collective mode spectrum with a possible interference of the optical and acoustic branch. But this is probably not the reason for the negative plasmon dispersion. The necessary condition for the appearance of the two-band related acoustic mode is a large difference in the mean squared velocity and density of the different bands [230] which is not observed in the photoemission data—showing similar FERMI velocities and pocket sizes—ruling out this effect. The bilayer-related acoustic branch possibly exists and one could in principle investigate its role by measuring the plasmon dispersion of the $1T$ modification. But as it turns out the plasma frequency of them is much lower [232] possibly due to the smaller

4. EELS On Transition-Metal Dichalcogenides

FERMI surface pockets [233] and therefore below the accessible limit of the EELS set by the width of the elastic line. Such a mode should, however, be observable also in other bilayer system like $\text{Bi}_2\text{Sr}_2\text{CaCu}_2\text{O}_{8+\delta}$ where there is no evidence for it playing a substantial role in the understanding of the plasmon dynamics. Moreover the positive slope of the acoustic mode should shift the optical one—which is observed in the EELS—to higher energies and not to smaller ones contradicting the findings reported above.

Finally, the layering of the dichalcogenides certainly calls for a proper consideration of crystal local field effects. Again this provides a very ambitious task as it requires in principle to solve Eq. 2.16 which in turn needs the whole electronic structure (wavefunctions and eigenvalues) as input parameters. Moreover it is not clear why other layered systems—like the cuprates discussed above—which are certainly similarly inhomogeneous, do not show such a peculiar negative plasmon velocity.

In summary, a possible influence of the CDW order on the plasmon dispersion is rather unlikely. This also holds for other more unconventional explanations in terms of acoustic modes. At present the interference of single-particle excitations with the plasmon seems to be the most reasonable explanation for its subtleties described above, although it is hard to judge on their importance without a more detailed theoretical and experimental understanding. In particular the “switching” of the plasmon with doping may be reconciled by this idea. In a rigid band model the additional electrons provided by the potassium intercalation fill the hole pockets around the Γ point thereby reducing the phase space for band-to-band transitions.

4.4. Possible Relation To Pnictides

It was explained above that there are numerous ideas how to reconcile the tendency of the chalcogenides to form CDWs and the lack of a generally accepted consensus may one allow to add another possible scenario. To this end we will briefly discuss the recently discovered [171] iron-based pnictide superconductors and in particular the theoretical model suggested by SAWATZKY and co-workers [234, 235].

The main ingredient of the mentioned approach is the large polarizability α of the anions (As, P, Se) in the pnictide lattice, i. e., the ease for electrical fields to induce charge inhomogeneities in their atomic shells. This ansatz can provide an explanation of the unexpectedly small value of the HUBBARD U that can be inferred from the good agreement between the photoemission signal and the predictions based on the local-density approximation [236]. It was even argued that U is smaller than the bandwidth [237], putting the pnictides in an at most weakly correlated regime. From this one can expect that the relationship between them and the cuprates is probably smaller than

4.4. Possible Relation To Pnictides

initially predicted as for the latter there is consensus on U being the, by far, largest energy scale involved.

The conventional definition for the HUBBARD interaction in terms of the ionization energy E_I and the electron affinity E_A reads

$$\begin{aligned} U_0 &= E_I - E_A \\ &= E(N) - E(N-1) - (E(N+1) - E(N-1)) \\ &= E(N+1) + E(N-1) - 2E(N), \end{aligned}$$

where E is the energy of the system containing the number of particles given in parenthesis. The ionization energy describing the willingness of a system to release an electron is, in a strongly polarizable medium mostly determined by the surrounding heavily interfering with the energetics on the ionized site. This is in analogy to the case of the solvation of, say, ionic salts in water and for the case of a solid the anions may therefore be regarded as the “solvent”. With this the electron-electron interaction becomes renormalized by nearest-neighbor point-charge interactions according to

$$U = U_0 - 2E_p \quad \text{with} \quad E_p \sim \sum_i \alpha_i E_i^2 = \frac{Z\alpha e^2}{2R^4},$$

where E_p is the polarization (or solvation) energy on the anion site, Z the number of polarizable nearest neighbors and R measures the distance from the transition metal to the anion. The additional energy term originates from an electric field E_i , i. e., an additional charge on the transition-metal site. Of course the effect of a polarizable medium does not only affect local physics but has also long-range components which can be captured in a first approximation by a nearest neighbor interaction V that also becomes renormalized from its plain value V_0 to

$$V = V_0 - \frac{1}{2} \sum \alpha [(\mathbf{E}_1^2 + \mathbf{E}_2^2) - E_1^2 - E_2^2] = V_0 - 2\alpha \mathbf{E}_1 \cdot \mathbf{E}_2 = V_0 - \frac{2\alpha e^2 \cos(\theta)}{R^4}.$$

Here the sum runs over the number of arsenic atoms shared by two iron sites and θ measures the Fe-As-Fe bond angle. For $\theta < \pi/2$ as is the case for the pnictides [234] it is clear that this can reduce the nearest-neighbor COULOMB repulsion possibly even providing a mechanism to bind charges into pairs.

In general—with the presence of a band structure inside the solid—the situation is of course more complicated and a microscopic model has to take into account the substantial overlap between the cation and anion states that are known to exist in the pnictides (see , e. g., [238]). Nevertheless, the above described framework is interesting as it potentially leaves its traces in the dynamics of the charge-carriers and it can

4. EELS On Transition-Metal Dichalcogenides

therefore be probed with the help of optical experiments. To see this, it is important to realize that there is a close connection between the polarizability and the dielectric function given, for the case of a cubic lattice, by the CLAUDIUS-MOSOTTI relation [239]

$$\frac{4\pi}{3}n\alpha = \frac{\epsilon_\infty - 1}{\epsilon_\infty + 2},$$

with the electron density n . The background dielectric function ϵ_∞ is a phenomenological parameter that captures the influence of higher-lying electronic transitions, i. e., the reorganization of charges triggered by and acting back on the propagation of the charge carriers in the vicinity of the FERMI level. With this at hand the plasma frequency Eq. 2.10 can be generalized to

$$\Omega_p = \sqrt{\frac{4\pi n e^2}{m \epsilon_\infty}} = \frac{\omega_p}{\sqrt{\epsilon_\infty}},$$

where Ω_p is now the screened plasma frequency. From this it is clear that the polarizability can be derived from an optical spectrum by extracting ϵ_∞ . Indeed there is strong experimental evidence for a prominent role of these effects in the pnictides where values of $\epsilon_\infty = 12 \dots 15$ are reported [240, 241].

So, where is the relation to the dichalcogenides? To this end Fig. 4.18 shows the reflectivity for $2H\text{-TaSe}_2$ and $2H\text{-NbSe}_2$ as derived from a KRAMERS-KRONIG transformation of the EELS intensity compared to a DRUDE-LORENTZ fit with ϵ_∞ taken as an additional fitting parameter.

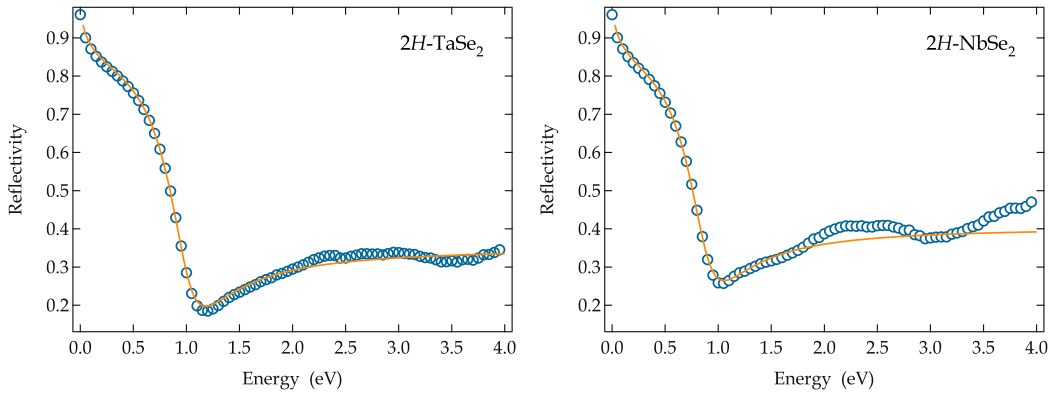


FIGURE 4.18.: The reflectivity obtained from a KRAMERS-KRONIG transformation of the EELS intensity at $q = 0.1 \text{ \AA}^{-1}$ (circles) together with a fit to a DRUDE-LORENTZ model (solid lines). The fitting was extended to $\omega = 2 \text{ eV}$ and the obtained parameters are: $\omega_p = 4.01 \text{ eV}$, $\gamma = 0.4 \text{ eV}$, $\epsilon_\infty \approx 15$ ($2H\text{-TaSe}_2$) and $\omega_p = 4.08 \text{ eV}$, $\gamma = 0.4 \text{ eV}$, $\epsilon_\infty \approx 20$ ($2H\text{-NbSe}_2$)

As can be seen the behavior for both compounds is very similar, which could be expected from the almost identical EELS signal, and in both cases the fitting to a single

4.4. Possible Relation To Pnictides

DRUDE term supplemented by ϵ_∞ provides an excellent description of the low-energy optical response, given the simplicity of the model.

It is the very high value of the background dielectric constant that turns out to be the most remarkable issue behind the fitting as this directly signals the presence of a high polarizability felt by the charges on the FERMI surface (the CLAUSIUS-MOSOTTI relation is steeply rising in the relevant parameter range $\epsilon_\infty = 1 \dots 20$). In particular the strongly pronounced dip at the position of the plasmon peak in the EELS is a clear-cut indication of a strong polarizability felt by the free charges as can be easily deduced from a DRUDE-LORENTZ model. This statement also remains valid if the infrared response consists of more than just the plasma edge (see the discussion above) because electronic transitions below the plasma edge will not produce the dip and the subsequent rise in the reflectivity.

One could of course argue that the plasma frequency is also influenced by the appearance of an effective mass m^* instead of the bare electron mass in the denominator but while this is certainly true it does not allow for an appropriate description of the shape of the reflectivity. We therefore can conclude that it is not a conventional mass-renormalization that softens the plasma frequency from its bare value of $\omega_p = 4 \text{ eV}$ down to the experimentally observable $\Omega_p = 1 \text{ eV}$ but the strong polarization of the charges leads to an object one could possibly call an electronic polaron, in analogy to the pnictides [235].

There is also a structural similarity. Like the FeAs-superconductors two transition-metal ions share two chalcogenide atoms in the $2H$ modification (see Fig. 4.3) with a bond angle of about 83° , again allowing for a reduction of the repulsion between electrons on the transition-metal sites. It is not *a priori* clear why this effect should not be able to favor density ordering, instead of superconductivity. This would then also provide a possible route to reconcile the evidence for substantial many-body effects in the dichalcogenides which were constantly reported in the past: the thermopower deviates from the expectation for an ordinary metal [242], the susceptibility is larger than predicted by band-theory [178] and from tunneling [127, 243, 244], optical [245] and even ARPES [167, 207] investigations it is known that the ratio

$$\frac{2\Delta_{\text{CDW}}}{kT_{\text{CDW}}} \gg 3.53,$$

clearly signaling the importance of strong-coupling phenomena.

Further support for the prominent role of the chalcogenide atoms on the transition-metal behavior comes from recent photoemission results on Ta_2NiSe_5 [246] which also point to a strongly reduced $U = 3 \text{ eV}$ on the Ni site and the decisive influence of a strongly polarizable medium on electronic instabilities. A reliable determination of the HUBBARD U for $2H\text{-TaSe}_2$ and $2H\text{-NbSe}_2$ is therefore desirable although the generally

4. EELS On Transition-Metal Dichalcogenides

good agreement between the band-structure calculations [173] and the observed FERMI surfaces indicates weak correlations although the larger extension of the $4d$ and $5d$ orbitals in Ta and Nb certainly plays a role in this respect.

All this may be taken as evidence for the nesting of the FERMI surface being insufficient to capture all the physics of the dichalcogenides which is also in line with recent theoretical investigations [194, 195] pointing out the fragileness of the criteria for a nesting-driven CDW instability and that they are hardly fulfilled in a real quasi-2D system. This is further corroborated by the observation that different dichalcogenides—in particular $2H$ -TaSe₂, $2H$ -NbSe₂ and $2H$ -NbS₂—show essentially the same nesting vector [228] but $2H$ -NbS₂ does not develop the CDW order (see also Fig. 4.4). In the above mentioned framework this could be related to the observation that the polarizability scales with the volume of the anions and therefore Se²⁻ is more polarizable than S²⁻ [247]. On the other hand Nb has a smaller extension of the d -shell than Ta. Hence, it is conceivable that the polarizability of the sulfur ion is strong enough to “switch on” the CDW order in $2H$ -TaS₂ but the expected higher U value on the Nb site may keep $2H$ -NbS₂ from adopting the charge-ordered state although the nesting criterion is fulfilled. For this it would also be interesting to see whether systems containing the even larger tellurium are stable and show the ordering in the charge channel.

While there are even more analogies between pnictides and chalcogenides like the layered structure, the linear dependence of the resistivity over a broad temperature range [248] and the tendency to form density order [249] one should not forget that there exist also substantial differences: the pnictides have partly much higher T_c values and a proper treatment of the dichalcogenides certainly calls for the inclusion of spin-orbit coupling which is needed to capture particular details of the FERMI surface geometry [224].

Nevertheless one could argue that the simultaneous appearance of density order and superconductivity is ubiquitous in nature, as both are present in the cuprates, pnictides and the dichalcogenides. Cuprates and pnictides certainly have the higher T_c values and one may take this as a hint that magnetism boosts the superconductivity. But the story could also be different. If one takes the close relation between density order and superconductivity as a sign that the corresponding system is in principle willing to adopt one *or* the other ordered state and if the nesting of the FERMI surface is just the—though maybe weak—final breath to favor the density order, what would happen if one were able to make a compound with highly-polarizable atoms without a nested FERMI surface? The result could be a superconductor with *really high* transition temperatures.



A. Properties Of The EELS Electrons

To extend the discussion in Sect. 2.3.1 the aim of this appendix is to calculate the wave vector of the primary electrons in the EELS spectrometer. We start from the relativistic conservation of energy, given by

$$m(v)c^2 = m_0c^2 + E_0 = \gamma m_0c^2,$$

with the primary energy $E_0 = 172$ keV, m_0 the rest mass of the electrons and c the speed of light. This leads immediately to an expression for the relativistic factor

$$\gamma \equiv \frac{1}{\sqrt{1 - \frac{v^2}{c^2}}} = 1 + \frac{E_0}{m_0c^2},$$

which is necessary to get a connection between the energy of the electrons and their velocity

$$v^2 = c^2 - \frac{m_0^2c^6}{(m_0c^2 + E_0)^2}.$$

On the other hand the 4-vector of the momentum reads

$$p^\mu = \left(\frac{E}{c}, \mathbf{p} \right) = \left(\frac{E}{c}, m\mathbf{v} \right) = \left(\frac{E}{c}, \gamma m_0\mathbf{v} \right) = \left(\frac{\hbar\omega}{c}, \hbar\mathbf{k}_0 \right).$$

So the spatial part of the momentum 4-vector is related to the wave vector to be calculated according to

$$\mathbf{k}_0 = \frac{m_0}{\hbar} \gamma \mathbf{v}.$$

Hence,

$$k_0 = \frac{m_0c}{\hbar} \cdot \left(1 + \frac{E_0}{m_0c^2} \right) \cdot \sqrt{1 - \left(\frac{m_0c^2}{m_0c^2 + E_0} \right)^2}.$$

and inserting all the known quantities

$$\begin{aligned} m_0 &= 512 \frac{\text{keV}}{c^2} \\ E_0 &= 172 \text{ keV} \\ c &= 3 \cdot 10^8 \frac{\text{m}}{\text{s}} \\ \hbar &= 1.054 \cdot 10^{-34} \text{ Js} \end{aligned}$$

justifies the relativistic approach, as

$$\frac{v}{c} \approx 0.66 \quad (\text{A.1})$$

and yields an approximate value for the wave vector

$$k_0 \approx 230 \text{ \AA}^{-1} . \quad (\text{A.2})$$

Bibliography

- [1] P. W. Anderson. *Science* 177 393 (1972).
- [2] P. W. Anderson. *Phys. Rev.* 130 439 (1963).
- [3] H. Eschrig. *The Particle World of Condensed Matter* (Edition am Gutenbergplatz Leipzig, 2005).
- [4] E. Rutherford. *Philos. Mag.* 6 1 (1911).
- [5] G. Ruthemann. *Naturwissenschaften* 29 648 (1941).
- [6] G. Ruthemann. *Naturwissenschaften* 30 145 (1942).
- [7] G. Ruthemann. *Ann. Phys.* 2 113 (1948).
- [8] W. Lang. *Optik* 3 233 (1948).
- [9] R. F. Egerton. *Rep. Prog. Phys.* 72 016502 (2009).
- [10] K. Sturm. *Z. Naturforsch.* 48a 233 (1993).
- [11] P. M. Platzman and P. A. Wolff. In *Solid State Phys.* (Academic Press, 1973). Suppl. 13.
- [12] S. Ichimaru. *Rev. Mod. Phys.* 54 1017 (1982).
- [13] F. Schwabl. *Advanced quantum mechanics* (Springer, 2005).
- [14] J. M. Ziman. *Elements of advanced quantum theory* (Cambridge University Press, 1992).
- [15] P. Abbamonte, K. D. Finkelstein, M. D. Collins and S. M. Gruner. *Phys. Rev. Lett.* 92 237401 (2004).
- [16] P. Abbamonte, T. Graber, J. P. Reed, S. Smadici, C.-L. Yeh, A. Shukla, J.-P. Rueff and W. Ku. *Proc. Natl. Acad. Sci.* 105 12159 (2008).
- [17] L. Van Hove. *Phys. Rev.* 95 249 (1954).
- [18] R. Kubo. *J. Phys. Soc. Jpn.* 12 570 (1957).
- [19] W. Hanke. *Adv. Phys.* 27 287 (1978).
- [20] H. B. Callen and T. A. Welton. *Phys. Rev.* 83 34 (1951).
- [21] L. D. Landau and E. M. Lifshitz. *Statistical physics* (Pergamon Pr., 1969).
- [22] A. Damascelli, Z. Hussain and Z.-X. Shen. *Rev. Mod. Phys.* 75 473 (2003).
- [23] A. L. Fetter and J. D. Walecka. *Quantum theory of many particle systems* (McGraw-Hill, 1971).
- [24] S. Raimes. *Rep. Prog. Phys.* 20 1 (1957).
- [25] D. Pines. *Elementary Excitations In Solids* (W. A. Benjamin, Inc. N.Y., 1963).
- [26] D. Pines and P. Nozières. *Theory of Quantum Liquids* (W. A. Benjamin, Inc. N.Y., 1966).
- [27] P. Ziesche and G. Paasch. *Ergebnisse in der Elektronentheorie der Metalle*, chapter Das Elektronengas, p. 14 (Akademie Verlag, 1983).
- [28] V. D. Gorobchenko, V. N. Kohn and E. G. Maksimov. *The Dielectric Function of Condensed Systems*, chapter The Dielectric Function of the Homogeneous Electron Gas, p. 87. *Modern Problems In Condensed Matter Sciences* (Elsevier, 1989).
- [29] W. Nolting. *Viel-Teilchen-Theorie* (Springer, 2002).

- [30] L. Tonks and I. Langmuir. *Phys. Rev.* 33 195 (1929).
- [31] D. Pines and D. Bohm. *Phys. Rev.* 85 338 (1952).
- [32] D. Pines. *Rev. Mod. Phys.* 28 184 (1956).
- [33] J. Lindhard. *Kgl. Danske Videnskab. Selskab, Mat.-fys. Medd.* 28 1 (1954).
- [34] W. Gasser, E. Heiner and K. Elk. *Greensche Funktionen in Festkörper- und Vielteilchenphysik* (Wiley-VCH, 2001).
- [35] M. Dressel and G. Grüner. *Electrodynamics Of Solids* (Cambridge University Press, 2003).
- [36] O. V. Dolgov, D. A. Kirzhnits and E. G. Maksimov. *Rev. Mod. Phys.* 53 81 (1981).
- [37] D. A. Kirshnitz. *High-Temperature Superconductivity*, chapter The Critical Temperture of a Superconducting System, p. 41 (Consultants Bureau, 1982).
- [38] P. W. Anderson. *Science* 316 1705 (2007).
- [39] E. G. Maksimov and O. V. Dolgov. *Phys. Usp.* 50 933 (2007).
- [40] G. Grüner. *Density Waves In Solids* (Addison-Wesley, 1994).
- [41] R. E. Peierls. *Quantum Theory Of Solids* (Oxford University Press, 1956).
- [42] W. Kohn. *Phys. Rev. Lett.* 2 393 (1959).
- [43] K. Sturm. *Adv. Phys.* 31 1 (1982).
- [44] K. S. Singwi, M. P. Tosi, R. H. Land and A. Sjölander. *Phys. Rev.* 176 589 (1968).
- [45] H. Ehrenreich and M. H. Cohen. *Phys. Rev.* 115 786 (1959).
- [46] S. L. Adler. *Phys. Rev.* 126 413 (1962).
- [47] N. Wiser. *Phys. Rev.* 129 62 (1963).
- [48] G. Onida, L. Reining and A. Rubio. *Rev. Mod. Phys.* 74 601 (2002).
- [49] S. R. Nagel and T. A. Witten. *Phys. Rev. B* 11 1623 (1975).
- [50] F. Wooten. *Optical Properties Of Solids* (Academic Press, 1972).
- [51] D. N. Basov and T. Timusk. *Rev. Mod. Phys.* 77 721 (2005).
- [52] J. Fink. *Adv. Electron. Electron Phys.* 75 121 (1989).
- [53] N. Nücker, J. Fink, J. C. Fuggle, P. J. Durham and W. M. Temmerman. *Phys. Rev. B* 37 5158 (1988).
- [54] J. Fink, M. Knupfer, S. Atzkern and M. S. Golden. *J. Electron Spectrosc. Relat. Phenom.* 117-118 287 (2001).
- [55] J. G. Bednorz and K. A. Müller. *Z. Phys. B* 64 189 (1986).
- [56] T. Dahm, V. Hinkov, S. V. Borisenko, A. A. Kordyuk, V. B. Zabolotnyy, J. Fink, B. Buchner, D. J. Scalapino, W. Hanke and B. Keimer. *Nat Phys* 5 217 (2009).
- [57] P. Monthoux, D. Pines and G. G. Lonzarich. *Nature* 450 1177 (2007).
- [58] E. G. Maksimov, M. L. Kulić and O. V. Dolgov. Bosonic spectral function and the electron-phonon interaction in htsc cuprates (2010). ArXiv:1001.4859.
- [59] E. A. Pashitskiĭ and V. I. Pentegov. *Low. Temp. Phys.* 27 103 (2001).
- [60] W. E. Pickett. *Rev. Mod. Phys.* 61 433 (1989).
- [61] E. Dagotto. *Rev. Mod. Phys.* 66 763 (1994).
- [62] W. Brenig. *Phys. Rep.* 251 153 (1995).
- [63] J. Orenstein and A. J. Millis. *Science* 288 468 (2000).

- [64] Z. Hiroi, N. Kobayashi and M. Takano. *Nature* 371 139 (1994).
- [65] Y. Kohsaka, M. Azuma, I. Yamada, T. Sasagawa, T. Hanaguri, M. Takano and H. Takagi. *J. Am. Chem. Soc.* 124 12275 (2002).
- [66] P. Fulde. *Electron Correlations in Molecules and Solids*. Springer Series in Solid-State Sciences (Springer, 1993).
- [67] H. Takagi, B. Batlogg, H. L. Kao, J. Kwo, R. J. Cava, J. J. Krajewski and W. F. Peck. *Phys. Rev. Lett.* 69 2975 (1992).
- [68] G. Shirane, Y. Endoh, R. J. Birgeneau, M. A. Kastner, Y. Hidaka, M. Oda, M. Suzuki and T. Murakami. *Phys. Rev. Lett.* 59 1613 (1987).
- [69] N. F. Mott. *Proc. Phys. Soc. A* 62 416 (1949).
- [70] A. Georges, G. Kotliar, W. Krauth and M. J. Rozenberg. *Rev. Mod. Phys.* 68 13 (1996).
- [71] M. J. Rozenberg, G. Kotliar, H. Kajueter, G. A. Thomas, D. H. Rapkine, J. M. Honig and P. Metcalf. *Phys. Rev. Lett.* 75 105 (1995).
- [72] M. J. Rozenberg, G. Kotliar and H. Kajueter. *Phys. Rev. B* 54 8452 (1996).
- [73] A. Comanac, L. de' Medici, M. Capone and A. J. Millis. *Nat Phys* 4 287 (2008).
- [74] P. Fazekas. *Lecture Notes on Electron Correlation and Magnetism* (World Scientific, 1999).
- [75] P. W. Anderson. *Science* 235 1196 (1987).
- [76] V. J. Emery. *Phys. Rev. Lett.* 58 2794 (1987).
- [77] F. C. Zhang and T. M. Rice. *Phys. Rev. B* 37 3759 (1988).
- [78] Y. Endoh, K. Yamada, R. J. Birgeneau, D. R. Gabbe, H. P. Jenssen, M. A. Kastner, C. J. Peters, P. J. Picone, T. R. Thurston, J. M. Tranquada, G. Shirane, Y. Hidaka, M. Oda, Y. Enomoto, M. Suzuki and T. Murakami. *Phys. Rev. B* 37 7443 (1988).
- [79] B. Keimer, N. Belk, R. J. Birgeneau, A. Cassanho, C. Y. Chen, M. Greven, M. A. Kastner, A. Aharony, Y. Endoh, R. W. Erwin and G. Shirane. *Phys. Rev. B* 46 14034 (1992).
- [80] L. N. Bulaevskii, E. L. Nagaev and D. I. Khomskii. *Sov. Phys JETP* 27 836 (1968).
- [81] W. F. Brinkman and T. M. Rice. *Phys. Rev. B* 2 1324 (1970).
- [82] C. L. Kane, P. A. Lee and N. Read. *Phys. Rev. B* 39 6880 (1989).
- [83] B. O. Wells, Z. X. Shen, A. Matsuura, D. M. King, M. A. Kastner, M. Greven and R. J. Birgeneau. *Phys. Rev. Lett.* 74 964 (1995).
- [84] R. B. Laughlin. *J. Phys. Chem. Solids* 56 1627 (1995).
- [85] T. Timusk and B. Statt. *Rep. Prog. Phys.* 62 61 (1999).
- [86] M. V. Sadovskii. *Phys. Usp.* 44 515 (2001).
- [87] M. R. Norman, D. Pines and C. Kallin. *Adv. Phys.* 54 715 (2005).
- [88] J. M. Tranquada, B. J. Sternlieb, J. D. Axe, Y. Nakamura and S. Uchida. *Nature* 375 561 (1995).
- [89] S. A. Kivelson, I. P. Bindloss, E. Fradkin, V. Oganessian, J. M. Tranquada, A. Kapitulnik and C. Howald. *Rev. Mod. Phys.* 75 1201 (2003).
- [90] M. Vojta. *Adv. Phys.* 58 699 (2009).
- [91] A. R. Moodenbaugh, Y. Xu, M. Suenaga, T. J. Folkerts and R. N. Shelton. *Phys. Rev. B* 38 4596 (1988).
- [92] M. Vojta, T. Vojta and R. K. Kaul. *Phys. Rev. Lett.* 97 097001 (2006).
- [93] S. Uchida, T. Ido, H. Takagi, T. Arima, Y. Tokura and S. Tajima. *Phys. Rev. B* 43 7942 (1991).

- [94] S. L. Cooper, D. Reznik, A. Kotz, M. A. Karlow, R. Liu, M. V. Klein, W. C. Lee, J. Giapintzakis, D. M. Ginsberg, B. W. Veal and A. P. Paulikas. *Phys. Rev. B* 47 8233 (1993).
- [95] C. C. Tsuei and J. R. Kirtley. *Rev. Mod. Phys.* 72 969 (2000).
- [96] A. Kanigel, M. R. Norman, M. Randeria, U. Chatterjee, S. Souma, A. Kaminski, H. M. Fretwell, S. Rosenkranz, M. Shi, T. Sato, T. Takahashi, Z. Z. Li, H. Raffy, K. Kadowaki, D. Hinks, L. Ozyuzer and J. C. Campuzano. *Nat Phys* 2 447 (2006).
- [97] W. S. Lee, I. M. Vishik, K. Tanaka, D. H. Lu, T. Sasagawa, N. Nagaosa, T. P. Devereaux, Z. Hussain and Z.-X. Shen. *Nature* 450 81 (2007).
- [98] M. R. Norman, H. Ding, M. Randeria, J. C. Campuzano, T. Yokoya, T. Takeuchi, T. Takahashi, T. Mochiku, K. Kadowaki, P. Guptasarma and D. G. Hinks. *Nature* 392 157 (1998).
- [99] S. Hühfner, M. A. Hossain, A. Damascelli and G. A. Sawatzky. *Rep. Prog. Phys.* 71 062501 (2008).
- [100] N. Doiron-Leyraud, C. Proust, D. LeBoeuf, J. Levallois, J.-B. Bonnemaïson, R. Liang, D. A. Bonn, W. N. Hardy and L. Taillefer. *Nature* 447 565 (2007).
- [101] D. LeBoeuf, N. Doiron-Leyraud, J. Levallois, R. Daou, J.-B. Bonnemaïson, N. E. Hussey, L. Balicas, B. J. Ramshaw, R. Liang, D. A. Bonn, W. N. Hardy, S. Adachi, C. Proust and L. Taillefer. *Nature* 450 533 (2007).
- [102] R. Neudert, T. Böske, O. Knauff, M. Knupfer, M. S. Golden, G. Krabbes, J. Fink, H. Eisaki and S. Uchida. *Physica B: Condensed Matter* 230-232 847 (1997).
- [103] R. Neudert. *Elektronische Korrelationen in niederdimensionalen Kupraten*. Dissertation, Technische Universität Dresden (1999).
- [104] A. Zibold, H. L. Liu, S. W. Moore, J. M. Graybeal and D. B. Tanner. *Phys. Rev. B* 53 11734 (1996).
- [105] H. S. Choi, Y. S. Lee, T. W. Noh, E. J. Choi, Y. Bang and Y. J. Kim. *Phys. Rev. B* 60 4646 (1999).
- [106] J. P. Falck, A. Levy, M. A. Kastner and R. J. Birgeneau. *Phys. Rev. Lett.* 69 1109 (1992).
- [107] M. E. Simón, A. A. Aligia, C. D. Batista, E. R. Gagliano and F. Lema. *Phys. Rev. B* 54 R3780 (1996).
- [108] F. C. Zhang and K. K. Ng. *Phys. Rev. B* 58 13520 (1998).
- [109] A. S. Moskvin, R. Neudert, M. Knupfer, J. Fink and R. Hayn. *Phys. Rev. B* 65 180512 (2002).
- [110] H. Kishida, M. Ono, K. Miura, H. Okamoto, M. Izumi, T. Manako, M. Kawasaki, Y. Taguchi, Y. Tokura, T. Tohyama, K. Tsutsui and S. Maekawa. *Phys. Rev. Lett.* 87 177401 (2001).
- [111] T. Manako, Y. Okimoto, M. Izumi, S. Shinomori, M. Kawasaki, H. Kishida, H. Okamoto, T. Fukumura, M. Ohtani and Y. Tokura. *Appl. Phys. Lett.* 79 1754 (2001).
- [112] K. W. Kim and G. D. Gu. *Phys. Rev. B* 79 085121 (2009).
- [113] N. Lin, E. Gull and A. J. Millis. *Phys. Rev. B* 80 161105 (2009).
- [114] S. Nakajima, Y. Toyozawa and R. Abe. *The Physics of Elementary Excitations*. Springer Series in Solid-State Sciences (Springer, 1980).
- [115] F. H. L. Essler, F. Gebhard and E. Jeckelmann. *Phys. Rev. B* 64 125119 (2001).
- [116] M. Ono, K. Miura, A. Maeda, H. Matsuzaki, H. Kishida, Y. Taguchi, Y. Tokura, M. Yamashita and H. Okamoto. *Phys. Rev. B* 70 085101 (2004).
- [117] R. Neudert, M. Knupfer, M. S. Golden, J. Fink, W. Stephan, K. Penc, N. Motoyama, H. Eisaki and S. Uchida. *Phys. Rev. Lett.* 81 657 (1998).
- [118] H. Itoh, A. Takahashi and M. Aihara. *Phys. Rev. B* 73 075110 (2006).

- [119] A. Zibold, L. Widder, H. P. Gesserich, G. Bräuchle, H. Claus, H. v. Löhneysen, N. Nücker, A. Erb and G. Müller-Vogt. *Physica C: Superconductivity* 212 365 (1993).
- [120] K. Waku, T. Katsufuji, Y. Kohsaka, T. Sasagawa, H. Takagi, H. Kishida, H. Okamoto, M. Azuma and M. Takano. *Phys. Rev. B* 70 134501 (2004).
- [121] Y. Y. Wang, F. C. Zhang, V. P. Dravid, K. K. Ng, M. V. Klein, S. E. Schnatterly and L. L. Miller. *Phys. Rev. Lett.* 77 1809 (1996).
- [122] M. Z. Hasan, E. D. Isaacs, Z.-X. Shen, L. L. Miller, K. Tsutsui, T. Tohyama and S. Maekawa. *Science* 288 1811 (2000).
- [123] D. S. Ellis, J. P. Hill, S. Wakimoto, R. J. Birgeneau, D. Casa, T. Gog and Y.-J. Kim. *Phys. Rev. B* 77 060501 (2008).
- [124] P. W. Anderson. *Phys. Rev.* 109 1492 (1958).
- [125] Y. S. Lee, K. Segawa, Z. Q. Li, W. J. Padilla, M. Dumm, S. V. Dordevic, C. C. Homes, Y. Ando and D. N. Basov. *Phys. Rev. B* 72 054529 (2005).
- [126] H. Romberg, N. Nücker, J. Fink, T. Wolf, X. X. Xi, B. Koch, H. P. Gesserich, M. DÄErrler, W. Assmus and B. Gegenheimer. *Z. Phys. B* 78 367 (1990).
- [127] C. Wang, B. Giambattista, C. G. Slough, R. V. Coleman and M. A. Subramanian. *Phys. Rev. B* 42 8890 (1990).
- [128] N. Nücker, U. Eckern, J. Fink and P. Müller. *Phys. Rev. B* 44 7155 (1991).
- [129] M. Knupfer, G. Roth, J. Fink, J. Karpinski and E. Kaldis. *Physica C* 230 121 (1994).
- [130] A. Hauschild. *Plasmonendispersion in $\text{Bi}_2\text{Sr}_{2-x}\text{La}_x\text{CuO}_{6+\delta}$ -Einkristallen*. Diplomarbeit, Universität Hamburg (1999).
- [131] M. Alexander. *Elektronenenergieverlustspektroskopie an n-dotierten Hochtemperatursupraleitern und verwandten Systemen*. Dissertation, Kernforschungszentrum Karlsruhe (1992).
- [132] C. H. Patterson. *Phys. Rev. B* 77 094523 (2008).
- [133] V. G. Grigoryan, G. Paasch and S.-L. Drechsler. *Phys. Rev. B* 60 1340 (1999).
- [134] L. L. Miller, X. L. Wang, S. X. Wang, C. Stassis, D. C. Johnston, J. Faber and C.-K. Loong. *Phys. Rev. B* 41 1921 (1990).
- [135] M. Wagner. *Gruppentheoretische Methoden in der Physik* (Vieweg, 1998).
- [136] L. D. Landau and E. M. Lifshitz. *Electrodynamics of continuous media* (Pergamon Pr., 1984).
- [137] H. Raether. *Excitation of plasmons and interband transitions by electrons* (Springer, 1980).
- [138] T. Hanaguri, C. Lupien, Y. Kohsaka, D.-H. Lee, M. Azuma, M. Takano, H. Takagi and J. C. Davis. *Nature* 430 1001 (2004).
- [139] Ş. Smadici, P. Abbamonte, M. Taguchi, Y. Kohsaka, T. Sasagawa, M. Azuma, M. Takano and H. Takagi. *Phys. Rev. B* 75 075104 (2007).
- [140] S. E. Brown, E. Fradkin and S. A. Kivelson. *Phys. Rev. B* 71 224512 (2005).
- [141] Y. Kohsaka, C. Taylor, K. Fujita, A. Schmidt, C. Lupien, T. Hanaguri, M. Azuma, M. Takano, H. Eisaki, H. Takagi, S. Uchida and J. C. Davis. *Science* 315 1380 (2007).
- [142] M. Vojta and O. Rösch. *Phys. Rev. B* 77 094504 (2008).
- [143] M. Vojta. *Phys. Rev. B* 78 144508 (2008).
- [144] K.-Y. Yang, W.-Q. Chen, T. M. Rice and F.-C. Zhang. *Phys. Rev. B* 80 174505 (2009).
- [145] T. Valla, A. V. Fedorov, J. Lee, J. C. Davis and G. D. Gu. *Science* 314 1914 (2006).

- [146] K. M. Shen, F. Ronning, D. H. Lu, F. Baumberger, N. J. C. Ingle, W. S. Lee, W. Meevasana, Y. Kohsaka, M. Azuma, M. Takano, H. Takagi and Z.-X. Shen. *Science* 307 901 (2005).
- [147] L. Tassini, F. Venturini, Q.-M. Zhang, R. Hackl, N. Kikugawa and T. Fujita. *Phys. Rev. Lett.* 95 117002 (2005).
- [148] S. Wakimoto, H. Kimura, K. Ishii, K. Ikeuchi, T. Adachi, M. Fujita, K. Kakurai, Y. Koike, J. Mizuki, Y. Noda, K. Yamada, A. H. Said and Y. Shvyd'ko. *Phys. Rev. Lett.* 102 157001 (2009).
- [149] Y. Ando, S. Komiya, K. Segawa, S. Ono and Y. Kurita. *Phys. Rev. Lett.* 93 267001 (2004).
- [150] F. Ronning, K. M. Shen, N. P. Armitage, A. Damascelli, D. H. Lu, Z.-X. Shen, L. L. Miller and C. Kim. *Phys. Rev. B* 71 094518 (2005).
- [151] J. Stiebling and H. Raether. *Phys. Rev. Lett.* 40 1293 (1978).
- [152] H. Eskes, M. B. J. Meinders and G. A. Sawatzky. *Phys. Rev. Lett.* 67 1035 (1991).
- [153] M. B. J. Meinders, H. Eskes and G. A. Sawatzky. *Phys. Rev. B* 48 3916 (1993).
- [154] T. Maier, M. Jarrell, T. Pruschke and M. H. Hettler. *Rev. Mod. Phys.* 77 1027 (2005).
- [155] M. Ferrero, P. S. Cornaglia, L. D. Leo, O. Parcollet, G. Kotliar and A. Georges. *Phys. Rev. B* 80 064501 (2009).
- [156] M. Aichhorn, E. Arrigoni, M. Potthoff and W. Hanke. *Phys. Rev. B* 74 024508 (2006).
- [157] W. Y. Liang and S. L. Cundy. *Philos. Mag.* 19 1031 (1969).
- [158] J. A. Wilson and A. D. Yoffe. *Adv. Phys.* 18 193 (1969).
- [159] J. A. Wilson, F. J. Di Salvo and S. Mahajan. *Phys. Rev. Lett.* 32 882 (1974).
- [160] J. A. Wilson, F. D. Salvo and S. Mahajan. *Adv. Phys.* 24 117 (1975).
- [161] W. A. Little. *Phys. Rev.* 134 A1416 (1964).
- [162] V. L. Ginzburg and D. A. Kirshnitz. *High-Temperature Superconductivity* (Consultants Bureau, 1982).
- [163] L. Bulaevskii. *High-Temperature Superconductivity*, chapter Electronic Properties and Superconductivity of Layered Crystals, p. 213 (Consultants Bureau, 1982).
- [164] F. R. Gamble, J. H. Osiecki, M. Cais, R. Pisharody, F. J. DiSalvo and T. H. Geballe. *Science* 174 493 (1971).
- [165] R. H. Friend and A. D. Yoffe. *Adv. Phys.* 36 1 (1987).
- [166] R. A. Klemm. *Physica C: Superconductivity* 341-348 839 (2000).
- [167] S. V. Borisenko, A. A. Kordyuk, A. N. Yaresko, V. B. Zabolotnyy, D. S. Inosov, R. Schuster, B. Büchner, R. Weber, R. Follath, L. Patthey and H. Berger. *Phys. Rev. Lett.* 100 196402 (2008).
- [168] A. A. Kordyuk, S. V. Borisenko, V. B. Zabolotnyy, R. Schuster, D. S. Inosov, D. V. Evtushinsky, A. I. Plyushchay, R. Follath, A. Varykhalov, L. Patthey and H. Berger. *Phys. Rev. B* 79 020504 (2009).
- [169] C. C. Homes, S. V. Dordevic, G. D. Gu, Q. Li, T. Valla and J. M. Tranquada. *Phys. Rev. Lett.* 96 257002 (2006).
- [170] V. Vescoli, L. Degiorgi, H. Berger and L. Forró. *Phys. Rev. Lett.* 81 453 (1998).
- [171] Y. Kamihara, T. Watanabe, M. Hirano and H. Hosono. *J. Am. Chem. Soc.* 130 3296 (2008).
- [172] T. Yokoya, T. Kiss, A. Chainani, S. Shin, M. Nohara and H. Takagi. *Science* 294 2518 (2001).
- [173] G. Wexler and A. M. Woolley. *J. Phys. C.* 9 1185 (1976).
- [174] L. F. Mattheiss. *Phys. Rev. B* 8 3719 (1973).
- [175] H. W. Myron and A. J. Freeman. *Phys. Rev. B* 11 2735 (1975).

- [176] A. M. Woolley and G. Wexler. *J. Phys. C*. 10 2601 (1977).
- [177] Q. Yan-Bin, L. Yan-Ling, Z. Guo-Hua, Z. Zhi and Q. Xiao-Ying. *Chinese Physics* 16 3809 (2007).
- [178] J. A. Wilson. *Phys. Rev. B* 15 5748 (1977).
- [179] M. Naito and S. Tanaka. *J. Phys. Soc. Jpn.* 51 219 (1982).
- [180] A. M. Gabovich, A. I. Voitenko and M. Ausloos. *Phys. Rep.* 367 583 (2002).
- [181] L. Fang, Y. Wang, P. Y. Zou, L. Tang, Z. Xu, H. Chen, C. Dong, L. Shan and H. H. Wen. *Phys. Rev. B* 72 014534 (2005).
- [182] Y. Nozuyama and S. Iida. *Jpn. J. Appl. Phys.* 23 L319 (1984).
- [183] K. E. Wagner, E. Morosan, Y. S. Hor, J. Tao, Y. Zhu, T. Sanders, T. M. McQueen, H. W. Zandbergen, A. J. Williams, D. V. West and R. J. Cava. *Phys. Rev. B* 78 104520 (2008).
- [184] E. Morosan, H. W. Zandbergen, B. S. Dennis, J. W. G. Bos, Y. Onose, T. Klimczuk, A. P. Ramirez, N. P. Ong and R. J. Cava. *Nat Phys* 2 544 (2006).
- [185] H. Cercellier, C. Monney, F. Clerc, C. Battaglia, L. Despont, M. G. Garnier, H. Beck, P. Aebi, L. Patthey, H. Berger and L. Forró. *Phys. Rev. Lett.* 99 146403 (2007).
- [186] W. Kohn. *Phys. Rev. Lett.* 19 439 (1967).
- [187] D. Jérôme, T. M. Rice and W. Kohn. *Phys. Rev.* 158 462 (1967).
- [188] S. V. Borisenko, A. A. Kordyuk, V. B. Zabolotnyy, D. S. Inosov, D. Evtushinsky, B. Büchner, A. N. Yaresko, A. Varykhalov, R. Follath, W. Eberhardt, L. Patthey and H. Berger. *Phys. Rev. Lett.* 102 166402 (2009).
- [189] T. M. Rice and G. K. Scott. *Phys. Rev. Lett.* 35 120 (1975).
- [190] T. Straub, T. Finteis, R. Claessen, P. Steiner, S. Hüfner, P. Blaha, C. S. Oglesby and E. Bucher. *Phys. Rev. Lett.* 82 4504 (1999).
- [191] R. L. Barnett, A. Polkovnikov, E. Demler, W.-G. Yin and W. Ku. *Phys. Rev. Lett.* 96 026406 (2006).
- [192] Z. J. Yao, J. X. Li and Z. D. Wang. *Phys. Rev. B*. 74 212507 (2006).
- [193] A. H. Castro Neto. *Phys. Rev. Lett.* 86 4382 (2001).
- [194] M. D. Johannes, I. I. Mazin and C. A. Howells. *Phys. Rev. B* 73 205102 (2006).
- [195] M. D. Johannes and I. I. Mazin. *Phys. Rev. B* 77 165135 (2008).
- [196] M. G. Bell and W. Y. Liang. *Adv. Phys.* 25 53 (1976).
- [197] R. Schuster, R. Kraus, M. Knupfer, H. Berger and B. Büchner. *Phys. Rev. B* 79 045134 (2009).
- [198] D. E. Moncton, J. D. Axe and F. J. DiSalvo. *Phys. Rev. Lett.* 34 734 (1975).
- [199] D. E. Moncton, J. D. Axe and F. J. DiSalvo. *Phys. Rev. B* 16 801 (1977).
- [200] J. A. Wilson. *Phys. Rev. B* 17 3880 (1978).
- [201] G. Campagnoli, A. Gustinetti, A. Stella and E. Tosatti. *Phys. Rev. B* 20 2217 (1979).
- [202] A. Bianconi, S. Stizza and R. Bernardini. *Phys. Rev. B* 24 4406 (1981).
- [203] R. Manzke, G. Crecelius, J. Fink and R. Schöllhorn. *Solid State Commun.* 40 103 (1981).
- [204] W. Z. Hu, G. Li, J. Yan, H. H. Wen, G. Wu, X. H. Chen and N. L. Wang. *Phys. Rev. B* 76 045103 (2007).
- [205] X. Zhu, Y. Sun, X. Zhu, X. Luo, B. Wang, G. Li, Z. Yang, W. Song and J. Dai. *J. Cryst. Growth* 311 218 (2008).
- [206] H. E. Brauer, H. I. Starnberg, L. J. Holleboom, H. P. Hughes and V. N. Strocov. *J. Phys.: Condens. Matter* 13 9879 (2001).

- [207] K. Rossnagel, E. Rotenberg, H. Koh, N. V. Smith and L. Kipp. *Phys. Rev. B* 72 121103 (2005).
- [208] G. Travaglini, P. Wachter, J. Marcus and C. Schlenker. *Solid State Commun.* 37 599 (1981).
- [209] M. Sing, V. G. Grigoryan, G. Paasch, M. Knupfer, J. Fink, B. Lommel and W. Aßmus. *Phys. Rev. B* 59 5414 (1999).
- [210] F. Denoyer, F. Comès, A. F. Garito and A. J. Heeger. *Phys. Rev. Lett.* 35 445 (1975).
- [211] J. J. Ritsko, D. J. Sandman, A. J. Epstein, P. C. Gibbons, S. E. Schnatterly and J. Fields. *Phys. Rev. Lett.* 34 1330 (1975).
- [212] L. M. Kahn, J. Ruvalds and R. Hastings. *Phys. Rev. B* 17 4600 (1978).
- [213] A. vom Felde, J. Fink, T. Büche, B. Scheerer and N. Nücker. *Europhys. Lett.* 4 1037 (1987).
- [214] A. vom Felde, J. Sprösser-Prou and J. Fink. *Phys. Rev. B* 40 10181 (1989).
- [215] A. Holas and S. Rahman. *Phys. Rev. B* 35 2720 (1987).
- [216] E. L. Pollock and J. P. Hansen. *Phys. Rev. A* 8 3110 (1973).
- [217] M. C. Abramo and M. P. Tosi. *Il Nuovo Cimento B* 21 363 (1974).
- [218] F. Aryasetiawan and K. Karlsson. *Phys. Rev. Lett.* 73 1679 (1994).
- [219] S. E. Schnatterly. In *Solid State Phys.*, volume 34, pp. 275–358 (Academic Press, 1979).
- [220] A. G. Eguiluz and W. Ku. *Electron Correlations and Materials Properties*, chapter Ab Initio Studies Of Electronic Excitations In Real Solids, p. 329 (Kluwer, 1999).
- [221] R. Oviedo-Roa, J.-M. Martínez-Magádan and F. Illas. *J. Phys. Chem. B* 110 7951 (2006).
- [222] A. H. Reshak and S. Auluck. *Physica B-Condensed Matter* 358 158 (2005).
- [223] K. Rossnagel, O. Seifarth, L. Kipp, M. Skibowski, D. Voss, P. Kruger, A. Mazur and J. Pollmann. *Phys. Rev. B* 64 235119 (2001).
- [224] K. Rossnagel and N. V. Smith. *Phys. Rev. B* 76 073102 (2007).
- [225] B. Ruzicka, L. Degiorgi, H. Berger, R. Gaál and L. Forró. *Phys. Rev. Lett.* 86 4136 (2001).
- [226] S. V. Dordevic, D. N. Basov, R. C. Dynes and E. Bucher. *Phys. Rev. B* 64 161103 (2001).
- [227] G. Paasch and V. G. Grigoryan. *Ukr. Fiz. Zhurn.* 44 1480 (1999).
- [228] D. S. Inosov, V. B. Zabolotnyy, D. V. Evtushinsky, A. A. Kordyuk, B. Buchner, R. Follath, H. Berger and S. V. Borisenko. *New J. Phys.* 10 125027 (2008).
- [229] M. Sing, V. G. Grigoryan, G. Paasch, M. Knupfer, J. Fink, H. Berger and F. Lévy. *Phys. Rev. B* 57 12768 (1998).
- [230] D. Pines. *Can. J. Phys.* 34 1379 (1956).
- [231] E. H. Hwang and S. D. Sarma. *Int. J. Mod. Phys. B* 12 2769 (1998).
- [232] G. Li, W. Z. Hu, D. Qian, D. Hsieh, M. Z. Hasan, E. Morosan, R. J. Cava and N. L. Wang. *Phys. Rev. Lett.* 99 027404 (2007).
- [233] F. Clerc, C. Battaglia, H. Cercellier, C. Monney, H. Berger, L. Despont, M. G. Garnier and P. Aebi. *J. Phys.: Condens. Matter* 19 355002 (17pp) (2007).
- [234] G. A. Sawatzky, I. S. Elfimov, J. van den Brink and J. Zaanen. *Europhys. Lett.* 86 17006 (2009).
- [235] M. Berciu, I. Elfimov and G. A. Sawatzky. *Phys. Rev. B* 79 214507 (2009).
- [236] A. Koitzsch, D. Inosov, J. Fink, M. Knupfer, H. Eschrig, S. V. Borisenko, G. Behr, A. Köhler, J. Werner, B. Büchner, R. Follath and H. A. Dürr. *Phys. Rev. B* 78 180506 (2008).

- [237] T. Kroll, S. Bonhommeau, T. Kachel, H. A. Dürr, J. Werner, G. Behr, A. Koitzsch, R. Hübel, S. Leger, R. Schönfelder, A. K. Ariffin, R. Manzke, F. M. F. de Groot, J. Fink, H. Eschrig, B. Büchner and M. Knupfer. *Phys. Rev. B* 78 220502 (2008).
- [238] D. J. Singh. *Phys. Rev. B* 78 094511 (2008).
- [239] J. M. Ziman. *Principles of the theory of solids* (Cambridge University Press, 1972).
- [240] S.-L. Drechsler, M. Grobosch, K. Koepfner, G. Behr, A. Köhler, J. Werner, A. Kondrat, N. Leps, C. Hess, R. Klingeler, R. Schuster, B. Büchner and M. Knupfer. *Phys. Rev. Lett.* 101 257004 (2008).
- [241] S.-L. Drechsler, H. Rosner, M. Grobosch, G. Behr, F. Roth, G. Fuchs, K. Koepfner, R. Schuster, J. Malek, M. R. S. Elgazzar, D. Johrendt, H.-H. Klauss, B. Büchner and M. Knupfer. New insight into the physics of iron pnictides from optical and penetration depth data (2009). Submitted to New J. Phys.
- [242] B. Sipos. *Normal state transport properties of novel superconductors*. Ph.D. thesis, EPFL Lausanne, Lausanne (2009).
- [243] H. F. Hess, R. B. Robinson, R. C. Dynes, J. J. M. Valles and J. V. Waszczak. *J. Vac. Sci. Technol.* A8 450 (1990).
- [244] C. Wang, C. G. Slough and R. V. Coleman. *J. Vac. Sci. Technol.* B9 1048 (1991).
- [245] A. S. Barker, J. A. Ditzberger and F. J. DiSalvo. *Phys. Rev. B* 12 2049 (1975).
- [246] Y. Wakisaka, T. Sudayama, K. Takubo, T. Mizokawa, M. Arita, H. Namatame, M. Taniguchi, N. Katayama, M. Nohara and H. Takagi. *Phys. Rev. Lett.* 103 026402 (2009).
- [247] J. R. Tessman, A. H. Kahn and W. Shockley. *Phys. Rev.* 92 890 (1953).
- [248] C. Hess, A. Kondrat, A. Narduzzo, J. E. Hamann-Borrero, R. Klingeler, J. Werner, G. Behr and B. Buchner. *Europhys. Lett.* 87 17005 (2009).
- [249] H. Luetkens, H.-H. Klauss, M. Kraken, F. J. Litterst, T. Dellmann, R. Klingeler, C. Hess, R. Khasanov, A. Amato, C. Baines, M. Kosmala, O. J. Schumann, M. Braden, J. Hamann-Borrero, N. Leps, A. Kondrat, G. Behr, J. Werner and B. Buchner. *Nat Mater* 8 305 (2009).

Danksagung

Viele Leute haben einen Beitrag zum Gelingen dieser Arbeit geleistet. Da ich mich hier nicht überschwänglich ausbreiten möchte, mache ich es relativ schmerzlos.

Herzlich gedankt sei an dieser Stelle:

- B. Büchner für die immerwährende Unterstützung und das Strippenziehen hinter den Kulissen
- M. Grüninger für die Übernahme des Zweitgutachtens
- M. Knupfer für die ständige Diskussionsbereitschaft, die hilfreichen physikalischen Bilder und die immer kritischen Anmerkungen
- J. Fink für noch viel kritischere Anmerkungen
- den (ehemaligen) Mitgliedern der IFW ARPES-Gruppe: V. B. Zabolotnyy, D. S. Inosov, D. V. Evtushinsky, A. A. Kordyuk und S. V. Borisenko für den einen oder anderen Programmierhinweis und die zahlreichen Diskussionen
- S.-L. Drechsler für die andauernden Besuche und die sich dabei oftmals einstellenden Aha-Effekte
- R. Hübel – meinem „Raumteiler“ – für das angenehme Arbeitsklima, das „dumme Gequatsche“ und die vielen technischen Hinweise
- den übrigen Mitgliedern der Abteilung „Elektronische und optische Eigenschaften“ für die Hilfe bei der Arbeit im Labor und bei sonstigen alltäglichen Verrichtungen
- dem IFF Sekretariat bei allerlei administrativem Kram und
- ... dem Rest, aber der ist privat.

Versicherung

Hiermit versichere ich, dass ich die vorliegende Arbeit ohne unzulässige Hilfe Dritter und ohne Benutzung anderer als der angegebenen Hilfsmittel angefertigt habe; die aus fremden Quellen direkt oder indirekt übernommenen Gedanken sind als solche kenntlich gemacht. Die Arbeit wurde bisher weder im Inland noch im Ausland in gleicher oder ähnlicher Form einer anderen Prüfungsbehörde vorgelegt.

Die vorliegende Arbeit wurde unter Betreuung von Prof. Dr. rer. nat. habil. B. Büchner am IFW Dresden angefertigt.

Bis zum jetzigen Zeitpunkt habe ich keinerlei erfolglose Promotionsverfahren absolviert.

Die Promotionsordnung der Fakultät Mathematik und Naturwissenschaften der Technischen Universität Dresden erkenne ich an.

Dresden, den

Roman Schuster